



UGR

Universidad
de Granada

Analysis of Composite Shells: Isogeometric Modelling and Damage Identification

Author:
Cesar Fernandez Casanova

Granada, November 2013

Advisor:
Antolino Gallego Molina

"The heart has its reasons which reason knows nothing of."

Blaise Pascal.

Acknowledgements

The author thank Spanish I+D National Plan “DPI2006-02970” Project and Junta de Andalucía “Proyecto de Excelencia P08-TEP-03641” “Detección de defectos en materiales compuestos avanzados de uso aeronáutico mediante técnicas vibro-acústicas y modelos de optimización (DEMAC)” and “Actividades de SHM en placas de material compuesto y cajones multilarguero” de alas integradas DAICA for financial assistance, Ref. CBC-DAICA SOW05 UGR Contract UGR with EADS-CASA.

The author also thanks:

To my family and dear friends. In this arduous journey, they have been a shoulder to lean on.

To Dr. Antolino Gallego as a Director of this PhD for giving me freedom that I so much appreciate and considering me for the P08-TEP-03641 Project.

To Dr. Thomas J. R. Hughes for accepting me as Visitor at the ICES in 2011 and 2013. Also for his incomparable knowledge about the FEM.

To Dr. Robert L. Taylor, who I had the pleasure to met in 2011. He developed FEAP, program that I have used in a big part of this work. My deepest admiration to a person that in his 80's is still coding.

To the SNADS colleges: Dr. Andrés Roldán Aranda, Dr. Pablo Moreno Garcia, Dr. Liliana Romero, Dr. Enrique Castro Rodriguez, Francisco Antonio Sagasta, Elisabet Suárez Vargas and last but not least Cristobal José Infantes Marquez for their at different aspects of the experiments related to this project.

To the ICES colleagues, specially, Dr. Luca Dede', Dr. Dominik Shillinger and Dr. Jahangir Hossain Shaikh for his help with some IGA concepts during the visits at the ICES.

Finally, to Dr. Mario Lázaro Navarro and Dr. Ignacio Ferrer Ballester, friends and colleagues.

Rights of authors

The doctoral Cesar Fernandez Casanova and the director of the thesis Antolino Gallego Molina, guarantee, by signing this thesis, the work has been done by the doctoral under the supervision of the thesis advisor and as far as our knowledge reaches, this work have respected the rights of other authors to be cited, when they have used their results or publications.

El doctorando César Fernández Casanova y el director de la tesis Antolino Gallego Molina, garantizamos, al firmar esta tesis doctoral, que el trabajo ha sido realizado por el doctorando bajo la dirección del director de la tesis y hasta donde nuestro conocimiento alcanza, en la realización del trabajo, se han respetado los derechos de otros autores a ser citados, cuando se han utilizado sus resultados o publicaciones.

Granada, October 30th, 2013

Antolino Gallego Molina: Advisor of Thesis

Cesar Fernandez Casanova: Doctoral

Preface

Composite materials have become more popular in recent decades. From their origins until the present day, their use has grown in sectors such as aerospace, automotive, energy and other civil engineering applications. In fact, they constitute an interdisciplinary area, where the work of many professionals (engineers, chemists, physicists, etc.) converges into a final product that must be inspected for maintenance in view of its applications. This study focuses on two particular areas, one pertaining to the field of structural analysis, the other within the field of Structural Health Monitoring (SHM).

Finite Element Analysis (FEA) contributes very substantially to the development of composite materials, making possible the computation of plate and shell theories. Recently, Isogeometric Analysis (IGA) has emerged as a new finite element theory that solves some of the limitations of the standard FEA. Unifying geometry definition and analysis, this recent theory serves to define and compute complex geometries while improving computation accuracy. It stands as a very promising way to generalize the definition and analysis of structures.

This work develops a composite shell with the novel Isogeometric Analysis (IGA) formulation, allowing for a definition of complex geometries through the use of non uniform rational B-Splines (NURBS).

Chapter 1 (Paper: *NURBS – based analysis of higher – order composite shells*) implements a shell for the most widely used ESL theories for shell structures, and verifies its implementation for some benchmark and numerical static and dynamic problems.

However, as happens with the standard finite element formulations, the same numerical issues accompany IGA. Chapter 2 develops a locking-free shell with this formulation. Both shear-locking and curvature-locking are avoided, and the obtained results present better accuracy.

The second area of focus lies in the field of SHM, and more concretely in delamination detection in Carbon Fiber Reinforced Polymer (CFRP) plates. Therefore, numerical and experimental analyses are performed in order to study the possibilities of delamination detection through the use of piezoelectric (PZT) sensors and actuators.

Chapter 3 (Paper: *On the Accuracy of a 4 – Node Delaminated Composite Plate Element and its Application to Damage Detection*) develops a delaminated finite element for a composite plate. Mode shape changes, frequency shifts and Frequency Response Function (FRF) changes are computed to study the effect of delamination in the dynamic response for several delamination sizes.

Chapter 4 presents an experimental study for three orthotropic composite plates $[0\ 90]_{3s}$, two of them with an internal delamination, provided by Airbus (EADS-CASA, Puerto de Santa María). Analysis of the FRF gives rise to several conclusions, some of them illustrated by means of the element developed in Chapter 3.

In Chapter 5 (Paper: *Modal Analysis of Delaminated Composite Plates using the Finite Element Method and Damage Detection via combined Ritz/2d – Wavelet Analysis*), the developed element from Chapter 2 is used to contribute with some numerical FEM results in order to test a new damage detection technique, from a theoretical point of view. The author limits mention of this contribution

on the delaminated model and results, since no further work has been done. Therefore, appears as co-author.

Finally in Chapter 6, general conclusions and lines of future work are expounded.

Important Remark :

This Doctoral Thesis is structured as a sequence of several papers. Chapters 1, 3 and 5 correspond to already published papers, whereas Chapters 2 and 4 will be submitted soon. Therefore, the reader may encounter some overlap of information in the different chapters. For example, the description of Isogeometric Analysis and composite equations included in Chapters 1 and 2, or the formulation of the delaminated element described in Chapters 3, 4 and 5. The author apologizes for such repetitions owing to the original underlying structure of the work.

Contents

Acknowledgements	v
Rights of authors	vii
Preface	ix
General Index	xiii
List of Figures	xvii
List of Tables	xxi
1 NURBS-based analysis of higher-order composite shells	3
1.1 Introduction	3
1.2 Isogeometric analysis	4
1.2.1 B-Splines	4
1.2.2 B-Spline curves and surfaces	5
1.2.3 NURBS	5
1.2.4 Mesh refinement	6
1.3 Shell formulation	6
1.3.1 Ply description	6
1.3.2 Laminate description	8
1.3.3 FEM implementation	10
1.3.4 IGA aspects	10
1.4 Numerical results	11
1.4.1 Simply supported plate	11
1.4.2 Simply supported cylinder	15
1.4.3 Clamped cylinder	16
1.5 Conclusions	20
2 An Isogeometric higher-order locking-free shell	21
2.1 Introduction	21

2.2 Isogeometric analysis.	22
2.2.1 B-Splines	22
2.2.2 B-Spline curves and surfaces	23
2.2.3 NURBS.	23
2.2.4 Mesh refinement	24
2.3 Shell formulation	24
2.3.1 Ply description	24
2.3.2 Laminate description.	25
2.3.3 FEM implementation	28
2.4 Numerical results	29
2.4.1 Simply supported plate	29
2.4.2 Cantilever plate.	34
2.4.3 Scoderlis Lo-roof	35
2.5 Conclusions	36
3 On the Accuracy of a 4-Node Delaminated Composite Plate Element and its Application to Damage Detection	39
3.1 Introduction	40
3.2 Delamination model	42
3.2.1 Kinematic equations of a delamination.	42
3.2.2 FEM formulation	43
3.3 Element validation	44
3.3.1 Patch Test	44
3.3.2 Convergence and accuracy compared with separate elements. Benchmark problem 1	45
3.3.3 Convergence and accuracy compared with separate elements. Benchmark problem 2.	46
3.4 Numerical examples for damage detection.	47
3.4.1 Cantilever beam.	47
3.4.2 Plates	51
3.5 Conclusions and further work	56
4 Experimental analysis of orthotropic composite plates. Comparison with numerical results	57
4.1 Introduction	57
4.2 Description of the composite SEDA plates and the experiment.	58
4.3 Experiment	61
4.4 Experiment variability.	62
4.5 Experimental results	64
4.6 Comparison with numerical results	66
4.6.1 Comparison with the given parameters.	67
4.6.2 Comparison with the inverse optimized parameters	71
4.7 General conclusions.	75

5 Modal Analysis of Delaminated Composite Plates using the Finite Element Method and Damage Detection via combined Ritz/2d-Wavelet Analysis	77
5.1 Introduction	78
5.2 Delamination model	79
5.2.1 Kinematic delamination equations	79
5.2.2 FEM Formulation	82
5.3 Semianalytical solution for the plate modes.	82
5.4 Damage detection.	83
5.5 Results	84
5.5.1 Cases analysed	84
5.5.2 Mode shapes.	86
5.5.3 FRF Analysis	86
5.5.4 Wavelet Analysis	87
5.5.5 Influence of the delamination thickness position	87
5.5.6 Influence of boundary conditions	88
5.5.7 Effect of added noise.	88
5.6 Conclusions	91
6 Conclusions and further works	93
References	95

List of Figures

1.1	Cubic basis functions for open knot vector $\Xi = \{0, 0, 0, 0, 1/5, 2/5, 3/5, 4/5, 1, 1, 1, 1\}$	5
1.2	B-Spline curve for open knot vector $\Xi = \{0, 0, 0, 0, 1/5, 2/5, 3/5, 4/5, 1, 1, 1, 1\}$	5
1.3	NURBS-based cylindrical surface for $\Xi = \{0, 0, 0, 1, 1, 1\}$ and $\mathcal{H} = \{0, 0, 1, 1\}$. Element and control mesh before and after a k -refinement.	6
1.4	Orientation of axes at ply level.	7
1.5	Shell description for TSDT.	8
1.6	IGA Plate model. Element mesh and control points.	12
1.7	IGA simply supported cylinder model. Element mesh and control points.	15
1.8	Mode 1 of simply supported cylinder.	16
1.9	IGA clamped cylinder model. Meshes for 8x8 and 16x16 elements.	17
1.10	Deformation (in) of clamped cylinder subjected to a uniform transverse load.	18
1.11	IGA clamped complete cylinder model. Element mesh and control points.	18
1.12	Deformation (in) of complete cylinder by internal pressure.	19
1.13	Mode 1 of clamped complete cylinder.	20
2.1	Cubic basis functions for open knot vector $\Xi = \{0, 0, 0, 0, 1/5, 2/5, 3/5, 4/5, 1, 1, 1, 1\}$	23
2.2	B-Spline curve for open knot vector $\Xi = \{0, 0, 0, 0, 1/5, 2/5, 3/5, 4/5, 1, 1, 1, 1\}$	23
2.3	NURBS-based cylindrical surface for $\Xi = \{0, 0, 0, 1, 1, 1\}$ and $\mathcal{H} = \{0, 0, 1, 1\}$. Element and control mesh before and after a k -refinement.	24
2.4	Orientation of axes at ply level.	25
2.5	Natural local bases for reference and deformed configurations.	26
2.6	Hierarchic difference vector.	27
2.7	IGA Plate model. Element mesh and control points.	30
2.8	IGA vs. hierarchic (*) vector displacements error for quadratic, cubic and quartic NURBS for the simply supported plate.	31

2.9	IGA vs. hierarchic vector normalized frequencies for $h=0.2$ m, $h=0.1$ m, $h=0.01$ m and $h=0.001$ m for the simply supported plate.	32
2.10	Skew plate model. Element mesh and control points.	33
2.11	Cantilever plate mesh (8 elements) and deformed configuration.	34
2.12	IGA vs. hierarchic vs. hierarchic (*) vector displacements error for quadratic and cubic NURBS for the cantilever plate for the FSDT and TSDT.	35
2.13	Maximum vertical displacement for the standard IGA, hierarchic vector and hierarchic (*) for cubic and quartic NURBS.	36
2.14	Scoderlis model and deformed configuration.	37
3.1	4 Regions Approach	41
3.2	a) Delaminated cantilever beam. b) FEM model.	45
3.3	a) Relative error in L_2 -Norm for separate elements (DKQ) and delaminated element. b) Relative error in eigenfreq. (1-4). Lines (DKQ), dots (delaminated element).	46
3.4	a) Delaminated circular clamped plate (quarter represented). b) FEM model.	46
3.5	a) Relative error in L_2 -Norm for separate elements (DKQ) and delaminated element. b) Relative error in eigenfreq. (1-3). Lines (DKQ), dots (delaminated element).	47
3.6	Delaminated FEM Model of a cantilever beam. Green elements represent the delamination.	48
3.7	Eigenvector 6 of displacements for extensions I, II and III. a) Composite $[0\ 90]_{3S}$. b) Composite $[0\ 90\ 45\ -45\ 0\ 90]_S$. The undamaged one is represented by 0. The vertical dashed line represents the center of the delamination.	49
3.8	Eigenvector 6 of curvatures for extensions I, II and III. a) Composite $[0\ 90]_{3S}$. b) Composite $[0\ 90\ 45\ -45\ 0\ 90]_S$. The undamaged one is represented by 0. The vertical dashed line represents the center of the delamination.	49
3.9	Frequency shifts (%) for composite $[0\ 90]_{3S}$ for modes 5, 6 and 7. a) Influence of the delamination extension. Delamination center at $x = 0.45 L$. b) Influence of delamination location, with extension 10%.	50
3.10	Eigenvector 6 of displacements for different delamination locations. Extension is 10%.	50
3.11	Composite clamped plate. Sections where eigenvectors are obtained (F1 and F2). Actuator (A1). Sensor (S1). Delamination (D).	51
3.12	Eigenvectors of 2-nd mode at section $x=0.13$ m (F1). Extensions I, II and III. a) Displacements w . b) Curvatures κ_x	52
3.13	Eigenvectors of 2-nd mode at section $y=0.58$ m (F2). Extensions I, II and III. a) Displacements w . b) Curvatures κ_y	53
3.14	FRF at location $x = 0.75$ m and $y = 0.30$ m. a) Extensions 0, I, II, III. b) Extensions 0, IV, V and VI.	55
3.15	Selected bandwidths of FRF (to compute damage indexes). a) Extensions 0, I, II, III. b) Extensions 0, IV, V and VI. Marked eigenfrequency: 1139 Hz.	56

4.1	SEDA $[0\ 90]_{3S}$ composite plates.	59
4.2	PULSE-System and SEDA plate on the steel frame instrumented with one actuator and two sensors.	60
4.3	PZT used as Actuator and Sensor.	61
4.4	Actuator and sensor positions. Clamped dimensions. All data in mm.	61
4.5	SEDA plate over foam.	62
4.6	Variability of instrumentation system for undelaminated plate.	63
4.7	Variability of the FRF for the undelaminated clamped plate.	63
4.8	Variability of the FRF for the undelaminated clamped plate. Frequency band $[350\ 500]$ Hz.	64
4.9	FRF of the undelaminated and 80x80 mm delamination plates.	65
4.10	FRF of undelaminated and 180x180 mm delamination plates.	66
4.11	Finite element model of the delaminated plate. Delamination 80x80 mm.	67
4.12	Numerical and experimental comparison for undelaminated and 80x80 mm delamination plates over the bandwidth $[0\ 500]$ Hz.	68
4.13	Numerical and experimental comparison for undelaminated and 80x80 mm delamination plates over the bandwidth $[500\ 1500]$ Hz.	68
4.14	Numerical and experimental comparison for undelaminated and 80x80 mm delamination plates over the bandwidth $[1500\ 3500]$ Hz.	69
4.15	Numerical and experimental comparison for undelaminated and 180x180 mm delamination plates over the bandwidth $[0\ 500]$ Hz.	69
4.16	Numerical and experimental comparison for undelaminated and 180x180 mm delamination plates over the bandwidth $[500\ 1500]$ Hz.	70
4.17	Numerical and experimental comparison for undelaminated and 180x180 mm delamination plates over the bandwidth $[1500\ 3500]$ Hz.	70
4.18	Numerical fitted frequencies at the frequency band $[0\ 500]$ Hz. First 17 eigenfrequencies.	71
4.19	Experimental and numerical FRF over the bandwidth $[0\ 500]$ Hz.	71
4.20	Numerical and experimental comparison for undelaminated and 80x80 mm delamination plates over the bandwidth $[0\ 500]$ Hz.	72
4.21	Numerical and experimental comparison for undelaminated and 80x80 mm delamination plates over the bandwidth $[500\ 1000]$ Hz.	73
4.22	Numerical and experimental comparison for undelaminated and 80x80 mm delamination plates over the bandwidth $[1000\ 1500]$ Hz.	73
4.23	Numerical and experimental comparison for undelaminated and 180x180 mm delamination plates over the bandwidth $[0\ 500]$ Hz.	74
4.24	Numerical and experimental comparison for undelaminated and 180x180 mm delamination plates over the bandwidth $[500\ 1000]$ Hz.	74

4.25	Numerical and experimental comparison for undelaminated and 180x180 mm delamination plates over the bandwidth [1000 1500] Hz.	75
5.1	Kinematics of delamination [56]	80
5.2	Block diagram for damage detection based on Ritz method and Wavelet Transform.	83
5.3	Halo Wavelet in Spatial domain (a) and Frequency domain (b).	84
5.4	FEM Model. Case IV of damage	85
5.5	Mode shapes 1(a), 2 (b), 4 (c) and 6 (d) for x-Curvatures for a plate with case I delamination	86
5.6	Mode shapes 1 (a), 2 (b), 4 (c) and 6 (d) for x-Curvatures for a plate with case IV delamination	87
5.7	FRF at locations S1 (a, b) and S2 (c, d) and cases 0, I, II, III (a, c) and 0, IV, V, VI (b, d)	88
5.8	Damage index $D(x, y)$ for damage cases I (a), II (b), IV (c) and VI (d) using mode 1. Horizontal line: coordinate x ; vertical line: coordinate y	89
5.9	Damage index $D(x, y)$ for damage cases I (a), II (b), IV (c) and VI (d) using mode 3. Horizontal line: coordinate x ; vertical line: coordinate y	89
5.10	Damage index $D(x, y)$ for damage cases VII (a, d), VIII (b, e) and IV (c, f) using mode 1 (a, b, c) and mode 3 (d, e, f). Horizontal line: coordinate x ; vertical line: coordinate y	90
5.11	Damage index $D(x, y)$ for damage case IV when the plate is fully simply supported (a, c) and fully clamped (b, d) using mode 1 (a, b) and mode 3 (c, d). Horizontal line: coordinate x ; vertical line: coordinate y	90
5.12	Damage index $D(x, y)$ for damage cases I (a), II (b), IV (c) and VI (d) using noisy mode 1. Horizontal line: coordinate x ; vertical line: coordinate y	91
5.13	Damage index $D(x, y)$ for damage cases I (a), II (b), IV (c) and VI (d) using noisy mode 3. Horizontal line: coordinate x ; vertical line: coordinate y	91

List of Tables

1.1	IGA and analytical results for a $[0\ 90\ 90\ 0]$ square plate for CLT, FSDT and TSDT subjected to a sinusoidal load	13
1.2	Normalized displacements for $[0\ 90]_n$ for CLT, FSDT and TSDT subjected to a sinusoidal load	13
1.3	Normalized displacements for $[45\ -45]_n$ for CLT, FSDT and TSDT subjected to a sinusoidal load	14
1.4	Normalized frequency of $[0\ 90\ 0]$ for CLT, FSDT and TSDT.	14
1.5	Normalized first frequency for $[45\ -45]_n$ for FSDT and TSDT.	15
1.6	Normalized first frequency for $[90\ 0]$, $[0\ 90\ 0]$ and $[0\ 90\ 90\ 0]$ simply supported cylinder for FSDT and TSDT.	16
1.7	Maximum displacement (in) at isotropic clamped cylinder subjected to a uniform transverse load.	17
1.8	Maximum displacement (in) for $[0]$ clamped cylinder with internal pressure for CLT, FSDT and TSDT.	18
1.9	Normalized first frequency for $[0\ 90]$ and $[90\ 0]$ clamped complete cylinder for FSDT and TSDT.	19
2.1	Scheme for the projection.	29
2.2	Standard IGA vs. hierarchic approximation for quartic NURBS and analytical results for an isotropic square plate for CLT, FSDT and TSDT subjected to a uniform load. .	30
2.3	Standard IGA vs. hierarchic approximation for cubic NURBS and analytical results for an isotropic square plate for CLT, FSDT and TSDT subjected to a uniform load. .	30
2.4	Standard IGA vs. hierarchic approximation for quadratic NURBS and analytical results for an isotropic square plate for CLT, FSDT and TSDT subjected to a uniform load. .	31
2.5	Normalized frequency for isotropic plate of thickness $h=0.1m$ for CLT, FSDT and TSDT.	33
2.6	Normalized displacements for a clamped isotropic skew plate with a TSDT under a uniform load.	33
2.7	Standard IGA vs. hierarchic vs. hierarchic (*) approximation for quartic NURBS and analytical results for a cantilever plate for FSDT and TSDT subjected to a vertical load.	34

2.8	Standard IGA vs. hierarchic vs. hierarchic (*) approximation for cubic NURBS and analytical results for a cantilever plate for FSDT and TSDT subjected to a vertical load.	35
2.9	Standard IGA vs. hierarchich (*) approximation for cubic and quartic NURBS and analytical results for a cantilever plate for CLT subjected to a vertical load.	35
2.10	Scoderlis problem. Maximum vertical displacement w_z for standard IGA vs. hierarchic vs. hierarchic (*) approximation for cubic and quartic NURBS.	36
3.1	Different delamination extensions and position in the thickness for the composite beam	48
3.2	Frequency shifts of a cantilever beam of $[0\ 90]_{3S}$ and $[0\ 90\ 45\ -45\ 0\ 90]_S$ composites	48
3.3	Damage indexes DI (%) for displacements w and curvatures κ of a cantilever beam of $[0\ 90]_{3S}$ and $[0\ 90\ 45\ -45\ 0\ 90]_S$ composites	49
3.4	Delamination sizes and position in the thickness for the $[0\ 90]_{3S}$ composite plate . . .	51
3.5	Damage indexes DI (%) for displacements w and curvatures κ_x for section $x=0.13$ m (F1) of the composite plate	52
3.6	Damage indexes DI (%) for displacements w and curvatures κ_y for section $y=0.58$ m (F2) of the composite plate	53
3.7	Damage indexes DI_F and DI_A (%) for selected Eigenfrequencies: 200.2, 207.6, 212.2, 228.6 and 256.0 (Hz) for extensions I, II and III; 1051, 1072, 1086, 1119 and 1199 (Hz) for extensions IV, V and VI	55
4.1	PZT used as Actuator and Sensor.	60
4.2	Experimental and numerical natural frequencies with the optimized parameters. . . .	72
4.3	Most significant frequency shifts due to delamination for experimental and numerical (optimized) analysis.	75
5.1	Cases of damage analized	85

Chapter 1

NURBS-based analysis of higher-order composite shells

In this chapter the following paper is presented: “NURBS-based analysis of higher-order composite shells” published in the Journal: Composite Structures in 2013, with doi:10.1016/j.compstruct.2013.04.024. The chapter presents a third order composite shell, developed with an Isogeometric analysis formulation. The continuity advantages of NURBS make this approach very promising, from both geometric and FEM perspectives. Some static and dynamic results are provided and compared with some known solutions in order to proof the efficiency of this formulation.

Abstract

Isogeometric analysis (IGA) can represent general double-curved geometries very well, as opposed to the classic finite element method (FEM). A composite shell is introduced for a third-order shear deformation theory (TSDT) that achieves the C^2 required continuity by the use of higher-order NURBS through a k -refinement strategy. The TSDT is therefore an approach that can be easily implemented in view of the IGA advantages. Numerical locking is moreover avoided by the use of higher-order NURBS. Here, linear static and dynamic analyses are performed and compared with some known analytical and FEM solutions to demonstrate the efficiency of Isogeometric analysis for TSDT and for the most widely used equivalent single layer theories (ESL), that is, classical laminate theory (CLT) and first order shear deformation theory (FSDT).

Keywords : Isogeometric; IGA; Composite; Shell; Higher-Order Theory; HOT

1.1 Introduction

The use of advanced composite materials has grown in recent decades. From the structural point of view, their stiffness, weight, fatigue-life and strength-to-weight relation make these materials very attractive [1]. Composites are used today by the aircraft industry as well as marine and aerospace sectors, and they have numerous engineering applications.

Composites have general geometric forms in many of their applications, requiring complex analysis to achieve good results. The development of the finite element method (FEM) has certainly contributed to the development of these materials. Shell theories, developed mostly with the so-called equivalent single layer theories (ESL), offer a good balance between the accuracy of the results from the numerical point of view and the time involved. The most popular ones entail Love-Kirchhoff elements, with the

classical laminate theory (CLT) and Reissner-Mindlin elements, with a first order shear deformation theory (FSDT). They have been widely used, providing acceptable results. For an enhanced approach to stresses, refined ESL theories were developed, constituting the so-called higher-order deformation theories (HOT). Meanwhile, bridge theories between the ESL and 3D-elasticity were developed, becoming known as Layerwise theories, yet these often required much more computational time. A good review of the different theories can be found in [2] for the ESL and in [3] for both ESL and Layerwise ones.

Due to their simplicity, commercial codes mostly implement shells that approximate the mesh geometry with planar elements. This implies very refined meshes to achieve a good approximation if the curvature is relative low, conditioning the FEM mesh to ensure accuracy. Many of the shell elements that have been developed to date are not implemented due to limitations surrounding the geometric continuity between elements.

On the other hand computer-aided design (CAD), computer graphics (CG) and animations eventually provided very good approximations of general complex geometries through the use of splines. Isogeometric analysis (IGA) achieves the union between FEA with CAD, CG and animation. Developed by Tom Hughes and co-workers, this method combines geometry and analysis using tools common to both. That is, the geometric basis functions are also used as the approximation functions required for analysis. Interested readers can find more details in [4, 5].

1.2 Isogeometric analysis

Non uniform rational B-Splines (NURBS) are a standard tool for representing curves and surfaces in computer-aided design and computer graphics. In this section, a short description of the isogeometric analysis concepts is briefly presented. More details are found in the fundamental works of Hughes and co-workers [4, 5, 6, 7, 8] for isogeometric analysis; and in Piegl and Tiller [9], Rogers [10], Farin [11] and Cohen [12] for a comprehensive review of the underlying geometric concepts and algorithms.

1.2.1 B-Splines

A B-spline is a non-interpolating, piecewise polynomial curve. It is defined by a knot vector Ξ , a set of control points, \mathbf{B}_i ($i=1,2,\dots,n$) and a polynomial degree. The knot vector is a set of non-decreasing real numbers representing points in the parametric space of the curve:

$$\Xi = \{\xi_1, \xi_2, \dots, \xi_{n+p+1}\}, \quad (1.1)$$

where p is the degree of the curve and n is the number of basis functions, corresponding to the \mathbf{B}_i control points.

B-Spline basis functions are defined recursively starting from $p=0$ (piecewise constant) using the Cox-de Boor formula:

$$N_{i,0}(\xi) = \begin{cases} 1 & \text{if } \xi \leq \xi < \xi_{i+1} \\ 0 & \text{otherwise} \end{cases} \quad (1.2)$$

and for $p \geq 1$:

$$N_{i,p}(\xi) = \frac{\xi - \xi_i}{\xi_{i+p} - \xi_i} N_{i,p-1}(\xi) + \frac{\xi_{i+p+1} - \xi}{\xi_{i+p+1} - \xi_{i+1}} N_{i+1,p-1}(\xi) \quad (1.3)$$

Figure 1.1 shows an example of cubic basis functions with an open knot vector.

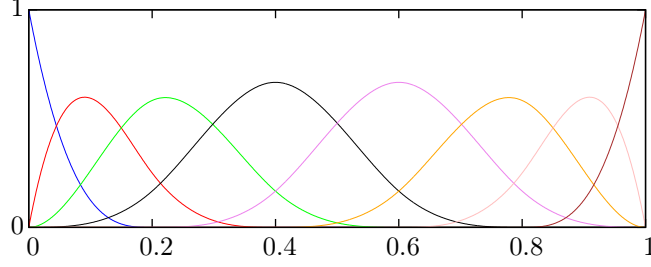


Figure 1.1: Cubic basis functions for open knot vector $\Xi = \{0, 0, 0, 0, 1/5, 2/5, 3/5, 4/5, 1, 1, 1, 1\}$.

1.2.2 B-Spline curves and surfaces

A B-Spline curve is constructed through a linear combination of B-Spline basis functions and the control points. Figure 2.2 shows an example of a B-Spline curve with its control points.

$$\mathbf{C}(\xi) = \sum_{i=1}^n N_{i,p}(\xi) \mathbf{B}_i \quad (1.4)$$

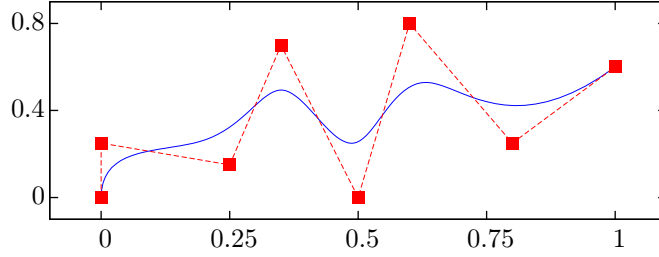


Figure 1.2: B-Spline curve for open knot vector $\Xi = \{0, 0, 0, 0, 1/5, 2/5, 3/5, 4/5, 1, 1, 1, 1\}$.

B-Spline surface basis are computed by means of the tensor product of single univariate B-Spline basis functions. Thus, two individual knot vectors $\Xi = \{\xi_1, \xi_2, \dots, \xi_{n+p+1}\}$ and $\mathcal{H} = \{\eta_1, \eta_2, \dots, \eta_{m+q+1}\}$, and a set of $n \cdot m$ control points $\mathbf{B}_{i,j}$ ($i=1,2,\dots,n$; $j=1,2,\dots,m$), define the B-Spline surface:

$$\mathbf{S}(\xi, \eta) = \sum_{i=1}^n \sum_{j=1}^m N_{i,p}(\xi) M_{j,q}(\eta) \mathbf{B}_{i,j} \quad (1.5)$$

1.2.3 NURBS

Non uniform rational B-Splines (NURBS) constitute an improvement upon B-splines, since they can represent more general geometries. Constructed as a projection in \mathbb{R}^d of a B-Spline of \mathbb{R}^{d+1} , NURBS basis can be defined. Then a space point of the B-Spline curve $\mathbf{B}_i^w(x_i, y_i, z_i, w_i)$ is geometrically projected into $\mathbf{B}_i(w_i x_i, w_i y_i, w_i z_i)$. Similarly to B-Spline curves and surfaces, NURBS-based ones are defined as:

$$\mathbf{C}(\xi) = \frac{\sum_{i=1}^n N_{i,p}(\xi) w_i \mathbf{B}_i}{\sum_{i=1}^n N_{i,p}(\xi) w_i} \quad (1.6)$$

$$\mathbf{S}(\xi, \eta) = \frac{\sum_{i=1}^n \sum_{j=1}^m N_{i,p}(\xi) M_{j,q}(\eta) w_{i,j} \mathbf{B}_{i,j}}{\sum_{i=1}^n \sum_{j=1}^m N_{i,p}(\xi) M_{j,q}(\eta) w_{i,j}} \quad (1.7)$$

1.2.4 Mesh refinement

NURBS-based refinements can be done by knot insertion (h refinement) or order increase (p refinement) [5]. Particularly the k -refinement combines order increase in the first place and knot insertion of multiplicity one in the second place. This refinement guarantees C^{p-1} continuity through the entire domain. Figure 2.3 shows an example of a cylindrical surface built with NURBS and the element, and control mesh before and after a k -refinement.

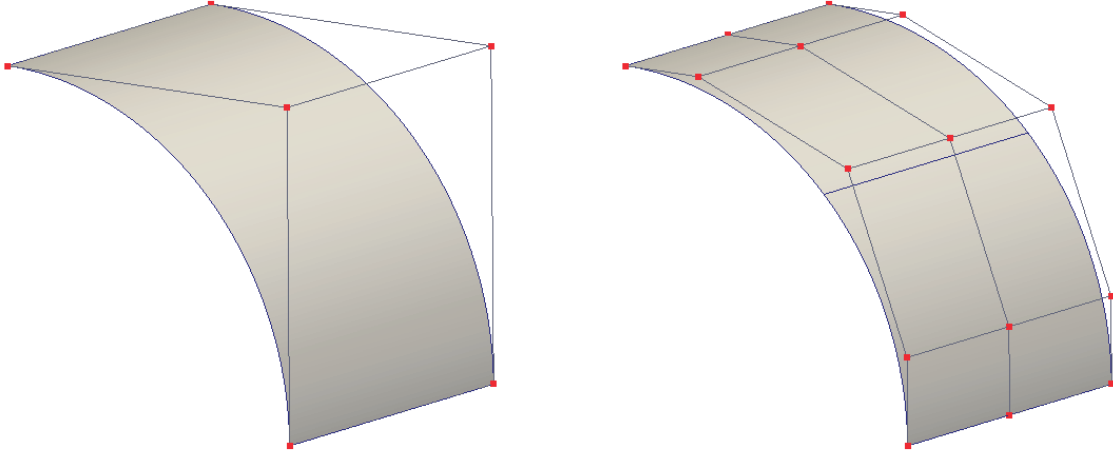


Figure 1.3: NURBS-based cylindrical surface for $\Xi = \{0, 0, 0, 1, 1, 1\}$ and $\mathcal{H} = \{0, 0, 1, 1\}$. Element and control mesh before and after a k -refinement.

1.3 Shell formulation

In this section the laminate shell theory is briefly exposed. First, a description at the ply level is introduced; then, the shell kinematics are described for the adopted ESL theories in order to build the equations of the laminate.

1.3.1 Ply description

ESL layer theories assume that each composite ply behaves as a case of a plane-stress problem, neglecting the transverse normal strain ($\mathbf{E}_{33}=0$). The stress-strain relation for an orthotropic ply can

be expressed with respect the ply/shell selected orthonormal axes as:

$$\begin{aligned}
 \bar{Q}_{11} &= Q_{11}\cos^4\theta + 2(Q_{12} + 2Q_{66})\sin^2\theta\cos^2\theta + Q_{22}\sin^4\theta \\
 \bar{Q}_{12} &= (Q_{11} + Q_{22} - 4Q_{66})\sin^2\theta\cos^2\theta + Q_{12}(\sin^4\theta + \cos^4\theta) \\
 \bar{Q}_{22} &= Q_{11}\sin^4\theta + (2Q_{12} + 2Q_{26})\sin^2\theta\cos^2\theta + Q_{22}\cos^4\theta \\
 \bar{Q}_{16} &= (Q_{11} - Q_{12} - 2Q_{66})\sin\theta\cos^3\theta + (Q_{12} - Q_{22} + 2Q_{66})\sin^3\theta\cos\theta \\
 \bar{Q}_{26} &= (Q_{11} - Q_{12} - 2Q_{66})\sin^3\theta\cos\theta + (Q_{12} - Q_{22} + 2Q_{66})\sin\theta\cos^3\theta \\
 \bar{Q}_{66} &= (Q_{11} + Q_{22} - 2Q_{12} - 2Q_{66})\sin^2\theta + \cos^2\theta + Q_{66}(\sin^4\theta + \cos^4\theta) \\
 \bar{Q}_{44} &= Q_{44}\cos^2\theta + Q_{55}\sin^2\theta \\
 \bar{Q}_{45} &= (Q_{55} - Q_{44})\cos\theta\sin\theta \\
 \bar{Q}_{55} &= Q_{55}\cos^2\theta + Q_{44}\sin^2\theta
 \end{aligned} \tag{1.8}$$

where θ is the angle between the fiber and the first ply/shell axis, plotted in Fig. 2.4.

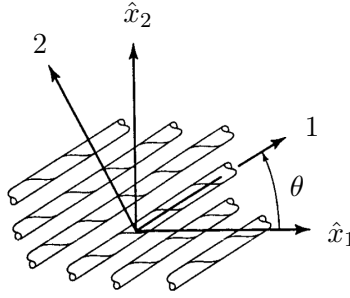


Figure 1.4: Orientation of axes at ply level.

The matrix $\bar{\mathbf{Q}}_r$, where r denotes the corresponding ply, is also called the reduced stiffness ply matrix, which can be rewritten in terms of normal and transverse ply stiffness as:

$$\bar{\mathbf{Q}}_r = \begin{bmatrix} \bar{\mathbf{Q}}_{r1} & \mathbf{0} \\ \mathbf{0} & \bar{\mathbf{Q}}_{r2} \end{bmatrix}; \tag{1.9}$$

where:

$$\bar{\mathbf{Q}}_{r1} = \begin{bmatrix} \bar{Q}_{11} & \bar{Q}_{12} & \bar{Q}_{16} \\ \bar{Q}_{12} & \bar{Q}_{22} & \bar{Q}_{26} \\ \bar{Q}_{16} & \bar{Q}_{26} & \bar{Q}_{66} \end{bmatrix}; \quad \bar{\mathbf{Q}}_{r2} = \begin{bmatrix} \bar{Q}_{44} & \bar{Q}_{45} \\ \bar{Q}_{45} & \bar{Q}_{55} \end{bmatrix} \tag{1.10}$$

1.3.2 Laminate description

The laminate equations will be deduced by considering the corresponding ESL theory. Although CLT, FSDT and TSDT are implemented in the present shell, only a description of the TSDT is exposed, since it is more general and can lead to the other ones, assuming certain well known simplifications.

The undeformed shell geometry can be described by:

$$\mathbf{X}(\xi, \eta, \zeta) = \bar{\mathbf{X}}(\xi, \eta) + \zeta \mathbf{A}_3 \quad (1.11)$$

and the deformed one can be described by:

$$\mathbf{x}(\xi, \eta, \zeta) = \mathbf{X}(\xi, \eta, \zeta) + \mathbf{u}(\xi, \eta, \zeta) \quad (1.12)$$

where \mathbf{A}_3 is the unitary normal vector normal to the undeformed mid-surface and $\mathbf{u}(\xi, \eta, \zeta)$ are the spatial displacements. Figure 2.5 shows the initial and the deformed configuration of the shell (denoted with '); ξ and η are coordinates; ζ is the normal coordinate to the midsurface; \mathbf{e}_1 and \mathbf{e}_2 comprise the selected orthonormal local base. The TSDT transverse section deformed is also plotted, where φ is the CLT rotation and ϕ is the total rotation, which includes the shear deformation proper of the FSDT. Points T and B denote the top and bottom ones of the laminate.

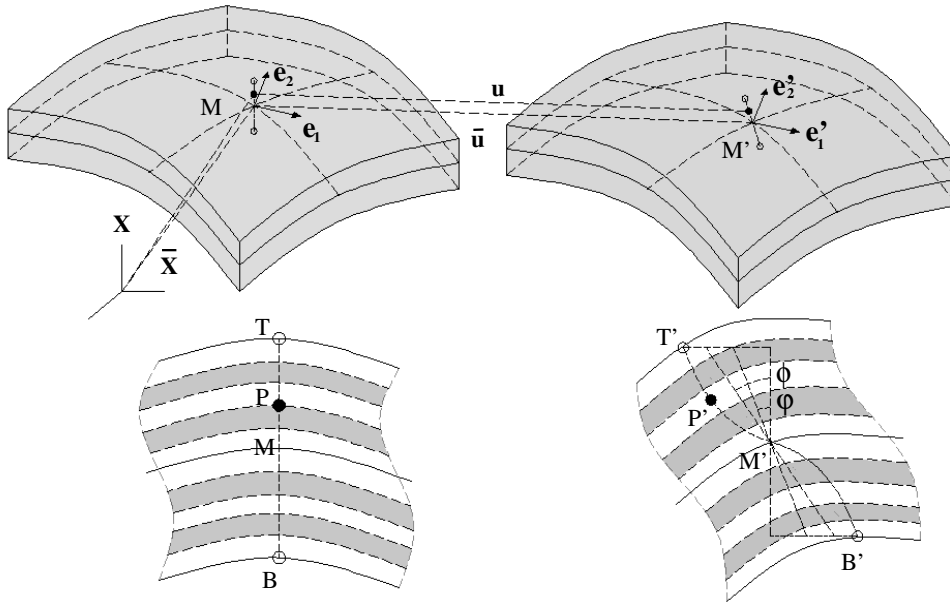


Figure 1.5: Shell description for TSDT.

Third order theories assume a cubic deformation for the transverse displacements, so the kinematics of the deformation for a linear regime can be described by:

$$\mathbf{u}(\xi, \eta, \zeta) = \bar{\mathbf{u}}(\xi, \eta) + \zeta(\phi_2 \mathbf{e}_1 - \phi_1 \mathbf{e}_2) + \zeta^3(\psi_2 \mathbf{e}_1 - \psi_1 \mathbf{e}_2) \quad (1.13)$$

where ϕ_1 and ϕ_2 are the rotations with respect the considered local base and ψ_1 and ψ_2 are new degrees of freedom.

The last term of Equation (2.24) represents the cubic displacements, inherit to the TSDT. ψ_1 and ψ_2 are in principle unknowns, but can be expressed in terms of the other d.o.f. by the assumption of certain conditions. Introduced by Reddy, firstly for plates in [13, 14] and later for shells in [15, 16], it can be assumed that the section is free of tangential stress at the top and the bottom of the laminate ($\tau_{13}(\pm h/2) = \tau_{23}(\pm h/2) = 0$). These conditions allow us to express ψ_1 and ψ_2 in terms of the rest of the d.o.f., the TSDT thus having the same number of d.o.f. as the FSDT, and expressed as:

$$\psi_1 = -\frac{4}{3h^2}(\phi_1 + w_{0,\hat{x}_1}); \quad \psi_2 = -\frac{4}{3h^2}(\phi_2 + w_{0,\hat{x}_2}) \quad (1.14)$$

where \hat{x}_i are local orthonormal coordinates and h is the laminate total thickness.

The strain tensor is obtained by means of the well known formula:

$$\mathbf{E} = \frac{1}{2}(\mathbf{G}_{ij} - \mathbf{g}_{ij}) \quad (1.15)$$

By integration through the thickness, the laminate strain-stress relationships can be obtained and then expressed in the local system as:

$$\begin{bmatrix} \mathbf{N}_0 \\ \mathbf{M}_0 \\ \mathbf{P}_0 \end{bmatrix} = \begin{bmatrix} \mathbf{A} & \mathbf{B} & \mathbf{E} \\ \mathbf{B} & \mathbf{D} & \mathbf{F} \\ \mathbf{E} & \mathbf{F} & \mathbf{H} \end{bmatrix} \begin{bmatrix} \epsilon_0^0 \\ \epsilon_0^1 \\ \epsilon_0^3 \end{bmatrix}; \quad \begin{bmatrix} \mathbf{Q}_0 \\ \mathbf{R}_0 \end{bmatrix} = \begin{bmatrix} \mathbf{A}_s & \mathbf{D}_s \\ \mathbf{D}_s & \mathbf{F}_s \end{bmatrix} \begin{bmatrix} \gamma_0^0 \\ \gamma_0^1 \end{bmatrix} \quad (1.16)$$

where \mathbf{N}_0 , \mathbf{M}_0 , \mathbf{P}_0 , \mathbf{Q}_0 and \mathbf{R}_0 are the resultant forces and moments, and ϵ_0^i and γ_0^i are the in-plane strains;

$$(\mathbf{A}, \mathbf{B}, \mathbf{D}, \mathbf{E}, \mathbf{F}, \mathbf{H}) = \sum_{r=1}^n \int_{-z_r}^{z_r} \bar{\mathbf{Q}}_{r1}(1, z, z^2, z^3, z^4, z^6) dz \quad (1.17)$$

$$(\mathbf{A}_s, \mathbf{D}_s, \mathbf{F}_s) = \sum_{r=1}^n \int_{-z_r}^{z_r} \bar{\mathbf{Q}}_{r2}(1, z^2, z^4) dz \quad (1.18)$$

Equations (2.26)-(2.27) represent the constitutive matrices of the laminate for the TSDT.

1.3.3 FEM implementation

In order to obtain the stiffness and mass matrices, the principle of virtual work is applied:

$$\delta W = \delta W_{int} + \delta W_{ext} = 0 \quad (1.19)$$

with:

$$\begin{aligned} \delta W_{int} &= \int_{\Omega} [\mathbf{S} : \delta \boldsymbol{\epsilon} + \rho \, dm \, \ddot{\mathbf{u}}] \, d\Omega \\ \delta W_{ext} &= \int_{\Omega} \mathbf{f} \cdot \mathbf{u} \, d\Omega \end{aligned} \quad (1.20)$$

From the internal work, and by interpolation of the displacements, the expressions of both matrices are obtained. Hence the stiffness matrix is:

$$\begin{aligned} \mathbf{K} = \int_{\Omega} & [\mathbf{B}_M^T \mathbf{A} \mathbf{B}_M + \mathbf{B}_M^T \mathbf{B} \mathbf{B}_B + \mathbf{B}_B^T \mathbf{B} \mathbf{B}_M + \mathbf{B}_B^T \mathbf{D} \mathbf{B}_B + \mathbf{B}_M^T \mathbf{E} \mathbf{B}_{B^*} + \mathbf{B}_{B^*}^T \mathbf{E} \mathbf{B}_M + \mathbf{B}_B^T \mathbf{F} \mathbf{B}_{B^*} + \\ & \mathbf{B}_{B^*}^T \mathbf{F} \mathbf{B}_B + \mathbf{B}_{B^*}^T \mathbf{H} \mathbf{B}_{B^*} + \mathbf{B}_S^T \mathbf{A}_s \mathbf{B}_S + \mathbf{B}_S^T \mathbf{B}_s \mathbf{B}_S + \mathbf{B}_S^T \mathbf{B}_s \mathbf{B}_{S^*} + \mathbf{B}_{S^*}^T \mathbf{D}_s \mathbf{B}_{S^*}] \, d\Omega \end{aligned} \quad (1.21)$$

where the subscript M refers to the membrane behaviour; B to the linear term of the transverse section deformation; B* to the cubic term; S the shear deformation derived from the linear term and S* the shear deformation derived from the cubic term.

The mass matrix, including its translational, rotational and the additional components derived from the third order theory, is as follows:

$$\begin{aligned} \mathbf{M} = \int_{\Omega} & \rho [\mathbf{N}_u^T \mathbf{N}_u + \mathbf{N}_v^T \mathbf{N}_v + \mathbf{N}_w^T \mathbf{N}_w + z^2 (\mathbf{N}_{\phi 1}^T \mathbf{N}_{\phi 1} + \mathbf{N}_{\phi 2}^T \mathbf{N}_{\phi 2}) + z^4 (\mathbf{N}_{\psi 1}^T \mathbf{N}_{\psi 1} + \mathbf{N}_{\psi 2}^T \mathbf{N}_{\psi 2}) + \\ & z^4 (\mathbf{N}_{\phi 2}^T \mathbf{N}_{\psi 2} + \mathbf{N}_{\psi 2}^T \mathbf{N}_{\phi 2}) + z^6 (\mathbf{N}_{\psi 1}^T \mathbf{N}_{\psi 1} + \mathbf{N}_{\psi 2}^T \mathbf{N}_{\psi 2})] \, d\Omega \end{aligned} \quad (1.22)$$

1.3.4 IGA aspects

As explained before, a shell for CLT, FSDT and TSDT is implemented. Regarding the continuity advantages of NURBS, CLT is implemented with a rotation-free formulation, since it requires C¹ continuity (see [17, 18]). For the TSDT, the C² required continuity is also guaranteed using at least cubic basis through a *k*-refinement strategy. TSDT has the same number of d.o.f. as the FSDT and because of this, the authors wish to underline the TSDT as a better approach, since it does not require any shear correction factor and because shear strains at the ply level can be computed directly. It can be easily implemented with IGA as opposed to the classical FEM, not commonly used due to its implementation disadvantages. Higher-order NURBS are used here, since are numerically quite efficient, in addition to the mentioned continuity requirements and the fact that are almost insensitive to the numerical locking phenomena.

1.4 Numerical results

In this section some benchmark static and dynamic problems are compared with the IGA shell for the introduced TSDT and the widely used ESL theories CLT and FSDT. For all the FSDT problems, a shear correction factor $K=5/6$ was used; TSDT do not require any shear correction factor.

1.4.1 Simply supported plate

A simply supported composite rectangular plate of dimension $a \times b$ was studied. The plate was assumed to be square ($a=b=1$). The IGA model can be seen in Fig. 2.6. A 8×8 mesh with fourth order NURBS basis was used. Two different materials are defined with the following ply properties:

Material 1

$$E_1=25E_2, G_{12}=G_{13}=0.5E_2, G_{23}=0.2E_2, \nu_{12}=\nu_{13}=0.25.$$

Material 2

$$E_1=40E_2, G_{12}=G_{13}=0.6E_2, G_{23}=0.5E_2, \nu_{12}=\nu_{13}=0.25.$$

Two different sets of boundary conditions are also defined:

SS – 1:

$$\begin{aligned} u_0(x, 0) = u_0(x, b) = \theta_x(x, 0) = \theta_x(x, b) = 0 \\ v_0(0, y) = v_0(a, y) = \theta_y(0, y) = \theta_y(a, y) = 0 \\ w_0(x, 0) = w_0(x, b) = w_0(0, y) = w_0(a, y) = 0 \end{aligned} \quad (1.23)$$

$$\begin{aligned} N_{xx}(0, y) = N_{xx}(a, y) = N_{yy}(x, 0) = N_{yy}(x, b) = 0 \\ \bar{M}_{xx}(0, y) = \bar{M}_{xx}(a, y) = \bar{M}_{yy}(x, 0) = \bar{M}_{yy}(x, b) = 0 \end{aligned} \quad (1.24)$$

SS – 2:

$$\begin{aligned} u_0(0, y) = u_0(a, y) = \theta_x(x, 0) = \theta_x(x, b) = 0 \\ v_0(x, 0) = v_0(x, b) = \theta_y(0, y) = \theta_y(a, y) = 0 \\ w_0(x, 0) = w_0(x, b) = w_0(0, y) = w_0(a, y) = 0 \end{aligned} \quad (1.25)$$

$$\begin{aligned} N_{xy}(0, y) = N_{xy}(a, y) = N_{xy}(x, 0) = N_{xy}(x, b) = 0 \\ \bar{M}_{xx}(0, y) = \bar{M}_{xx}(a, y) = \bar{M}_{yy}(x, 0) = \bar{M}_{yy}(x, b) = 0 \end{aligned} \quad (1.26)$$

where $\bar{M} = M_0 - c1 \cdot P_0$, being $c1 = 4/3h^2$.

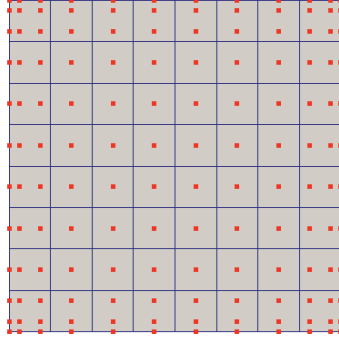


Figure 1.6: IGA Plate model. Element mesh and control points.

For all the static analyses the following normalization was applied:

$$\begin{aligned}
 \bar{\omega} &= \omega_0 \left(\frac{a}{2}, \frac{b}{2}\right) \left(\frac{E_2 h^3}{a^4 q_0}\right); \quad \bar{\sigma}_{xx} = \sigma_{xx} \left(\frac{a}{2}, \frac{b}{2}, \frac{h}{2}\right) \left(\frac{h^2}{b^2 q_0}\right) \\
 \bar{\sigma}_{yy} &= \sigma_{yy} \left(\frac{a}{2}, \frac{b}{2}, \frac{h}{4}\right) \left(\frac{h^2}{b^2 q_0}\right); \quad \bar{\sigma}_{xy} = \sigma_{xy} \left(0, 0, \frac{h}{2}\right) \left(\frac{h^2}{b^2 q_0}\right) \\
 \bar{\tau}_{xz} &= \tau_{xz} \left(\frac{a}{2}, 0, 0\right) \left(\frac{h}{b q_0}\right); \quad \bar{\tau}_{yz} = \tau_{yz} \left(0, \frac{b}{2}, 0\right) \left(\frac{h}{b q_0}\right)
 \end{aligned} \tag{1.27}$$

where a and b are the plate dimensions; h is the laminate thickness and q_0 is the maximum value of the applied load. For the case of a sinusoidal load the spatial distribution is the following:

$$q(x, y) = q_0 \sin\left(\frac{\pi x}{a}\right) \sin\left(\frac{\pi y}{b}\right) \tag{1.28}$$

Static analysis of symmetric cross-ply laminate [0 90 90 0]

The defined simply supported plate with *Material 1* and boundary conditions $SS - 1$ for a cross-ply laminate of stacking sequence $[0\ 90\ 90\ 0]$ subjected to a sinusoidal load (1.28) was analyzed. Table 1.1 shows the results obtained with IGA and the analytical results (normalized displacements and stresses are presented) for CLT, FSDT and TSDT, for different thickness values. The 3D elasticity solution obtained in [19] is also indicated (ELS). IGA results prove exactly the same as the analytical solutions. From relatively thick plates to thin ones ($a/h=100$) all the solutions are exact, that is, fourth order NURBS are accurate for thin plates even with a moderate mesh.

a/h		w	σ_{xx}	σ_{yy}	σ_{xy}	τ_{xz}	τ_{yz}
4	IGA TSDT	1.8937	0.665	0.6322	0.044	0.2064	0.2389
	IGA FSDT	1.7095	0.4059	0.5764	0.0308	0.1398	0.1962
	ELS [19]	1.954	0.72	0.666	0.0467	0.219	0.292
	TSDT [20]	1.8937	0.6651	0.6322	0.044	0.2064	0.2389
10	FSDT [21]	1.71	0.4059	0.5765	0.0308	0.1398	0.1962
	IGA TSDT	0.7147	0.5456	0.3888	0.0268	0.264	0.1531
	IGA FSDT	0.6627	0.4989	0.3614	0.0241	0.1659	0.1292
	ELS [19]	0.743	0.559	0.401	0.0275	0.301	0.196
20	TSDT [20]	0.7147	0.5456	0.3888	0.0268	0.264	0.1531
	FSDT [21]	0.6628	0.4989	0.3615	0.0241	0.1667	0.13
	IGA TSDT	0.506	0.5393	0.3043	0.0228	0.2825	0.1234
	IGA FSDT	0.4912	0.5273	0.2957	0.0221	0.1748	0.1087
100	ELS [19]	0.517	0.543	0.308	0.023	0.328	0.156
	TSDT [20]	0.506	0.5393	0.3043	0.0228	0.2825	0.123
	FSDT [21]	0.4912	0.5273	0.2957	0.0221	0.1749	0.109
	IGA TSDT	0.4343	0.5387	0.2708	0.0213	0.2893	0.1101
∞	IGA FSDT	0.4337	0.5382	0.2705	0.0213	0.1775	0.0993
	ELS [19]	0.438	0.539	0.276	0.0216	0.337	0.141
	TSDT [20]	0.4343	0.5387	0.2708	0.0213	0.2897	0.112
	FSDT [21]	0.4337	0.5382	0.271	0.0213	0.178	0.101
∞	CLT [3]	0.4312	0.5386	0.2692	0.0213		
	IGA CLT	0.431	0.5386	0.2693	0.0213		

Table 1.1: IGA and analytical results for a $[0\ 90\ 90\ 0]$ square plate for CLT, FSDT and TSDT subjected to a sinusoidal load

Static analysis of antisymmetric cross-ply laminate $[0\ 90]_n$ and angle-ply laminate $[45\ -45]_n$

In this case we studied an antisymmetric cross-ply laminate of stacking sequence $[0\ 90]_n$ with *Material 1* and boundary conditions $SS - 1$ and an angle-ply laminate of stacking sequence $[45\ -45]_n$ with *Material 2* and boundary conditions $SS - 2$. Tables 1.2 and 1.3 show the results obtained with IGA and the analytical results for CLT, FSDT and TSDT for different thickness values. Numerical values are presented for $n=1, 2, 3$ whereas analytical values are presented for $n=1, 3$. In this case only the normalized center displacement was studied. As can be observed, the numerical results are the same as the analytical ones.

a/h	n	1	2	3		1	3
4	IGA FSDT	2.1492	1.5921	1.5473	FSDT [3]	2.1492	1.5473
	IGA TSDT	1.9985	1.6093	1.5411	TSDT [3]	1.9985	1.5411
10	IGA FSDT	1.2373	0.6802	0.6354	FSDT [3]	1.2373	0.6354
	IGA TSDT	1.2161	0.6865	0.6382	TSDT [3]	1.2161	0.6382
20	IGA FSDT	1.107	0.55	0.5517	FSDT [3]	1.107	0.5052
	IGA TSDT	1.1018	0.5517	0.506	TSDT [3]	1.1018	0.506
100	IGA FSDT	1.0653	0.5083	0.4635	FSDT [3]	1.0653	0.4635
	IGA TSDT	1.0651	0.5083	0.4635	TSDT [3]	1.0651	0.4635
∞	IGA CLT	1.0636	0.5065	0.4617	CLT [3]	1.0636	0.4618

Table 1.2: Normalized displacements for $[0\ 90]_n$ for CLT, FSDT and TSDT subjected to a sinusoidal load

a/h	n	1	2	3		1	3
4	IGA FSDT	1.1576	0.8715	0.8531	FSDT [3]	1.1576	0.8531
	IGA TSDT	1.0203	0.8747	0.8375	TSDT [3]	1.0203	0.8375
10	IGA FSDT	0.5773	0.2912	0.2728	FSDT [3]	0.5773	0.2728
	IGA TSDT	0.5581	0.2956	0.2745	TSDT [3]	0.5581	0.2745
20	IGA FSDT	0.4944	0.2083	0.1899	FSDT [3]	0.4944	0.1899
	IGA TSDT	0.4897	0.2095	0.1905	TSDT [3]	0.4897	0.1905
100	IGA FSDT	0.4678	0.1818	0.1633	FSDT [3]	0.4678	0.1633
	IGA TSDT	0.4676	0.1818	0.1634	TSDT [3]	0.4676	0.1634
∞	IGA CLT	0.4667	0.1806	0.1622	CLT [3]	0.4667	0.1622

Table 1.3: Normalized displacements for $[45 -45]_n$ for CLT, FSDT and TSDT subjected to a sinusoidal load

Eigenfrequencies of symmetric cross-ply laminate [0 90 0]

In this case a $[0 90 0]$ cross-ply laminate with *Material 1* and boundary conditions $SS - 1$ was studied. Several normalized eigenfrequencies were computed and compared with their respective analytical results, as presented in Table 1.4 for different thickness values. As it can be seen, numerical and analytical results are the same for CLT and FSDT. Additionally, numerical values for TSDT are presented.

a/h		CLT [3]	FSDT [3]	IGA CLT	IGA FSDT	IGA TSDT
10	Mode 1	15.228	12.163	15.228	12.163	11.797
	Mode 2	22.877	18.729	22.877	18.729	18.517
	Mode 3	40.299	30.932	40.299	30.932	29.369
	Mode 4	56.885	30.991	56.885	30.991	30.989
	Mode 5	60.911	34.434	60.911	34.434	33.023
	Mode 6	66.754	45.923	66.755	45.923	46.399
	Mode 7	71.522	42.585	71.522	42.582	41.66
100	Mode 1	15.228	15.183	15.228	15.183	15.175
	Mode 2	22.877	22.817	22.877	22.817	22.81
	Mode 3	40.299	40.153	40.299	40.153	40.149
	Mode 4	56.885	56.21	56.885	56.21	56.076
	Mode 5	60.911	60.211	60.911	60.211	60.076
	Mode 6	66.754	66.364	66.755	66.364	66.367
	Mode 7	71.522	70.764	71.522	70.764	70.639

Table 1.4: Normalized frequency of $[0 90 0]$ for CLT, FSDT and TSDT.

Frequencies were normalized by the following expression:

$$\bar{\omega} = \omega_i(a^2/h)\sqrt{\rho/E_2} \quad (1.29)$$

where ω_i is the considered frequency, ρ the density and a the edge length.

Eigenfrequencies of antisymmetric angle-ply laminate [45 -45]_n

Finally, a $[45 -45]_n$ angle-ply laminate with *Material 2* and boundary conditions $SS - 2$ was studied. Several normalized eigenfrequencies were computed and compared with their respective analytical results. They are presented in Table 1.5 for CLT, FSDT and TSDT for different thickness values. Numerical values for $n=1, 2, 3$ are given whereas analytical values are presented for $n=1, 3$. Numerical and analytical results are the same.

a/h	n	1	2	3		1	3
4	IGA FSDT	9.759	10.684	10.895	FSDT [3]	9.161	10.805
	IGA TSDT	13.044	10.651	19.025	TSDT [3]	9.759	10.895
10	IGA FSDT	13.263	18.463	19.025	FSDT [3]	13.044	19.025
	IGA TSDT	14.179	18.322	22.913	TSDT [3]	13.263	19.025
20	IGA FSDT	14.246	21.872	22.877	FSDT [3]	14.179	22.913
	IGA TSDT	14.618	21.806	24.741	TSDT [3]	14.246	22.877
100	IGA FSDT	14.621	23.454	24.739	FSDT [3]	14.618	24.741
	IGA TSDT	14.621	23.451	24.739	TSDT [3]	14.621	24.739

Table 1.5: Normalized first frequency for $[45 -45]_n$ for FSDT and TSDT.

1.4.2 Simply supported cylinder

In this subchapter, a simply supported cylinder of radius R and edges of length a (the 4 edges) with $SS - 1$ boundary conditions was studied. *Material 1* was used for cross-ply laminates of stacking sequences $[0\ 90]$, $[0\ 90\ 0]$ and $[0\ 90\ 90\ 0]$. The IGA model can be seen in Fig. 2.7. A 8×8 mesh with fourth order NURBS basis was used. The first normalized eigenmode (3.11) was computed for different values of the radius and two different thicknesses and plotted in Fig. 2.8. Table 1.6 shows the results obtained with IGA and the analytical results for FSDT and TSDT. As seen, numerical and analytical solutions are in good agreement. For the case of $R = 10^{30}$, the results are the same as the ones presented before (see Table 1.4). The analytical values for the TSDT presented in [16] assume that $1/R=0$ in the shear strains for a Naghdi-Shell formulation. This assumption was considered for the IGA of the TSDT solutions. Results for both theories are in good agreement with the numerical results for the selected mesh.

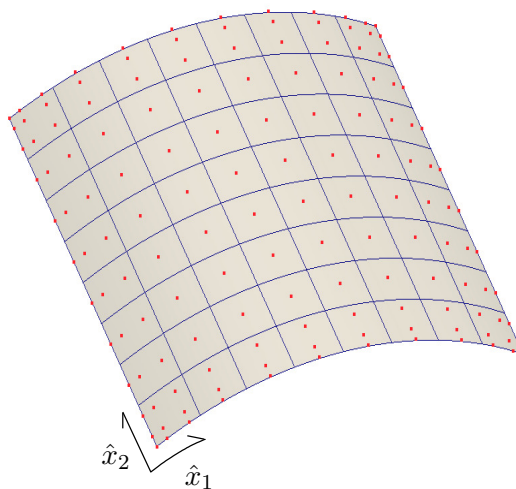


Figure 1.7: IGA simply supported cylinder model. Element mesh and control points.

R/a	a/h	[0 90]		[0 90 0]		[0 90 90 0]	
		100	10	100	10	100	10
5	IGA FSDT	16.669	8.913	20.333	12.209	20.362	12.268
	IGA TSDT	16.687	9.026	20.331	11.851	20.360	11.831
	FSDT [16]	16.668	8.908	20.332	12.207	20.361	12.267
	TSDT [16]	16.69	9.023	20.33	11.85	20.36	11.83
10	IGA FSDT	11.831	8.89	16.625	12.174	16.634	12.237
	IGA TSDT	11.838	8.981	16.619	11.809	16.631	11.790
	FSDT [16]	11.831	8.888	16.625	12.173	16.634	12.236
	TSDT [16]	11.84	8.979	16.62	11.8	16.63	11.79
20	IGA FSDT	10.265	8.891	15.557	12.166	15.559	12.23
	IGA TSDT	10.268	8.971	15.548	11.8	15.549	11.784
	FSDT [16]	10.265	8.89	15.556	12.166	15.559	12.228
	TSDT [16]	10.27	8.972	15.55	11.79	15.55	11.78
100	IGA FSDT	9.711	8.898	15.198	12.163	15.199	12.227
	IGA TSDT	9.712	8.978	15.19	11.797	15.188	11.784
	FSDT [16]	9.711	8.897	15.198	12.163	15.199	12.227
	TSDT [16]	9.712	8.975	15.19	11.79	15.19	11.78
Plate $R=10^{30}$	IGA FSDT	9.687	8.9	15.183	12.163	15.184	12.227
	IGA TSDT	9.688	8.98	15.175	11.797	15.173	11.784
	FSDT [16]	9.687	8.9	15.183	12.162	15.184	12.226
	TSDT [16]	9.688	8.976	15.17	11.79	15.17	11.78

Table 1.6: Normalized first frequency for [90 0], [0 90 0] and [0 90 90 0] simply supported cylinder for FSDT and TSDT.

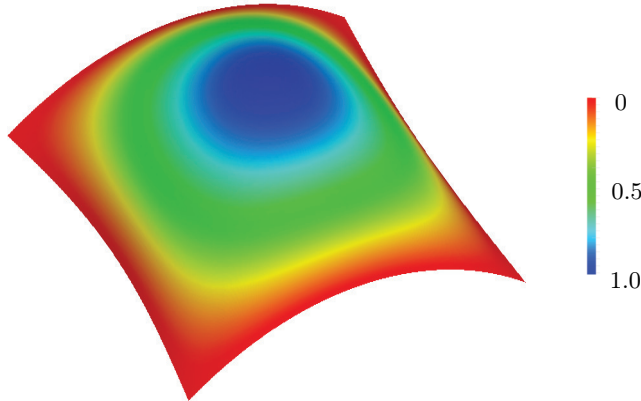


Figure 1.8: Mode 1 of simply supported cylinder.

1.4.3 Clamped cylinder

Static analysis of isotropic clamped cylinder

A cylinder of radius R and edge length L totally clamped on its 4 edges was studied for an isotropic material subjected to a uniform transverse load. The IGA model can be seen in Fig. 2.9, for two considered meshes. It is assumed that $R = 100$ in, $L = 20$ in, $h = 0.125$ in, $2\alpha = 0.2$ rad, which is the total angle that defines the circular edges ($a = 2\alpha R$) and $q = 0.04$ psi. The material used has the following ply properties:

Material 3

$E=0.45 \cdot 10^6$ psi, $\nu=0.30$.

The clamped boundary conditions are defined as:

$CC - 1$:

$$\begin{aligned}
 u_0(0, y) = u_0(a, y) = u_0(x, 0) = u_0(x, b) = 0 \\
 v_0(0, y) = v_0(a, y) = v_0(x, 0) = v_0(x, b) = 0 \\
 \theta_x(0, y) = \theta_x(a, y) = \theta_x(x, 0) = \theta_x(x, b) = 0 \\
 \theta_y(0, y) = \theta_y(a, y) = \theta_y(x, 0) = \theta_y(x, b) = 0 \\
 w_0(0, y) = w_0(a, y) = w_0(x, 0) = w_0(x, b) = 0
 \end{aligned} \tag{1.30}$$

This is a relatively thin shell, so all the solutions should give the same results. Solutions for CLT, FSDT and TSDT are quite similar for this thickness, since the shear deformation is negligible. Table 1.7 shows the results obtained with IGA for 8 x 8 and 16 x 16 element meshes, for NURBS basis orders 4-th, 5-th and 6-th. The results are compared with other FEM results obtained with an educational version of the Software [22] and the one in [3]. As expected, a refined mesh should be used for fourth order NURBS and shear deformation theories. For CLT no additional refinement is required, since this formulation does not provide any locking; whereas for shear deformation cases, the locking phenomena tends to vanish as the NURBS order increases. The deformation is plotted in Fig. 2.10.

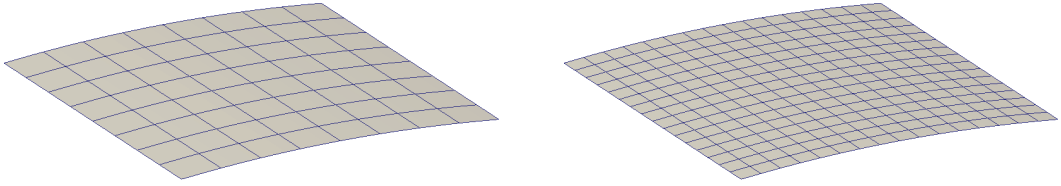


Figure 1.9: IGA clamped cylinder model. Meshes for 8x8 and 16x16 elements.

NURBS order	Elements	CLT	FSDT	TSDT
4th	IGA 8x8	1.1352	1.1327	1.133
	IGA 16x16	1.1351	1.1348	1.1345
5th	IGA 8x8	1.1351	1.1345	1.1338
	IGA 16x16	1.1351	1.1348	1.1344
6th	IGA 8x8	1.1351	1.1348	1.1354
	IGA 16x16	1.1351	1.1348	1.1343
-	FEM 16x16 [3]	1.1349	-	-
-	FEM 64x64 [22]	1.1354	1.1351	-

Table 1.7: Maximum displacement (in) at isotropic clamped cylinder subjected to a uniform transverse load.

Static analysis of complete clamped cylinder

A cylinder of radius R and edge length L totally clamped was studied for a [0] cross-ply laminate, with $CC - 1$ boundary conditions at $\hat{x}_1 = 0$ and $\hat{x}_1 = L$. The IGA model can be seen in Fig. 1.11. A 32 x 8 mesh with fourth order NURBS basis was used. It was assumed that $R/L = 1$, $R/h = 20$ and $h = 1$ in. The material used has the following ply properties:

Material 4

$$\begin{aligned}
 E_1=7.5 \cdot 10^6 \text{ psi}, E_2=2.0 \cdot 10^6 \text{ psi}, G_{12}=1.25 \cdot 10^6 \text{ psi}, \\
 G_{13}=G_{23}=0.625 \cdot 10^6 \text{ psi}, \nu_{12}=\nu_{13}=0.25.
 \end{aligned}$$

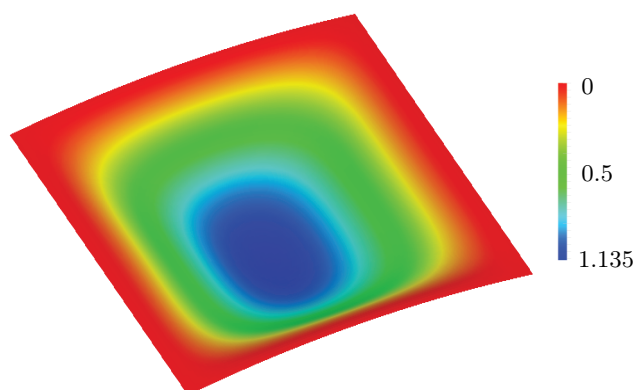


Figure 1.10: Deformation (in) of clamped cylinder subjected to a uniform transverse load.

A uniform internal pressure of $6.41/\pi$ ksi was applied. The deformation was computed and plotted in Fig. 1.12. Table 1.8 shows the results obtained with IGA and other FEM results. The CLT results are in good agreement for FEM and IGA. Additionally, solutions for FSDT and TSDT are presented.

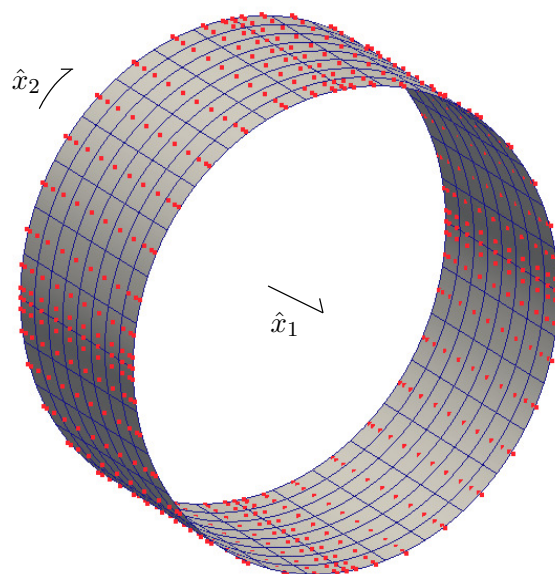


Figure 1.11: IGA clamped complete cylinder model. Element mesh and control points.

	CLT[23]	FSDT[3]	IGA CLT	IGA FSDT	IGA TSDT
[0]	0.3666	0.3754	0.3671	0.3748	0.3742

Table 1.8: Maximum displacement (in) for [0] clamped cylinder with internal pressure for CLT, FSDT and TSDT.

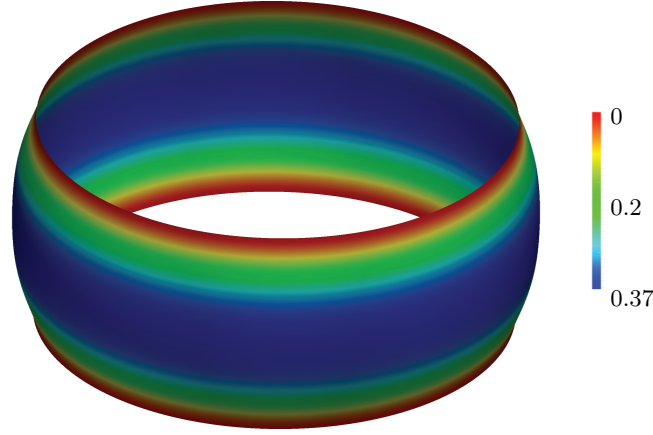


Figure 1.12: Deformation (in) of complete cylinder by internal pressure.

Eigenmode analysis of clamped complete cylinder

Finally, another cylinder of radius R and edge length L totally clamped was studied for $[0\ 90]$ and $[90\ 0]$ cross-ply laminates, with $CC - 1$ boundary conditions at $\hat{x}_1 = 0$ and $\hat{x}_1 = L$. The IGA model can be seen in Fig. 1.11. A 32×8 mesh with fourth order NURBS basis was used. It was assumed that $R/L = 1$, $R/h = 60$ and $h = 1$ in. The material used has the following ply properties:

Material 5

$$E_1=10E_2, G_{12}=G_{13}=0.6E_2, G_{23}=0.5E_2, \nu_{12}=\nu_{13}=0.25.$$

The first normalized eigenmode (3.12) was computed and plotted in Fig. 2.11. Table 1.9 shows the results obtained with IGA and the analytical results for FSDT and TSDT. Superindex 1 refers to the general solution while superindex 2 is for the case in which $1/R = 0$ in the shear strains, for a Naghdi-Shell formulation [3]. Numerical results are in good agreement with the analytical ones for the selected mesh.

$$\bar{\omega} = \omega_i(L^2/10h)\sqrt{\rho/E_2} \tag{1.31}$$

where ω_i is the considered frequency and ρ the density and L the cylinder length.

	FSDT[3]	IGA FSDT ¹	IGA FSDT ²	IGA TSDT ¹	IGA TSDT ²
[0 90]	3.266	3.248	3.268	3.249	3.264
[90 0]	3.242	3.208	3.244	3.209	3.237

Table 1.9: Normalized first frequency for $[0\ 90]$ and $[90\ 0]$ clamped complete cylinder for FSDT and TSDT.

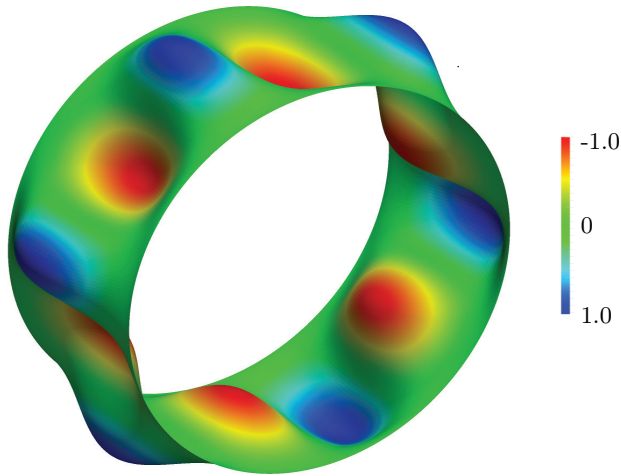


Figure 1.13: Mode 1 of clamped complete cylinder.

1.5 Conclusions

In this contribution, a composite shell is implemented with an IGA NURBS-based formulation. The most widely ESL composite theories are analyzed, particularly the TSDT shell, introduced in this paper. Higher-order NURBS ensure the continuity requirements inherent to the different ESL theories, and serve to avoid numerical locking. Numerical and analytical results were compared for a set of benchmark and FEM solutions to corroborate the efficiency of IGA, giving the same results for relative small meshes. The results underline IGA in contrast to the classic FEM as a very promising approach for double-curved composite shells, especially the TSDT, which can be easily implemented and is more accurate than the FSDT.

Chapter 2

An Isogeometric higher-order locking-free shell

In this chapter an improvement in terms of numerical accuracy is performed for a TSDT shell. The well known locking phenomenon is avoided with the use of a locking-free theory in terms of shear-locking, in combination with a numerical method (projection technique) to avoid the curvature-locking. The results presented in this chapter compare this strategy with the standard IGA formulation developed in the previous chapter, being this new one more accurate, specially for lower order NURBS. The methodology is also valid for composites, but for the sake of brevity, only isotropic cases are presented. In a future paper these results will be extended to composite cases, similar to those presented in Chapter 1.

Abstract

Isogeometric analysis (IGA) represents an important improvement for shell analysis due to its advantage to represent complex geometries. However, IGA formulation is sensible of locking effects, as well as happens with standard finite element analysis (FEA). In this work a locking-free third order shear deformation theory (TSDT) shell is proposed. Particularly, shear-locking is avoided through a discrete hierarchic vector formulation, whereas the curvature-locking is avoided with a projection technique. Linear static and dynamic analyses are performed and compared with some known analytical and FEM solutions to demonstrate the efficiency of isogeometric analysis for the TSDT and for the most widely used equivalent single layer theories (ESL), that is, the classical laminate theory (CLT) and the first order shear deformation theory (FSDT).

Keywords : Isogeometric Analysis; Shell; Higher-Order Theory; Locking-free; Hierarchic difference vector; Projection methods

2.1 Introduction

Shell structures are present in many engineering applications because of its geometric characteristics. Particularly, in the area of composite materials they have become more popular in the recent decades due to their properties (relationship strength-stiffness, weight, etc.).

The development of the finite element method (FEM) made possible solving plate and shell theories, required to design composites. Particularly, shell theories, developed mostly with the so-called equivalent single layer theories (ESL), offer a good balance between the accuracy of the results from the numerical point of view and the time involved. The most popular ones entail Love-Kirchhoff

elements, with the classical laminate theory (CLT) and Reissner-Mindlin elements, with a first order shear deformation theory (FSDT). They have been widely used, providing acceptable results. For an enhanced approach to stresses, refined ESL theories were developed, constituting the so-called higher-order deformation theories (HOT). Interested reader can find more information about these materials in [1] and [3] and more details on ESL theories on [2] and [3].

On the other hand computer-aided design (CAD), computer graphics (CG) and animations, eventually provided very good approximations of general complex geometries through the use of splines. Isogeometric analysis (IGA) achieves the union between FEA with CAD, CG and animation. Developed by Tom Hughes and co-workers, this method combines geometry and analysis using tools common to both. That is, the geometric basis functions are also used as the approximation functions required for analysis. Interested readers can find more details in [4, 5].

The author presented in [24] a TSDT shell, where locking is avoided through the use of higher-order NURBS. However, as happens with standard FEA, the locking phenomenon has to be considered, specially for lower order NURBS. All the classical techniques used to avoid this problem, can be applied for IGA. Particularly, the Ref. [25] introduced the hierarchic difference vector for FSDT shells to avoid shear-locking. In [26], the authors also used this concept combined with DSG and projection techniques to avoid the curvature-locking for a FSDT.

2.2 Isogeometric analysis

Non uniform rational B-Splines (NURBS) are a standard tool for representing curves and surfaces in computer-aided design and computer graphics. In this section, a short description of the isogeometric analysis concepts is briefly presented. More details are found in the fundamental works of Hughes and co-workers [4, 5, 6, 7, 8] for isogeometric analysis; and in Piegl and Tiller [9], Rogers [10], Farin [11] and Cohen [12] for a comprehensive review of the underlying geometric concepts and algorithms.

2.2.1 B-Splines

A B-spline is a non-interpolating, piecewise polynomial curve. It is defined by a knot vector Ξ , a set of control points, \mathbf{B}_i ($i=1,2,\dots,n$) and a polynomial degree. The knot vector is a set of non-decreasing real numbers representing points in the parametric space of the curve:

$$\Xi = \{\xi_1, \xi_2, \dots, \xi_{n+p+1}\}, \quad (2.1)$$

where p is the degree of the curve and n is the number of basis functions, corresponding to the \mathbf{B}_i control points.

B-Spline basis functions are defined recursively starting from $p=0$ (piecewise constant) using the Cox-de Boor formula:

$$N_{i,0}(\xi) = \begin{cases} 1 & \text{if } \xi \leq \xi < \xi_{i+1} \\ 0 & \text{otherwise} \end{cases} \quad (2.2)$$

and for $p \geq 1$:

$$N_{i,p}(\xi) = \frac{\xi - \xi_i}{\xi_{i+p} - \xi_i} N_{i,p-1}(\xi) + \frac{\xi_{i+p+1} - \xi}{\xi_{i+p+1} - \xi_{i+1}} N_{i+1,p-1}(\xi) \quad (2.3)$$

Figure 2.1 shows an example of cubic basis functions with an open knot vector.

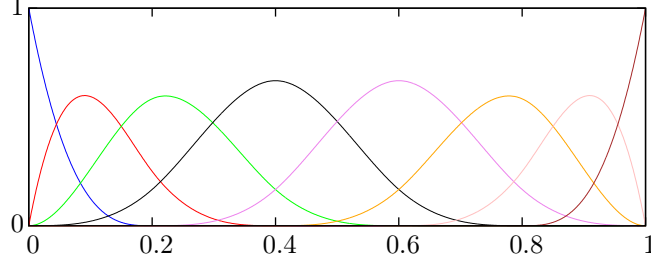


Figure 2.1: Cubic basis functions for open knot vector $\Xi = \{0, 0, 0, 0, 1/5, 2/5, 3/5, 4/5, 1, 1, 1, 1\}$.

2.2.2 B-Spline curves and surfaces

A B-Spline curve is constructed through a linear combination of B-Spline basis functions and the control points. Figure 2.2 shows an example of a B-Spline curve with its control points.

$$\mathbf{C}(\xi) = \sum_{i=1}^n N_{i,p}(\xi) \mathbf{B}_i \quad (2.4)$$

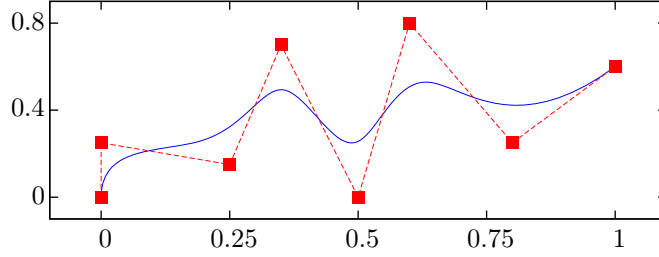


Figure 2.2: B-Spline curve for open knot vector $\Xi = \{0, 0, 0, 0, 1/5, 2/5, 3/5, 4/5, 1, 1, 1, 1\}$.

B-Spline surface basis are computed by means of the tensor product of single univariate B-Spline basis functions. Thus, two individual knot vectors $\Xi = \{\xi_1, \xi_2, \dots, \xi_{n+p+1}\}$ and $\mathcal{H} = \{\eta_1, \eta_2, \dots, \eta_{m+q+1}\}$, and a set of $n \cdot m$ control points $\mathbf{B}_{i,j}$ ($i=1,2,\dots,n; j=1,2,\dots,m$), define the B-Spline surface:

$$\mathbf{S}(\xi, \eta) = \sum_{i=1}^n \sum_{j=1}^m N_{i,p}(\xi) M_{j,q}(\eta) \mathbf{B}_{i,j} \quad (2.5)$$

2.2.3 NURBS

Non uniform rational B-Splines (NURBS) constitute an improvement upon B-splines, since they can represent more general geometries. Constructed as a projection in \mathbb{R}^d of a B-Spline of \mathbb{R}^{d+1} , NURBS basis can be defined. Then a space point of the B-Spline curve $\mathbf{B}_i^w(x_i, y_i, z_i, w_i)$ is geometrically projected into $\mathbf{B}_i(w_i x_i, w_i y_i, w_i z_i)$. Similarly to B-Spline curves and surfaces, NURBS-based ones are defined as:

$$\mathbf{C}(\xi) = \frac{\sum_{i=1}^n N_{i,p}(\xi) w_i \mathbf{B}_i}{\sum_{i=1}^n N_{i,p}(\xi) w_i} \quad (2.6)$$

$$\mathbf{S}(\xi, \eta) = \frac{\sum_{i=1}^n \sum_{j=1}^m N_{i,p}(\xi) M_{j,q}(\eta) w_{i,j} \mathbf{B}_{i,j}}{\sum_{i=1}^n \sum_{j=1}^m N_{i,p}(\xi) M_{j,q}(\eta) w_{i,j}} \quad (2.7)$$

2.2.4 Mesh refinement

NURBS-based refinements can be done by knot insertion (h refinement) or order increase (p refinement) [5]. Particularly the k -refinement combines order increase in the first place and knot insertion of multiplicity one in the second place. This refinement guarantees C^{p-1} continuity through the entire domain. Figure 2.3 shows an example of a cylindrical surface built with NURBS and the element, and control mesh before and after a k -refinement.

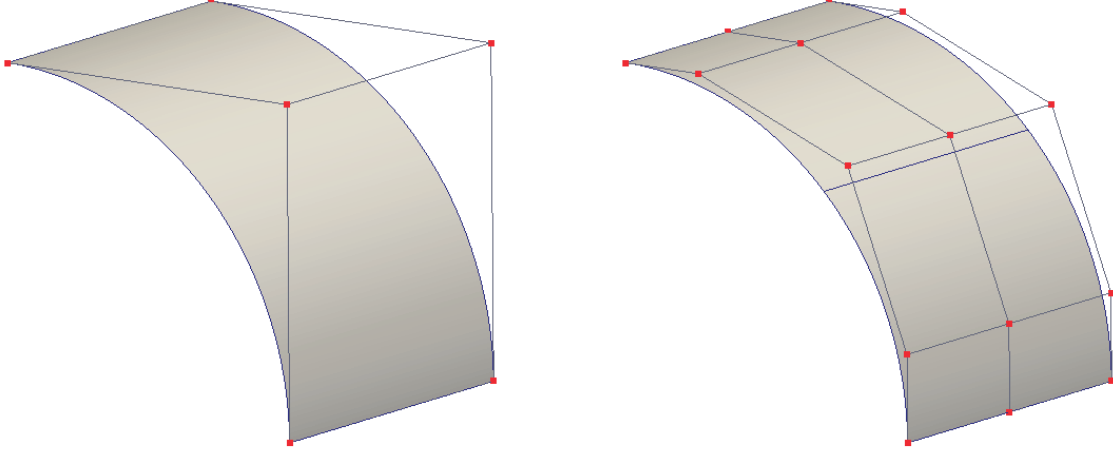


Figure 2.3: NURBS-based cylindrical surface for $\Xi = \{0, 0, 0, 1, 1, 1\}$ and $\mathcal{H} = \{0, 0, 1, 1\}$. Element and control mesh before and after a k -refinement.

2.3 Shell formulation

In this section the laminate shell theory is briefly exposed. First, a description at the ply level is introduced; then, the shell kinematics are described for the adopted ESL theories in order to build the equations of the laminate.

2.3.1 Ply description

ESL layer theories assume that each composite ply behaves as a case of a plane-stress problem, neglecting the transverse normal strain ($\epsilon_{33}=0$). The stress-strain relation for an orthotropic ply can be expressed with respect the ply/shell selected orthonormal axes as:

$$\begin{aligned}
 \bar{Q}_{11} &= Q_{11}\cos^4\theta + 2(Q_{12} + 2Q_{66})\sin^2\theta\cos^2\theta + Q_{22}\sin^4\theta \\
 \bar{Q}_{12} &= (Q_{11} + Q_{22} - 4Q_{66})\sin^2\theta\cos^2\theta + Q_{12}(\sin^4\theta + \cos^4\theta) \\
 \bar{Q}_{22} &= Q_{11}\sin^4\theta + (2Q_{12} + 2Q_{26})\sin^2\theta\cos^2\theta + Q_{22}\cos^4\theta \\
 \bar{Q}_{16} &= (Q_{11} - Q_{12} - 2Q_{66})\sin\theta\cos^3\theta + (Q_{12} - Q_{22} + 2Q_{66})\sin^3\theta\cos\theta \\
 \bar{Q}_{26} &= (Q_{11} - Q_{12} - 2Q_{66})\sin^3\theta\cos\theta + (Q_{12} - Q_{22} + 2Q_{66})\sin\theta\cos^3\theta \\
 \bar{Q}_{66} &= (Q_{11} + Q_{22} - 2Q_{12} - 2Q_{66})\sin^2\theta + \cos^2\theta + Q_{66}(\sin^4\theta + \cos^4\theta) \\
 \bar{Q}_{44} &= Q_{44}\cos^2\theta + Q_{55}\sin^2\theta \\
 \bar{Q}_{45} &= (Q_{55} - Q_{44})\cos\theta\sin\theta \\
 \bar{Q}_{55} &= Q_{55}\cos^2\theta + Q_{44}\sin^2\theta
 \end{aligned} \tag{2.8}$$

where θ is the angle between the fiber and the first ply/shell axis, plotted in Fig. 2.4.

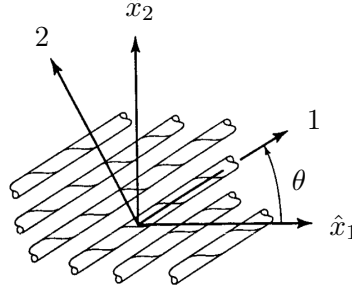


Figure 2.4: Orientation of axes at ply level.

The matrix $\bar{\mathbf{Q}}_r$, where r denotes the corresponding ply, is also called the reduced stiffness ply matrix, which can be rewritten in terms of normal and transverse ply stiffness as:

$$\bar{\mathbf{Q}}_r = \begin{bmatrix} \bar{\mathbf{Q}}_{r1} & \mathbf{0} \\ \mathbf{0} & \bar{\mathbf{Q}}_{r2} \end{bmatrix}; \quad (2.9)$$

where:

$$\bar{\mathbf{Q}}_{r1} = \begin{bmatrix} \bar{Q}_{11} & \bar{Q}_{12} & \bar{Q}_{16} \\ \bar{Q}_{12} & \bar{Q}_{22} & \bar{Q}_{26} \\ \bar{Q}_{16} & \bar{Q}_{26} & \bar{Q}_{66} \end{bmatrix}; \quad \bar{\mathbf{Q}}_{r2} = \begin{bmatrix} \bar{Q}_{44} & \bar{Q}_{45} \\ \bar{Q}_{45} & \bar{Q}_{55} \end{bmatrix} \quad (2.10)$$

2.3.2 Laminate description

The laminate equations will be deduced by considering the corresponding ESL theory. Although CLT, FSDT and TSDT are implemented in the present shell, only a description of the TSDT is exposed, since it is more general and can lead to the other ones by simplification of the TSDT.

The undeformed shell geometry can be described by:

$$\mathbf{X}(\xi, \eta, \zeta) = \bar{\mathbf{X}}(\xi, \eta) + \zeta \mathbf{A}_3 = \bar{\mathbf{X}}(\xi, \eta) + \mathbf{N} \quad (2.11)$$

and the deformed one can be described by:

$$\mathbf{x}(\xi, \eta, \zeta) = \mathbf{X}(\xi, \eta, \zeta) + \mathbf{u}(\xi, \eta, \zeta) \quad (2.12)$$

being:

$$\mathbf{x}(\xi, \eta, \zeta) = \bar{\mathbf{x}}(\xi, \eta) + \mathbf{n} \quad (2.13)$$

where $\bar{\mathbf{X}}$ and $\bar{\mathbf{x}}$ represent the mid-surface positions for the reference and deformed configurations; $\{\mathbf{A}_\xi, \mathbf{A}_\eta\}$ and $\{\mathbf{a}_\xi, \mathbf{a}_\eta\}$ are the convected unitary vectors for the reference and deformed configurations of the manifold; \mathbf{A}_3 and \mathbf{a}_3 are the unitary vectors orthogonal to the respective mid-surface; \mathbf{N} is the normal position vector and \mathbf{n} is the director vector (they define the position of a body position P respect to its reference configuration; P' in the deformed one); $\mathbf{u}(\xi, \eta, \zeta)$ are the spatial displacements. Finally ξ and η are the manifold coordinates, whereas ζ is the normal coordinate to the mid-surface. All these concepts are illustrated in Figures 2.5 and 2.6.

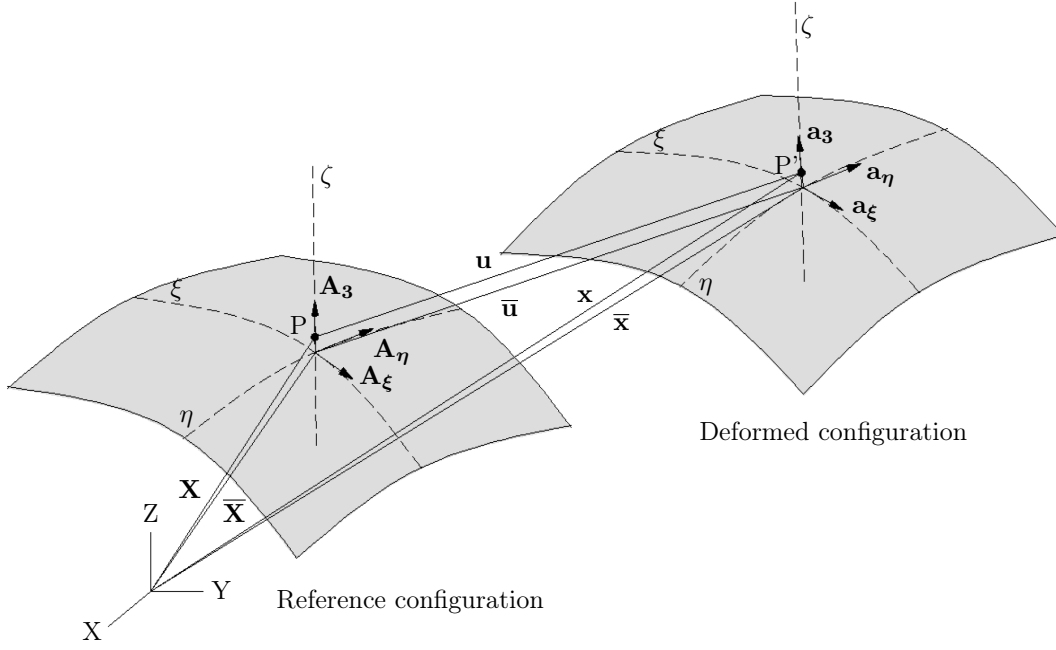


Figure 2.5: Natural local bases for reference and deformed configurations.

The director vector \mathbf{n} is defined as:

$$\mathbf{n} = \sum_{i=1}^{\infty} \zeta^i \mathbf{n}_i \quad (2.14)$$

However, in this case an approximation until the third member is performed, resulting:

$$\mathbf{n} = \zeta \mathbf{n}_1 + \zeta^2 \mathbf{n}_2 + \zeta^3 \mathbf{n}_3 \quad (2.15)$$

Expressing the director vector in terms of the the normal position vector \mathbf{N} and the difference between them \mathbf{d} , it is obtained:

$$\mathbf{n} = \mathbf{N} + \mathbf{d} \quad (2.16)$$

$$\mathbf{d} = \zeta(\boldsymbol{\psi} + \mathbf{w}_1) + \zeta^2 \mathbf{w}_2 + \zeta^3 \mathbf{w}_3 \quad (2.17)$$

where $\boldsymbol{\psi}$ is the CLT rotation and \mathbf{w}_1 , \mathbf{w}_2 , \mathbf{w}_3 are the components of the hierarchic difference vector, associated to the different order. The hierarchic difference vector can be defined as:

$$\mathbf{w} = \zeta \mathbf{w}_1 + \zeta^2 \mathbf{w}_2 + \zeta^3 \mathbf{w}_3 \quad (2.18)$$

Since the shell does not allow deformation in the thickness direction, the difference vector depends only on the manifold components. Therefore:

$$\mathbf{w} = w^1 \mathbf{A}_1 + w^2 \mathbf{A}_2 \quad (2.19)$$

The second and third term of Equation (2.18) represent the quadratic and cubic displacements, inherit to the TSDT. However if it is assumed that the section is free of tangential stress at the top and the

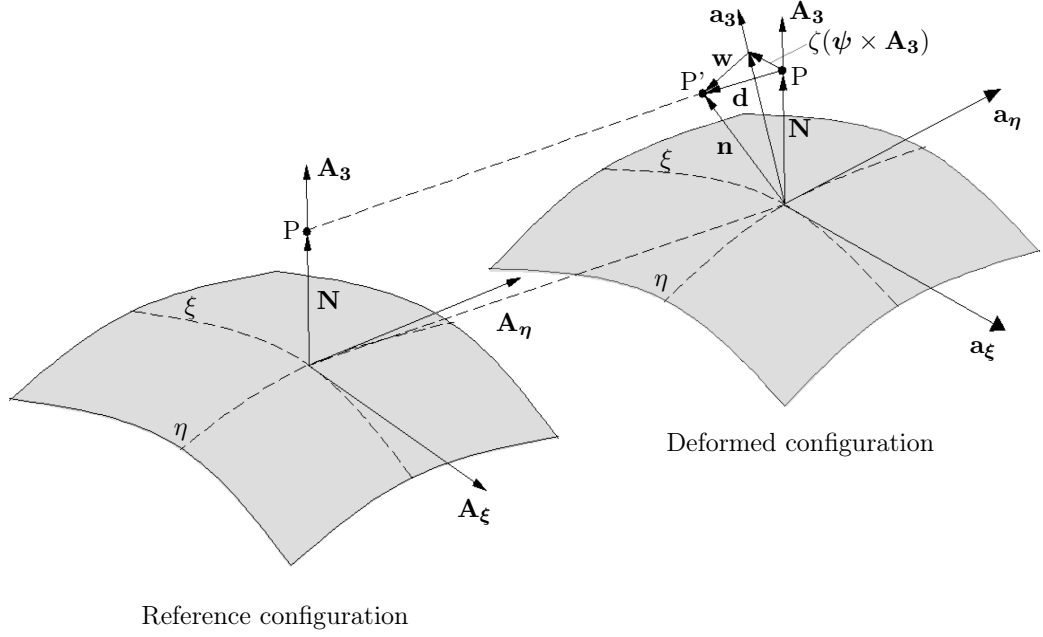


Figure 2.6: Hierarchic difference vector.

bottom of the laminate [3] ($\tau_{13}(\pm h/2) = \tau_{23}(\pm h/2) = 0$), the following results are obtained:

$$\mathbf{w}_2 = \mathbf{0} \quad (2.20)$$

$$\mathbf{w}_3 = -\frac{4}{3h^2} \mathbf{w}_1 = \alpha \mathbf{w}_1 \quad (2.21)$$

Thus having the TSDT the same number of d.o.f. as the FSDT.

The linearized strain tensor can be expressed as:

$$\epsilon_{ij} = \frac{1}{2} (\mathbf{G}_i \mathbf{u}_{,j} + \mathbf{G}_j \mathbf{u}_{,i}) \quad (2.22)$$

The expression of the displacements according to this new theory is:

$$\mathbf{u} = \bar{\mathbf{u}} + \zeta (\boldsymbol{\psi} \times \mathbf{A}_3) + \mathbf{w}_1 (\zeta + \alpha \zeta^3) \quad (2.23)$$

The components of the strain tensor are:

$$\begin{aligned} \epsilon_{\xi\xi} &= \mathbf{A}_\xi \mathbf{u}_{,\xi} + \zeta \mathbf{A}_\xi (\boldsymbol{\psi}_{,\xi} \times \mathbf{A}_3) + \mathbf{A}_\xi \mathbf{w}_{1,\xi} (\zeta + \alpha \zeta^3) \\ \epsilon_{\eta\eta} &= \mathbf{A}_\eta \mathbf{u}_{,\eta} + \zeta \mathbf{A}_\eta (\boldsymbol{\psi}_{,\eta} \times \mathbf{A}_3) + \mathbf{A}_\eta \mathbf{w}_{1,\eta} (\zeta + \alpha \zeta^3) \\ \gamma_{\xi\eta} &= \mathbf{A}_\eta \mathbf{u}_{,\xi} + \zeta \mathbf{A}_\eta (\boldsymbol{\psi}_{,\xi} \times \mathbf{A}_3) + \mathbf{A}_\eta \mathbf{w}_{1,\xi} (\zeta + \alpha \zeta^3) + \mathbf{A}_\xi \mathbf{u}_{,\eta} + \zeta \mathbf{A}_\xi (\boldsymbol{\psi}_{,\eta} \times \mathbf{A}_3) + \mathbf{A}_\xi \mathbf{w}_{1,\eta} (\zeta + \alpha \zeta^3) \\ \gamma_{\xi\xi} &= \mathbf{A}_\xi \mathbf{w}_1 (1 + 3\alpha \zeta^2) \\ \gamma_{\eta\zeta} &= \mathbf{A}_\eta \mathbf{w}_1 (1 + 3\alpha \zeta^2) \end{aligned} \quad (2.24)$$

It has to be kept in mind that quadratic and higher terms in ζ multiplied by $\mathbf{A}_{3,i}$ have been neglected. This simplification is quite normal for shell theories, since $\mathbf{A}_{3,i}$ is proportional to the curvatures of the mid-surface.

Particularly, the FSDT theory can be obtained by assuming $\alpha = 0$. The CLT can be obtained by assuming $\mathbf{w}_1 = 0$.

By integration through the thickness, the laminate strain-stress relationships can be obtained and then expressed in the local system as:

$$\begin{bmatrix} \mathbf{N}_0 \\ \mathbf{M}_0 \\ \mathbf{P}_0 \end{bmatrix} = \begin{bmatrix} \mathbf{A} & \mathbf{B} & \mathbf{E} \\ \mathbf{B} & \mathbf{D} & \mathbf{F} \\ \mathbf{E} & \mathbf{F} & \mathbf{H} \end{bmatrix} \begin{bmatrix} \epsilon_0^0 \\ \epsilon_0^1 \\ \epsilon_0^3 \end{bmatrix}; \quad \begin{bmatrix} \mathbf{Q}_0 \\ \mathbf{R}_0 \end{bmatrix} = \begin{bmatrix} \mathbf{A}_s & \mathbf{D}_s \\ \mathbf{D}_s & \mathbf{F}_s \end{bmatrix} \begin{bmatrix} \gamma_0^0 \\ \gamma_0^1 \end{bmatrix} \quad (2.25)$$

where \mathbf{N}_0 , \mathbf{M}_0 , \mathbf{P}_0 , \mathbf{Q}_0 and \mathbf{R}_0 are the resultant forces and moments, and ϵ_0^i and γ_0^i are the in-plane strains, with:

$$(\mathbf{A}, \mathbf{B}, \mathbf{D}, \mathbf{E}, \mathbf{F}, \mathbf{H}) = \sum_{r=1}^n \int_{-z_r}^{z_r} \bar{\mathbf{Q}}_{r1}(1, z, z^2, z^3, z^4, z^6) dz \quad (2.26)$$

$$(\mathbf{A}_s, \mathbf{D}_s, \mathbf{F}_s) = \sum_{r=1}^n \int_{-z_r}^{z_r} \bar{\mathbf{Q}}_{r2}(1, z^2, z^4) dz \quad (2.27)$$

Equations (2.26)-(2.27) represent the constitutive matrices of the laminate for the TSDT.

2.3.3 FEM implementation

In the context of shells, two well known kinds of locking have to be considered. Shear-locking and curvature-locking tend to appear as the thickness or the curvature diminishes. In [24] the locking is avoided with the use of higher-order NURBS, which work pretty well for moderate thicknesses. However, low order NURBS and very thin thicknesses do not avoid this problem unless the mesh is relative big. As well as with standard FEA, several techniques were developed to avoid this problem (see [27, 28]), which also are adequate for IGA.

The shell equations developed in this paper, based on the hierarchic discrete difference vector [25, 26], do not present shear-locking and only the curvature-locking has to be avoided. For this purpose, a mixed formulation based on the Hellinger-Reissner variational principle is applied, which weak form can be described as follows:

$$\Pi_{HR}^h(\epsilon, \mathbf{u}) = \frac{1}{2} \int_{\Omega} \epsilon : \mathbf{C} : \epsilon d\Omega + \int_{\Omega} \epsilon : \mathbf{C} : (\epsilon^d - \epsilon) d\Omega - \int_{\Gamma} \mathbf{u} \mathbf{f} d\Gamma \quad (2.28)$$

which by minimization leads to:

$$\begin{aligned} \delta \Pi_{HR}^h(\epsilon, \mathbf{u}) &= 0 \\ \int_{\Omega} \delta \epsilon : \mathbf{C} : (\epsilon^d - \epsilon) d\Omega + \int_{\Omega} \delta \epsilon^d : \mathbf{C} : \epsilon d\Omega - \int_{\Gamma} \delta \mathbf{u} \mathbf{f} d\Gamma &= 0 \end{aligned} \quad (2.29)$$

By substitution of the projected strain $\epsilon = \tilde{\mathbf{N}}\boldsymbol{\beta}$ and the displacement based one $\epsilon^d = \mathbf{B} \mathbf{q}$, equation (2.29) can be rewritten as:

$$\begin{aligned} \delta \Pi_{HR}^h(\epsilon, \mathbf{u}) &= \mathbf{0} \\ \delta \boldsymbol{\beta}^T \int_{\Omega} [\tilde{\mathbf{N}}^T \mathbf{C} \mathbf{B}] \mathbf{q} - [\tilde{\mathbf{N}}^T \mathbf{C} \tilde{\mathbf{N}}] \boldsymbol{\beta} d\Omega + \delta \mathbf{q}^T \left(\int_{\Omega} [\mathbf{B}^T \mathbf{C} \tilde{\mathbf{N}}] \boldsymbol{\beta} d\Omega - \int_{\Gamma} \mathbf{N}^T \mathbf{f} d\Gamma \right) &= 0 \end{aligned} \quad (2.30)$$

Finally, this expression can be expressed in a matrix form as:

$$\begin{bmatrix} \mathbf{K}_{\mathbf{uu}} & \mathbf{K}_{\mathbf{u}\beta} \\ \mathbf{K}_{\beta\mathbf{u}} & \mathbf{K}_{\beta\beta} \end{bmatrix} \begin{bmatrix} \mathbf{q} \\ \beta \end{bmatrix} = \begin{bmatrix} \mathbf{F} \\ \mathbf{0} \end{bmatrix} \quad (2.31)$$

being:

$$\begin{aligned} \mathbf{K}_{\mathbf{uu}} &= \int_{\Omega} [\mathbf{B}^T \mathbf{C} \mathbf{B}] d\Omega; & \mathbf{K}_{\mathbf{u}\beta} &= \int_{\Omega} [\mathbf{B}^T \mathbf{C} \tilde{\mathbf{N}}] d\Omega \\ \mathbf{K}_{\beta\mathbf{u}} &= \int_{\Omega} [\tilde{\mathbf{N}}^T \mathbf{C} \mathbf{B}] d\Omega; & \mathbf{K}_{\beta\beta} &= - \int_{\Omega} [\tilde{\mathbf{N}}^T \mathbf{C} \tilde{\mathbf{N}}] d\Omega \\ \mathbf{F} &= \int_{\Gamma} \mathbf{N}^T \mathbf{f} d\Gamma \end{aligned} \quad (2.32)$$

The scheme for the projection is the Table 2.1. The matrix $\mathbf{K}_{\mathbf{uu}}$ is referred to unprojected strains.

	ξ	η
\mathbf{u}	p	q
$\epsilon_{\xi\xi}$	$p-1$	q
$\epsilon_{\eta\eta}$	p	$q-1$
$\gamma_{\xi\eta}$	$p-1$	$q-1$

Table 2.1: Scheme for the projection.

2.4 Numerical results

In this section some benchmark static and dynamic problems analyzed with the introduced TSdT, are compared with the standard IGA formulation. Additionally, CLT and FSdT are theories also considered. For all the FSdT problems, a shear correction factor $K=5/6$ was used; TSdT do not require any shear correction factor. First of all, a flat analysis is performed in order to proof that element is free of shear locking. Additionally the results are compare with standard NURBS. Regarding the notation, the symbol (*) will denote the hierarchic discrete difference vector, in combination with the projection technique in all the following figures and tables.

2.4.1 Simply supported plate

A simply supported isotropic rectangular plate of dimension $a \times b$ was studied. The plate was assumed to be square ($a=b=1$). The IGA model can be seen in Fig. 2.7. A 8x8 mesh with fourth order NURBS basis was used. The material assumed properties are:

Material 1

$$E=7 \cdot 10^7 \text{ kN/m}^2, \nu=0.30.$$

For displacements the following normalization was applied:

$$\bar{w} = \omega_0 \left(\frac{a}{2}, \frac{b}{2} \right) \left(\frac{Eh^3}{a^4 q_0} \right) \quad (2.33)$$

where a and b are the plate dimensions; h is the laminate thickness and q_0 is the value of the applied load.

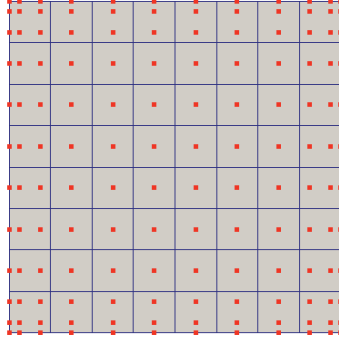


Figure 2.7: IGA Plate model. Element mesh and control points.

Static analysis under a uniform load

The defined simply supported plate with *Material 1* was subjected to a uniform load. Results are presented in Tables 2.2-2.4 for standard NURBS [24] and for the shell with the discrete vector theory for quadratic, cubic and quartic NURBS. The analytical thin solution value is 4.0624 [29]. As it can be seen, the effects of locking increase as the NURBS order diminishes for the standard NURBS. However the hierarchic vector theory is free of locking.

a/h	IGA FSDT	IGA TSDT	Hier FSDT	Hier TSDT	Thin IGA
5	4.9043	4.9026	4.9043	4.903	4.0624
10	4.2729	4.2728	4.2729	4.2728	
10 ²	4.0644	4.0644	4.0645	4.0645	
10 ³	4.0673	4.0655	4.0624	4.0624	
10 ⁴	4.0965	4.0956	4.0624	4.0624	
10 ⁵	4.0983	4.0983	4.0624	4.0624	

Table 2.2: Standard IGA vs. hierarchic approximation for quartic NURBS and analytical results for an isotropic square plate for CLT, FSDT and TSDT subjected to a uniform load.

a/h	IGA FSDT	IGA TSDT	Hier FSDT	Hier TSDT	Thin IGA
5	4.9044	4.9028	4.9042	4.9026	4.0625
10	4.2729	4.2728	4.273	4.2729	
10 ²	4.0665	4.0656	4.0646	4.0646	
10 ³	4.01	4.038	4.0625	4.0625	
10 ⁴	3.5773	3.591	4.0625	4.0625	
10 ⁵	3.5514	3.5516	4.0625	4.0625	

Table 2.3: Standard IGA vs. hierarchic approximation for cubic NURBS and analytical results for an isotropic square plate for CLT, FSDT and TSDT subjected to a uniform load.

Figure 2.8 represents the error of the central normalized displacement for a fixed mesh of 8 x 8 elements. It can be appreciated how these values are not sensitive to the slenderness and therefore how the hierarchic difference vector strategy is free of locking. It can also be appreciated that higher order NURBS converge to the analytical solution for the selected mesh, whereas the second order NURBS has not reach the final value.

a/h	IGA FSDT	IGA TSDT	Hier FSDT	Hier TSDT	Thin IGA
5	4.904	4.9017	4.8936	4.8919	
10	4.2713	4.2708	4.2576	4.2575	
10^2	3.9259	3.9688	4.0455	4.0455	
10^3	3.563	3.5692	4.0433	4.0433	4.0433
10^4	3.5513	3.5513	4.0433	4.0433	
10^5	3.5511	3.5511	4.0433	4.0433	

Table 2.4: Standard IGA vs. hierarchic approximation for quadratic NURBS and analytical results for an isotropic square plate for CLT, FSDT and TSDT subjected to a uniform load.

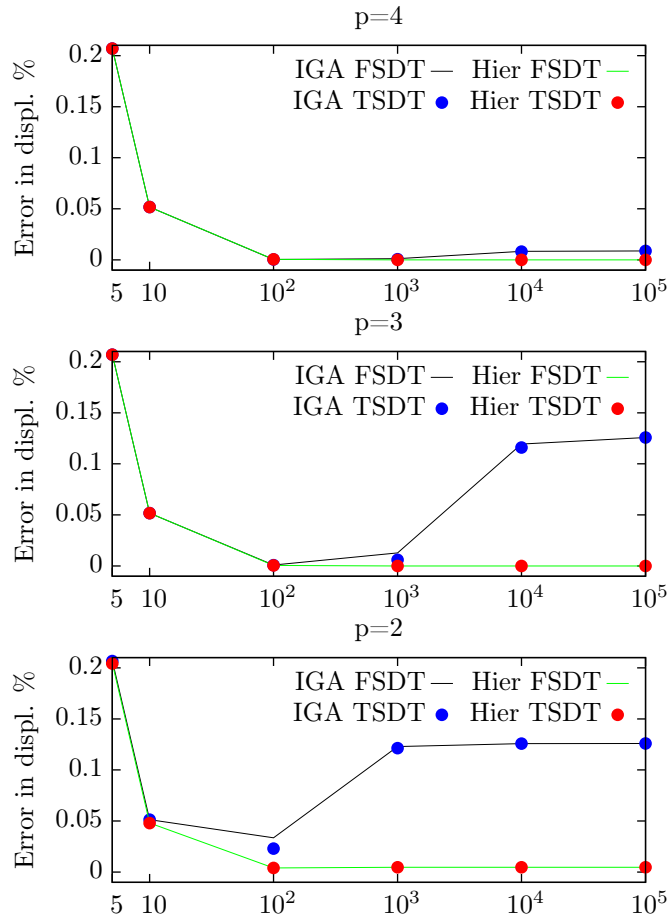


Figure 2.8: IGA vs. hierarchic (*) vector displacements error for quadratic, cubic and quartic NURBS for the simply supported plate.

Eigenmode analysis

In this case normalized frequencies are presented for the same isotropic plate for several slenderness. Here fourth-order NURBS were used and a 16x16 mesh. The first 256 modes are presented for the FSDT and TSDT solutions. Both of them were studied with standard NURBS and with the hierarchic vector theory. Figure 2.9 presents the relationship between the shear deformation theories and the CLT. Although higher order NURBS are used, locking effects increase as frequency does for the standard NURBS. The hierarchic vector theory is not sensitive to locking effects.

Frequencies were normalized by the following expression:

$$\bar{\omega} = \omega_i(a^2/h)\sqrt{\rho/E_2} \quad (2.34)$$

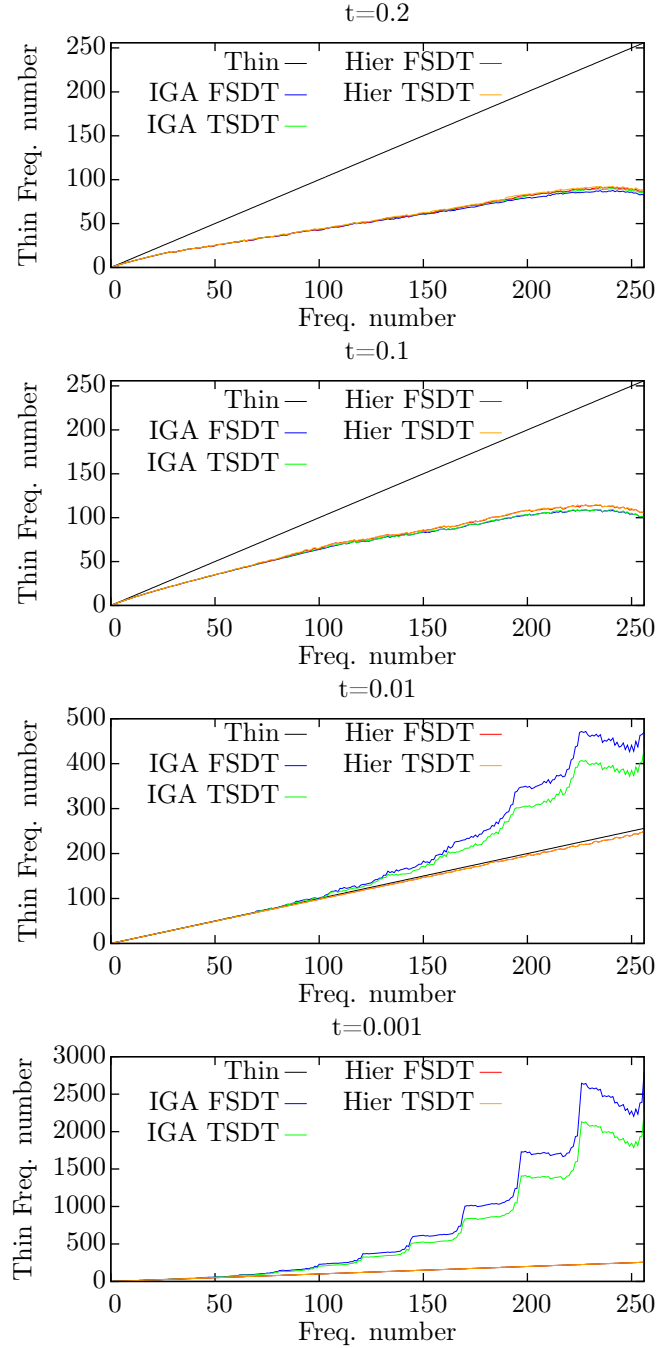


Figure 2.9: IGA vs. hierarchic vector normalized frequencies for $h=0.2$ m, $h=0.1$ m, $h=0.01$ m and $h=0.001$ m for the simply supported plate.

Mode	IGA FSDT	Hier FSDT	IGA TSDT	Hier TSDT	TSDT [30]	Thin IGA	Thin [30]
1	19.065	19.065	19.1	19.065	19.065	19.739	19.739
2	45.483	45.483	45.487	45.487	45.487	49.348	49.348
3	69.794	69.794	69.809	69.809	69.809	78.957	78.957
4	85.038	85.038	85.065	85.065	85.065	98.696	98.696
5	106.684	106.684	106.735	106.735	106.74	128.305	128.31
6	133.621	133.622	133.72	133.721	133.72	167.784	167.78
7	140.057	140.057	140.17	140.17	140.17	177.653	177.65
8	152.609	152.609	152.753	152.754	152.75	197.393	197.39
9	182.324	182.324	182.565	182.566	182.57	246.741	246.74
10	188.012	188.018	188.275	188.282	188.28	256.615	256.61
11	204.62	204.626	204.956	204.962	204.96	286.223	286.22
12	220.6	220.601	221.017	221.018	221.02	315.828	315.83
13	230.936	230.942	231.412	231.417	231.41	335.571	335.57

Table 2.5: Normalized frequency for isotropic plate of thickness $h=0.1m$ for CLT, FSDT and TSDT.

Figure 2.9 shows that for small thicknesses and higher frequencies, the hierarchic vector formulation tends to the thin solution. The standard IGA becomes inaccurate for small thicknesses and requires a mesh refinement to be more accurate.

A closer look to the same plate for a thickness $h=0.1 m$ is presented in Table 2.5 for the first 13 modes, in order to observe the differences between the frequencies for a moderate thick plate.

Static analysis of a skew plate under a uniform load

In this case a clamped skewed plate is studied for a slenderness of value 1000 ($L/t=1000$), for the FSDT and TSDT and two skew angles. As the slenderness is relative high, both theories FSDT and TSDT give the same results. Therefore, normalized central displacements are compared for quadratic, cubic and quartic NURBS. Several meshes with the hierarchic vector theory for the TSDT are presented in Table 2.6. Results converge to the thin case values [31], as expected with the selected thickness. Figure 2.10 presents the model of a 8×8 element mesh and 45° skew angle.

θ	4x4			8x8			16x16			Thin Anal.[31]
	p=2	p=3	p=4	p=2	p=3	p=4	p=2	p=3	p=4	
60°	0.5271	0.7614	0.7714	0.7066	0.7682	0.769	0.7534	0.769	0.769	0.769
45°	0.2199	0.3522	0.3715	0.3266	0.3748	0.377	0.3631	0.377	0.377	0.377

Table 2.6: Normalized displacements for a clamped isotropic skew plate with a TSDT under a uniform load.

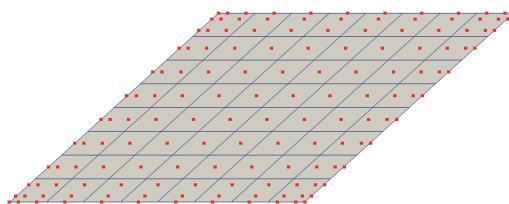


Figure 2.10: Skew plate model. Element mesh and control points.

Besides the shear-locking, the curvature of the shell introduces numerical locking, due to the effect of the coupling between the bending and membrane deformation. In the following examples this phenomenon will be illustrated.

2.4.2 Cantilever plate

A clamped isotropic circular plate of radius $R=1$ m and width $b=0.2$ m was studied. The IGA model can be seen in Fig. 2.11, jointly with the deformed configuration. A 1×16 mesh was used. The plate was subjected to an uniform line load in the free edge. The material assumed properties are:

Material 2

$$E=7 \cdot 10^7 \text{ kN/m}^2, \nu=0.$$

Tables 2.7-2.9 show the displacement u_s in the length direction. Results for standard IGA, for the discrete difference vector and for the projection method are presented. The solution is asymptotically convergent to the thin case, which normalized value is 6.1062. Since it is a bending dominated problem, the load is normalized with t^3 in order to have always the same result. It can be seen how the projection technique is free of locking, being the results independent from the slenderness. The standard IGA formulation is the worst of them since it has two kinds of lockings. Figure 2.12 shows the mentioned results for all the computed slenderness. In this case, for the sake of simplicity, only for the FSDT and TSDT and for cubic and quartic NURBS.

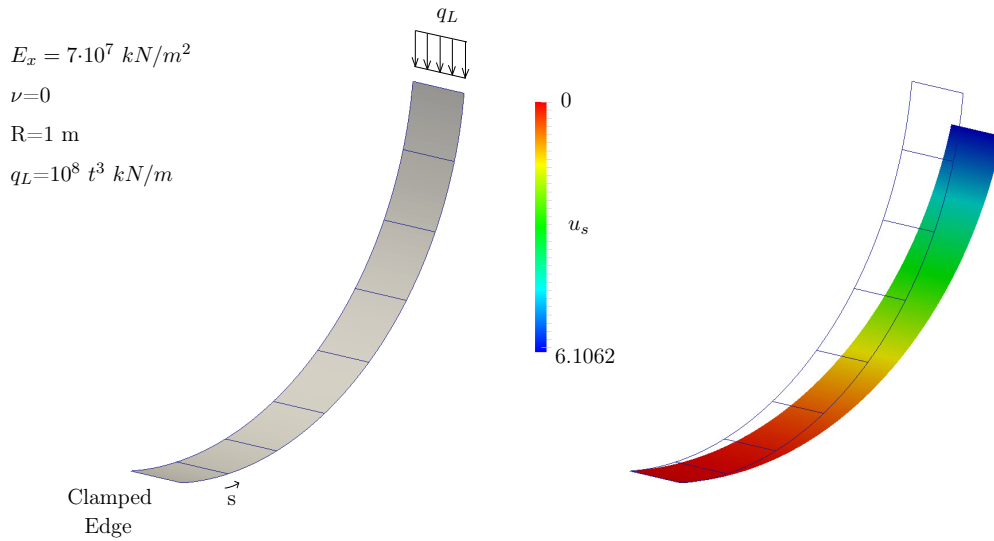


Figure 2.11: Cantilever plate mesh (8 elements) and deformed configuration.

a/h	IGA FSDT	IGA TSDT	Hier FSDT	Hier TSDT	FSDT*	TSDT*
5	6.2588	6.2562	6.2564	6.2561	6.2564	6.2561
10	6.1443	6.1438	6.1438	6.1438	6.1438	6.1438
10^2	6.1066	6.1066	6.1066	6.1066	6.1066	6.1066
10^3	6.105	6.1051	6.1055	6.1055	6.1062	6.1062
10^4	6.0755	6.076	6.0804	6.0804	6.1062	6.1062
10^5	5.1558	5.2484	6.0423	6.0423	6.1062	6.1062

Table 2.7: Standard IGA vs. hierarchic vs. hierarchic (*) approximation for quartic NURBS and analytical results for a cantilever plate for FSDT and TSDT subjected to a vertical load.

a/h	IGA FSDT	IGA TSDT	Hier FSDT	Hier TSDT	FSDT*	TSDT*
5	6.2588	6.2551	6.2551	6.255	6.2551	6.255
10	6.1443	6.1435	6.1436	6.1436	6.1436	6.1436
10 ²	6.1027	6.1033	6.1042	6.1042	6.1065	6.1065
10 ³	5.8565	5.8674	5.9026	5.9026	6.1062	6.1062
10 ⁴	3.1346	3.2269	3.8916	3.8916	6.1062	6.1062
10 ⁵	0.1431	0.1662	3.0662	3.0662	6.1062	6.1062

Table 2.8: Standard IGA vs. hierarchic vs. hierarchic (*) approximation for cubic NURBS and analytical results for a cantilever plate for FSDT and TSDT subjected to a vertical load.

a/h	CLT IGA (p=3)	CLT* (p=3)	CLT IGA (p=4)	CLT* (p=4)
5	6.1511	6.1511	6.151	6.151
10	6.1174	6.1174	6.1174	6.1174
10 ²	6.1063	6.1063	6.1039	6.1063
10 ³	6.1055	6.1062	5.9026	6.1062
10 ⁴	6.0804	6.1062	3.8916	6.1062
10 ⁵	6.0416	6.1062	3.0664	6.1062

Table 2.9: Standard IGA vs. hierarchic (*) approximation for cubic and quartic NURBS and analytical results for a cantilever plate for CLT subjected to a vertical load.

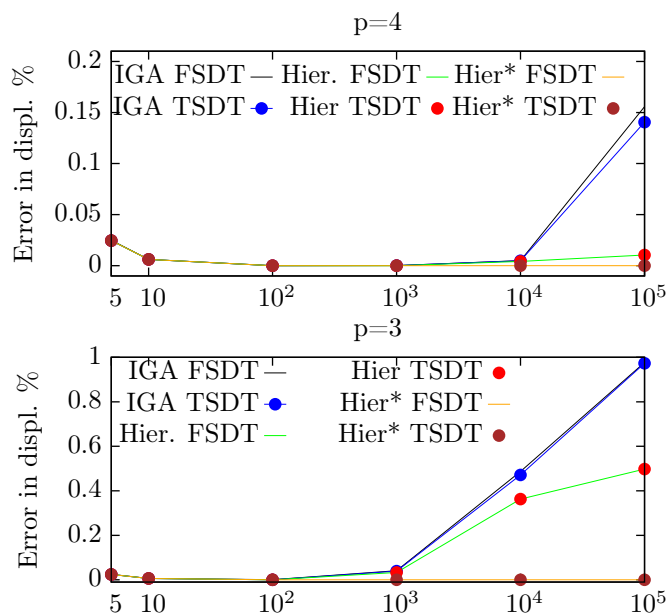


Figure 2.12: IGA vs. hierarchic vs. hierarchic (*) vector displacements error for quadratic and cubic NURBS for the cantilever plate for the FSDT and TSDT.

2.4.3 Scoderlis Lo-roof

Another problem to illustrate the advantage of the locking-free techniques is the well known Scoderlis problem. In this case it would be computed for a TSDT. The selected slenderness is in this case $R/t=1000$, which should give a solution similar to the CLT.

The cylinder of radius R and edge length L is fixed in the curved edges ($u_x = w_z = 0$). It is assumed that $R = 25$ m, $L = 50$ m, $h = 0.025$ m, $2\alpha = 80^\circ$, which is the total angle that defines the circular edges ($a = 2\alpha R$) and a dead load of $q_z = 0.90$ kN/m². The assumed material has the following properties:

Material 3
 $E=4.32 \cdot 10^8$ kN/m², $\nu=0$

Figure 2.13 defines this problem and also shows the vertical displacements under the dead load. The numerical convergence value obtained for this problem is 0.3204, which is the same with all the different approximations. In Figure 2.14 the maximum vertical displacement for several meshes at the center of the free edge is plotted for the standard IGA, the hierarchic approximation and the hierarchic (*). It can be seen how the presented formulation has better convergence. For small meshes, the accuracy is much better. The standard IGA is the worst strategy, as expected, whereas the hierarchic lies between them. Results are presented in Table 2.10.

Elements/side	IGA(p=3)	IGA(p=4)	Hier (p=3)	Hier (p=4)	Hier* (p=3)	Hier* (p=4)
2	0.0673	0.1427	0.07525	0.1428	0.1063	0.1568
4	0.13497	0.1925	0.14254	0.1953	0.2893	0.3294
8	0.2038	0.2952	0.2558	0.3142	0.3199	0.3205
16	0.3074	0.3201	0.3192	0.3204	0.3204	0.3204
32	0.3202	0.3204	0.3204	0.3204	0.3204	0.3204

Table 2.10: Scoderlis problem. Maximum vertical displacement w_z for standard IGA vs. hierarchic vs. hierarchic (*) approximation for cubic and quartic NURBS.

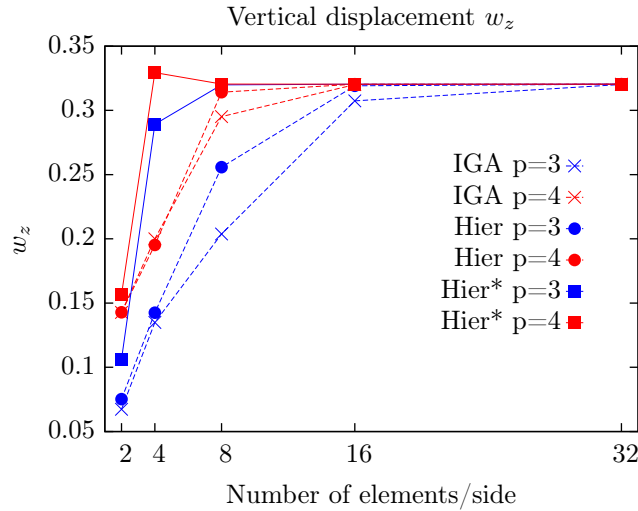


Figure 2.13: Maximum vertical displacement for the standard IGA, hierarchic vector and hierarchic (*) for cubic and quartic NURBS.

2.5 Conclusions

In this contribution, a shell has been implemented with an IGA NURBS-based formulation with a locking strategy. Shear-locking is avoided with the use of a discrete difference vector theory, whereas curvature-locking is avoided with a projection technique. Several problems have been analyzed in order to proof the advantages of the locking-free formulation for a TSDT, as well the typical FSDT and CLT. In further works this chapter will be a paper in which some additional composite results, similar to the ones presented in Chapter 1, will be presented. The main objective was to illustrate how the selected strategy avoid the locking phenomenon which is usually done with isotropic examples.

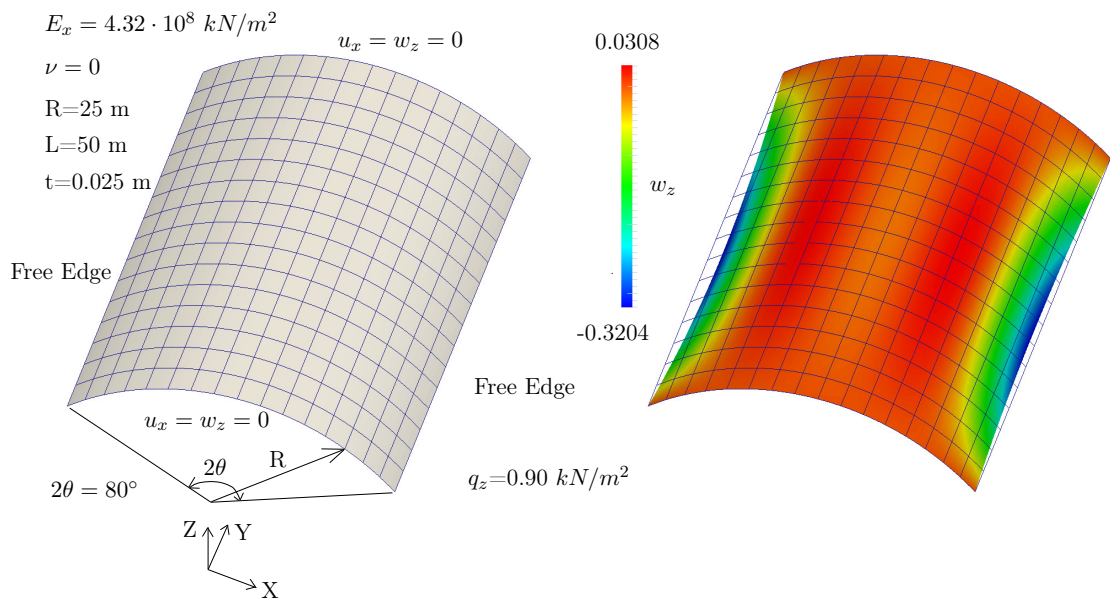


Figure 2.14: Scoderlis model and deformed configuration.

Chapter 3

On the Accuracy of a 4-Node Delaminated Composite Plate Element and its Application to Damage Detection

In this chapter the following paper is presented: "On the Accuracy of a 4-Node Delaminated Composite Plate Element and its Application to Damage Detection" published in the Journal of Vibration and Acoustics. Transactions of ASME. in 2013, with doi: 10.1115/1.4023994. The chapter develops a 4-node delaminated finite element composite plate and presents some results in the field of SHM, to quantify the effect of delamination in composite plates.

Abstract

This paper presents a new 4-node composite element, which incorporates n_d delaminations through its thickness. Based on the Extended Finite Element Method (X-FEM) technology, the element is particularized on a CLT (Classical Laminate Theory). Delamination is considered in the kinematic equations with additional degrees of freedom. The result is a 4-node quadrilateral element requiring only two single FEM (Finite Element Method) formulations, a bending one and a membrane one. An important result is that this formulation has the same accuracy as when separate elements are considered ("4 Region Approach"). It is furthermore proven that the delaminated element passes the "Patch Test" if the selected FEM formulations to build the element pass the test in the pure single problems, making this methodology very attractive to develop other fractured elements. To illustrate this result, two *Benchmark* problems were studied: firstly a complete delaminated cantilever plate, and secondly a complete delaminated circular plate. The element was tested in the context of SHM (Structural Health Monitoring). Frequency shifts, damage indexes and changes in mode shapes and Frequency Response Functions (FRF) were obtained to quantify the severity of damage due to delamination.

3.1 Introduction

The use of advanced composite materials has grown in recent decades. From the structural point of view, their stiffness, weight, fatigue-life and strength limit make this kind of material very attractive.

It is well known that the delamination or debonding of adjoining plies is one of the most frequent types of damage in composite structures. This modifies the carrying capacity of the structure and can lead to catastrophic consequences if they are large enough. Therefore, delamination must be taken into account in the process of designing such structures.

In the context of SHM, model based methods are one of the recent damage detection research lines that has been successfully applied. They combine a response measured on a structure with a numerical model, in order to detect damage, which is usually subdivided into four levels of damage [32] (detection, localization, severity and remaining life). In this case, the physical properties, obtained from measurements, are the dynamic ones. Several damage identification methods based on the change of eigenfrequencies, mode shapes, damping ratios, FRF, etc., have been used to quantify damage in combination with a damage detection technique (Artificial Neuronal Networks or ANN, model updating strategies, Genetic Algorithms, etc). This implies the minimization of a cost function based on these damage indicators to finally arrive at the first three levels of damage [32]. Improvements in terms of location (levels II and III) can be performed by the use of modal shapes, the curvature shapes being more powerful than displacement ones. All the identification techniques involve a compromise between the severity of damage and the number of modes required to be able to detect damage. Interested readers can find detailed information in [33, 34, 35, 36, 37].

Fritzen and Bohle in [38, 39] investigated the capabilities of model based methods in civil engineering structures with model update strategies, performed minimizing a cost function in terms of frequencies and mode shapes extracted from FRF, obtained with piezoelectric (PZT) accelerometers. Similar work in frame structures was presented by Yu and Lin in [40] and by Liu et al. in [41]. Jenq and Lee [42] utilized a back-propagation neural network with an adaptive learning rate, using frequency changes as inputs, to predict hole defect sizes and locations in Glass Fiber Reinforced Plastic (GFRP) composite laminated beams. Feng and Bahng [43] proposed a new method for the monitoring of jacketed columns that employs the combination of vibration testing, neural network, and finite element techniques. Frequencies and mode shapes were used as inputs.

More specifically, Zak et al. [44, 45] studied the vibration of delaminated composite beams and plates. Changes in eigenfrequencies were validated in a finite element model and experimental data. Using three-layer feed-forward neural networks, Hanagud and Luo [46] studied a composite plate based on measured structural dynamic response. Analytical models were constructed to predict the dynamic response of the damaged structure, based on the computation of damage indexes, obtained from the mode shapes. They were used as inputs and damage parameters (location and extent) as outputs. The influence in frequency shifts and FRF due to debonding on sandwich panels was studied by Kim and Hwang in [47] with good agreement with numerical results. Krawczuk et al. [48] applied a genetic algorithm to identify and locate damage in a laminated composite beam using frequency shifts as inputs. The model was validated with numerical tests. Ling et al. in [49] used fiber-optic sensors to measure FRF, which is used to detect and identify the size and location of delaminations in composite beams. Results are also validated with a numerical model. Wei et al. in [50] studied damage detection with model-based neural networks and vibration response measurement. Damage-induced energy in terms of the FRF of the signals was used as input to locate delamination and extent. Sanders et al. in [51, 52] discussed the subject of detecting delamination within composites with neural networks. Fiber-optic sensors were used to measure the first five modal frequencies of several glass/epoxy composite beams. Harrison and Butler used a genetic algorithm to locate delamination on beams in [53] using frequency shifts and mode shapes. Recently, Figueiredo et al. have used piezoelectric sensors for damage detection in composite plates using time-series analysis in [54]. Results are also compared to those provided from FRF analysis. Zwink have located damage in composite specimens due to impact loads with vibration-based techniques considering the non-linear

response in [55]. Finally, Saravanos and Hopkins studied in [56] the change of damping ratios in cantilever composite beams and compared the results with numerical simulations.

On the other hand, developing a delaminated composite implies two models, the first being a composite theory and the second a fracture model. The main composite theories are based on the so-called Equivalent Single Layer Theory (ESL), resulting in the Classical Laminate Theory (CLT) for thin plates, the First Order Shear Deformation Theory (FSDT) for thick plates, and the Higher Order Theories (HOT) as a generalized ESL theory. Focusing on the layer level, in order to study interply stresses, Layerwise theories were introduced by Reddy in [3].

A review of the models developed for delaminations was offered initially by Zhou et al. in [33] and more recently by Delia and Shu in [57]. Fracture models mostly consider delamination using the so-called “4 Region Approach” (see Refs. [33, 57]). This assumption physically separates the model into four different elements that are properly connected at the nodes. Figure 3.1 shows a delaminated composite and the model of the “4 Region Approach”. In the context of SHM, this is the most commonly applied technique. This technique has also been applied by Damghani et al. in [58] to study the buckling of plates, and by Azam in [59] to study the buckling of shells.

An alternative and less common way to model delaminations is considering them in the equations of the problem. Thus, when new kinematic equations are properly defined, the delamination can be taken into account. This methodology affords the advantage of not requiring remeshing. As in the X-FEM technology, introduced by Babuska and Melenk in [60, 61], the discontinuity generated by the delamination can be included through new degrees of freedom that represent the relative movements in the discontinuity. This concept was firstly applied in the context of SHM with successful results by Saravanos and Hopkins in [56] to study the effect of delaminations on damping ratios in cantilever beams, and by Chattopadhyay et al. in [62, 63] and Swann et al. in [64] with delaminated composite plates, comparing the numerical model and the experimental data.

In the present paper, we are mostly interested in comparing the two delamination modeling methodologies and showing that numerically they provide the same results. The present methodology is signaled as a better way to model delaminations for further applications, involving advantages in terms of design, such as no need for remeshing, and allowing for multiple delaminations. Furthermore, the effect of delamination on some of the reviewed damage indicators is determined, presenting the new element as a tool for damage detection techniques.

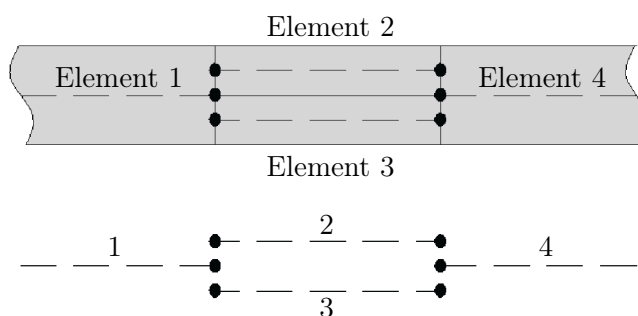


Figure 3.1: 4 Regions Approach

3.2 Delamination model

3.2.1 Kinematic equations of a delamination

In this paper, the delaminated element developed is based on a CLT theory whose kinematic equations are given by:

$$\begin{aligned}
 u(x, y, z) &= u_0(x, y) + \theta_{y0}(x, y)z + \sum_{r=1}^{n_d} \left[u_r(x, y) + \theta_{yr}(x, y)z \right] H(z - z_r) \\
 v(x, y, z) &= v_0(x, y) + \theta_{x0}(x, y)z + \sum_{r=1}^{n_d} \left[v_r(x, y) + \theta_{xr}(x, y)z \right] H(z - z_r) \\
 w(x, y, z) &= w_0(x, y) + \sum_{r=1}^{n_d} \left[w_r(x, y) H(z - z_r) \right]
 \end{aligned} \tag{3.1}$$

where u , v , and w are displacements; θ_x and θ_y are rotations; H is the Heaviside step function; the subscript 0 indicates mid-plane quantities and n_d is the number of delaminations considered. Variables with subscript r are the new degrees of freedom describing the kinematic discontinuities across the r -th delamination. These new variables represent relative displacements and rotations between plies.

The CLT of an undelaminated plate relates internal forces/moments, \mathbf{N}_0 and \mathbf{M}_0 , with in-plane strains, $\boldsymbol{\epsilon}_0$ and $\boldsymbol{\kappa}_0$, i.e.,

$$\begin{Bmatrix} \mathbf{N}_0 \\ \mathbf{M}_0 \end{Bmatrix} = \begin{bmatrix} \mathbf{A} & \mathbf{B} \\ \mathbf{B} & \mathbf{D} \end{bmatrix} \begin{Bmatrix} \boldsymbol{\epsilon}_0 \\ \boldsymbol{\kappa}_0 \end{Bmatrix} \tag{3.2}$$

where \mathbf{A} is the membrane stiffness matrix, \mathbf{D} the bending stiffness matrix and \mathbf{B} the coupling matrix, all of them referred to the laminate mid-plane and \mathbf{N}_0 , \mathbf{M}_0 are the resultant internal forces and moments of the laminate section.

Using the kinematic equations (5.1), an analogue to Eq. (5.2) can be obtained for a laminate with n_d delaminations:

$$\begin{Bmatrix} \mathbf{N}_0 \\ \mathbf{N}_1 \\ \vdots \\ \mathbf{N}_{n_d} \\ \mathbf{M}_0 \\ \mathbf{M}_1 \\ \vdots \\ \mathbf{M}_{n_d} \end{Bmatrix} = \begin{bmatrix} \mathbf{A} & \mathbf{A}_1 & \dots & \mathbf{A}_{n_d} & \mathbf{B} & \mathbf{B}_1 & \dots & \mathbf{B}_{n_d} \\ \mathbf{A}_1 & \mathbf{A}_{11} & \dots & \mathbf{A}_{1n_d} & \mathbf{B}_1 & \mathbf{B}_{11} & \dots & \mathbf{B}_{1n_d} \\ \vdots & \vdots & \dots & \vdots & \vdots & \vdots & \dots & \vdots \\ \mathbf{A}_{n_d} & \mathbf{A}_{1n_d} & \dots & \mathbf{A}_{n_d} & \mathbf{B}_{n_d} & \mathbf{B}_{1n_d} & \dots & \mathbf{B}_{n_d} \\ \mathbf{B} & \mathbf{B}_1 & \dots & \mathbf{B}_{n_d} & \mathbf{D} & \mathbf{D}_1 & \dots & \mathbf{D}_{n_d} \\ \mathbf{B}_1 & \mathbf{B}_{11} & \dots & \mathbf{B}_{1n_d} & \mathbf{D}_1 & \mathbf{D}_{11} & \dots & \mathbf{D}_{1n_d} \\ \vdots & \vdots & \dots & \vdots & \vdots & \vdots & \dots & \vdots \\ \mathbf{B}_{n_d} & \mathbf{B}_{1n_d} & \dots & \mathbf{B}_{n_d} & \mathbf{D}_{n_d} & \mathbf{D}_{1n_d} & \dots & \mathbf{D}_{n_d} \end{bmatrix} \begin{Bmatrix} \boldsymbol{\epsilon}_0 \\ \boldsymbol{\epsilon}_1 \\ \vdots \\ \boldsymbol{\epsilon}_{n_d} \\ \boldsymbol{\kappa}_0 \\ \boldsymbol{\kappa}_1 \\ \vdots \\ \boldsymbol{\kappa}_{n_d} \end{Bmatrix} \tag{3.3}$$

where $\mathbf{A}_{rr} = \mathbf{A}_r$, $\mathbf{B}_{rr} = \mathbf{B}_r$ for $r = 1, 2, \dots, n_d$ are the constitutive matrices of the r -th delamination and \mathbf{N}_r , \mathbf{M}_r are the internal forces and moments of the partial section (above the r -th ply).

3.2.2 FEM formulation

Using the weak form of the elastic problem, the Stiffness and Mass matrices can be obtained, i.e.,

$$\int_{\Omega_V} [\rho \omega_i \ddot{u}_i + \omega_{i,j} \sigma_{ij}] d\Omega_V = \int_{\Omega} \omega_i f_i d\Omega + \int_{\Gamma_q} \omega_i \bar{t}_i d\Gamma \quad (3.4)$$

where Ω_V is the volume of the body; Γ is the body surface and Γ_q the surface with load prescriptions; f_i are the body loads and \bar{t}_i are surface loads; ω_i are the variations; ρ is the density; u_i are the displacements and \ddot{u}_i are the accelerations and finally σ_{ij} are stresses. From Eq. (3.4), the Stiffness Matrix is obtained as:

$$\begin{aligned} \mathbf{K} = & \int_{\Omega} [\mathbf{B}_M^T \mathbf{A} \mathbf{B}_M + \mathbf{B}_M^T \mathbf{B} \mathbf{B}_B + \mathbf{B}_B^T \mathbf{B} \mathbf{B}_M + \mathbf{B}_B^T \mathbf{D} \mathbf{B}_B] d\Omega + \\ & \sum_{r=1}^{n_d} \int_{\Omega} [\mathbf{B}_M^T \mathbf{A}_r \mathbf{B}_{rM} + \mathbf{B}_{rM}^T \mathbf{A}_r \mathbf{B}_{rM} + \mathbf{B}_M^T \mathbf{B}_r \mathbf{B}_{rB} + \mathbf{B}_{rM}^T \mathbf{B}_r \mathbf{B}_B + \\ & \mathbf{B}_B^T \mathbf{B}_r \mathbf{B}_{rM} + \mathbf{B}_{rB}^T \mathbf{B}_r \mathbf{B}_M + \mathbf{B}_B^T \mathbf{D}_r \mathbf{B}_{rB} + \mathbf{B}_{rB}^T \mathbf{D}_r \mathbf{B}_B] d\Omega + \\ & \sum_{r=1}^{n_d} \sum_{s=1}^{n_d} \int_{\Omega} [\mathbf{B}_{rM}^T \mathbf{A}_{rs} \mathbf{B}_{sM} + \mathbf{B}_{rM}^T \mathbf{B}_{rs} \mathbf{B}_{sB} + \\ & \mathbf{B}_{rB}^T \mathbf{B}_{rs} \mathbf{B}_{sM} + \mathbf{B}_{rB}^T \mathbf{D}_{rs} \mathbf{B}_{sB}] d\Omega \end{aligned} \quad (3.5)$$

where Ω is the mid-plane of the plate; $\mathbf{B}_M, \mathbf{B}_B$ are the deformation matrices of the membrane (u_0, v_0) and bending ($w_0, \theta_{x0}, \theta_{y0}$) problem and $\mathbf{B}_{rM}, \mathbf{B}_{rB}$ are the deformation matrices of the membrane (u_r, v_r) and bending ($w_r, \theta_{xr}, \theta_{yr}$) problem. Analogously, the Mass Matrix is obtained as:

$$\mathbf{M} = \int_{-t/2}^{t/2} [m_1 + m_2 + m_3 + m_4] dz \quad (3.6)$$

$$m_1 = \int_{\Omega} \rho [\mathbf{N}_u^T \mathbf{N}_u + \mathbf{N}_v^T \mathbf{N}_v + \mathbf{N}_w^T \mathbf{N}_w + z^2 (\mathbf{N}_{\theta_x}^T \mathbf{N}_{\theta_x} + \mathbf{N}_{\theta_y}^T \mathbf{N}_{\theta_y})] d\Omega$$

$$\begin{aligned} m_2 = & \sum_{r=1}^{n_d} \int_{\Omega} \rho [\mathbf{N}_u^T \mathbf{N}_{ur} + \mathbf{N}_{ur}^T \mathbf{N}_u + z (\mathbf{N}_u^T \mathbf{N}_{\theta_{yr}} + \mathbf{N}_{ur}^T \mathbf{N}_{\theta_y} + \mathbf{N}_{\theta_{yr}}^T \mathbf{N}_u + \mathbf{N}_{\theta_y}^T \mathbf{N}_{ur}) + \\ & z^2 (\mathbf{N}_{\theta_y}^T \mathbf{N}_{\theta_{yr}} + \mathbf{N}_{\theta_{yr}}^T \mathbf{N}_{\theta_y})] H(z - z_r) d\Omega + \\ & \sum_{r=1}^{n_d} \sum_{s=1}^{n_d} \int_{\Omega} \rho [\mathbf{N}_{ur}^T \mathbf{N}_{us} + z (\mathbf{N}_{ur}^T \mathbf{N}_{\theta_{ys}} + \mathbf{N}_{\theta_{yr}}^T \mathbf{N}_{us}) + \\ & z^2 \mathbf{N}_{\theta_{yr}}^T \mathbf{N}_{\theta_{ys}}] H(z - z_r) H(z - z_s) d\Omega \end{aligned}$$

$$\begin{aligned} m_3 = & \sum_{r=1}^{n_d} \int_{\Omega} \rho [\mathbf{N}_v^T \mathbf{N}_{vr} + \mathbf{N}_{vr}^T \mathbf{N}_v + z (\mathbf{N}_v^T \mathbf{N}_{\theta_{xr}} + \mathbf{N}_{vr}^T \mathbf{N}_{\theta_x} + \mathbf{N}_{\theta_{xr}}^T \mathbf{N}_v + \mathbf{N}_{\theta_x}^T \mathbf{N}_{vr}) + \\ & z^2 (\mathbf{N}_{\theta_x}^T \mathbf{N}_{\theta_{xr}} + \mathbf{N}_{\theta_{xr}}^T \mathbf{N}_{\theta_x})] H(z - z_r) d\Omega + \\ & \sum_{r=1}^{n_d} \sum_{s=1}^{n_d} \int_{\Omega} \rho [\mathbf{N}_{vr}^T \mathbf{N}_{vs} + z (\mathbf{N}_{vr}^T \mathbf{N}_{\theta_{xs}} + \mathbf{N}_{\theta_{xr}}^T \mathbf{N}_{vs}) + \\ & z^2 \mathbf{N}_{\theta_{xr}}^T \mathbf{N}_{\theta_{xs}}] H(z - z_r) H(z - z_s) d\Omega \end{aligned}$$

$$\begin{aligned}
 m_A = & \sum_{r=1}^{n_d} \int_{\Omega} \rho (\mathbf{N}_w^T \mathbf{N}_{wr} + \mathbf{N}_{wr}^T \mathbf{N}_w) H(z - z_r) d\Omega + \\
 & \sum_{r=1}^{n_d} \sum_{s=1}^{n_d} \int_{\Omega} \rho \mathbf{N}_{wr}^T \mathbf{N}_{ws} H(z - z_r) H(z - z_s) d\Omega
 \end{aligned} \tag{3.7}$$

where:

$$\begin{aligned}
 u_0(x, y) &= \mathbf{N}_u \mathbf{u}, & v_0(x, y) &= \mathbf{N}_v \mathbf{u}, & w_0(x, y) &= \mathbf{N}_w \mathbf{u} \\
 \theta_{x0}(x, y) &= \mathbf{N}_{\theta_x} \mathbf{u}, & \theta_{y0}(x, y) &= \mathbf{N}_{\theta_y} \mathbf{u} \\
 u_r(x, y) &= \mathbf{N}_{ur} \mathbf{u}, & v_r(x, y) &= \mathbf{N}_{vr} \mathbf{u}, & w_r(x, y) &= \mathbf{N}_{wr} \mathbf{u} \\
 \theta_{xr}(x, y) &= \mathbf{N}_{\theta_{xr}} \mathbf{u}, & \theta_{yr}(x, y) &= \mathbf{N}_{\theta_{yr}} \mathbf{u}
 \end{aligned} \tag{3.8}$$

With the formulation presented in Section 5.2.1, a finite element was developed. This element has $5 + 5 n_d$ degrees of freedom per node, due to the n_d delaminations in its thickness. The $5 n_d$ degrees of freedom represent the relative displacements in each delamination. The element requires two finite element formulations to develop the global behaviour. One is the membrane formulation, modeled with the QMITC element [65]. The other one is the bending formulation, modeled with the DKQ element [66]. This element was implemented in the Finite Element Analysis Program FEAP ([67]-[28]).

3.3 Element validation

One of the interesting results of this paper is that this methodology always leads to elements that pass the ‘‘Patch Test’’. Two *Benchmark* problems show, in this section, that the accuracy of this methodology is the same as that of the ‘‘4 Region Approach’’ (separate elements), underlining this alternative as a better way to model delamination.

3.3.1 Patch Test

The developed element passes the ‘‘Patch Test’’ if the single FEM formulations to build the element likewise pass the ‘‘Patch Test’’ in the pure single problems. No FEM tests are required and a brief demonstration is expounded here. Two steps are needed to prove this:

- Every composite passes the ‘‘Patch Test’’ if the uncoupled membrane and bending formulation pass the ‘‘Patch Test’’
- The delaminated element passes the ‘‘Patch Test’’ if the kinematic equations have the form described in this paper (see Eq. (5.1))

The first argument can be easily understood since the uncoupled trial solutions: $\mathbf{u}=\{u_0, v_0\}$ and $\mathbf{w}=\{w_0, \theta_{x0}, \theta_{y0}\} \in H^1$ Sobolev space¹. Then, the *Cauchy – Schwartz* inequality² ensures that the coupling term of the membrane-bending ‘‘Patch Test’’ problem has an exact solution, verifying the ‘‘Patch Test’’ for a composite element.³

¹The DKQ element is a C^0 element.

² $|\int_{\Omega} fg d\Omega| \leq \left(\int_{\Omega} f^2 d\Omega\right)^{1/2} \left(\int_{\Omega} g^2 d\Omega\right)^{1/2}$

³For C^1 bending elements, the trial solution $\mathbf{w}=\{w_0, \theta_{x0}, \theta_{y0}\} \in H^2$ Sobolev space; analogously it can be proven that the composite element also passes the ‘‘Patch Test’’.

Secondly, the kinematic equations described in this paper allow us to define the following trial solutions:

$$\begin{aligned} \mathbf{u} &= \{ \underbrace{u_0, v_0}_0, \underbrace{u_1, v_1}_1, \underbrace{u_2, v_2}_2, \dots, \underbrace{u_{n_d}, v_{n_d}}_{n_d} \} \\ \mathbf{w} &= \{ \underbrace{w_0, \theta_{x0}, \theta_{y0}}_0, \underbrace{w_1, \theta_{x1}, \theta_{y1}}_1, \underbrace{w_2, \theta_{x2}, \theta_{y2}}_2, \dots, \underbrace{w_{n_d}, \theta_{x_{n_d}}, \theta_{y_{n_d}}}_{n_d} \} \end{aligned} \quad (3.9)$$

This structure ensures that the new trial functions $\in H^1$. Then, it is trivial that all the new coupling terms have an exact solution for the ‘‘Patch Test’’ problem, as in the case of the undelaminated composite.

Finally, for higher order composite theories, it can be easily proven that this methodology leads to elements that always pass the ‘‘Patch Test’’ if the selected single elements to build the delaminated one also pass the ‘‘Patch Test’’.

3.3.2 Convergence and accuracy compared with separate elements. Benchmark problem 1

First of all, a complete delaminated cantilever plate with beam behaviour and dimensions 0.20 m x 0.02 m was studied. The mechanical properties of the ply were taken to be $E_x = 150$, $E_y = 11.5$, $G_{xy} = 5$ GPa, $\nu = 0$, $\rho = 1560$ kg/m³. The ply thickness was considered to be $t_p = 0.188$ mm. The composite is a 14 layer $[0, 90, 0, 90, 0, 90, 0]_S$, plotted in Fig. 3.2.

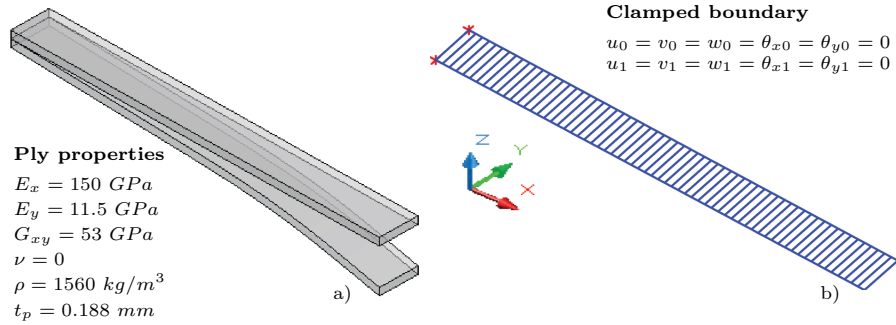


Figure 3.2: a) Delaminated cantilever beam. b) FEM model.

A uniform load was applied to the lower part of the plate, ensuring the opening of the delamination. Figure 4.2a shows the relative error of the L_2 -Norm for the delaminated element and the one obtained from a cantilever plate element of 7 layers $[0, 90, 0, 90, 0, 90, 0]$ that constitutes the lower part of the composite (separate elements). The separate part can be directly computed with the DKQ formulation. Both formulations have practically the same relative error of the L_2 -Norm for every mesh.

Figure 4.2b shows the relative error in the first four eigenfrequencies for both formulations. It can be seen that the results are practically equivalent for every mesh and that the error grows with the frequency, since the mesh loses accuracy when the modes increase.

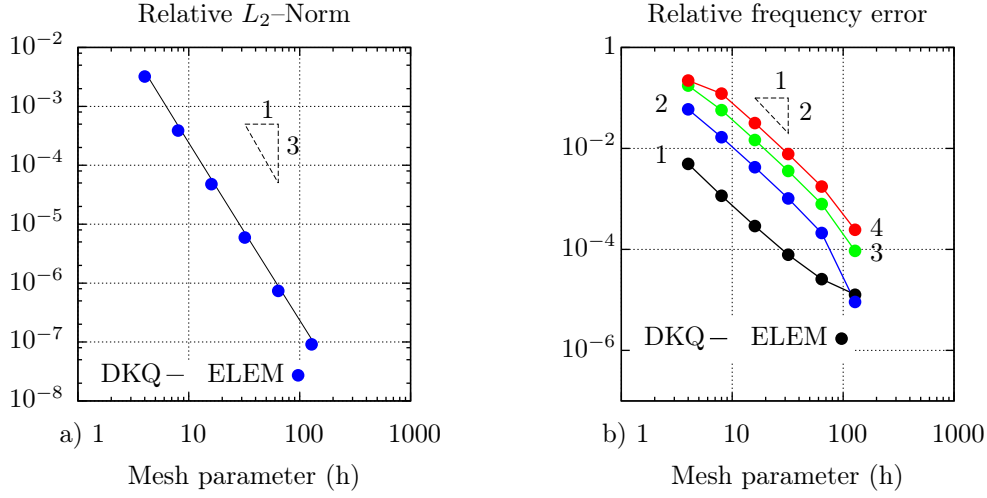


Figure 3.3: a) Relative error in L_2 -Norm for separate elements (DKQ) and delaminated element. b) Relative error in eigenfreq. (1-4). Lines (DKQ), dots (delaminated element).

3.3.3 Convergence and accuracy compared with separate elements. Benchmark problem 2

Secondly, a complete delaminated circular plate, clamped in all its boundaries and having a radius of 0.50 m, was studied. The mechanical properties of the ply were considered to be $E_x = 150$, $E_y = 150$, $G_{xy} = 53$ GPa, $\nu = 0.42$, $\rho = 1560$ kg/m³. The ply thickness was taken to be $t_p = 0.188$ mm. The composite is a 14 layer $[0, 90, 0, 90, 0, 90, 0]_S$, plotted in Fig. 3.4.

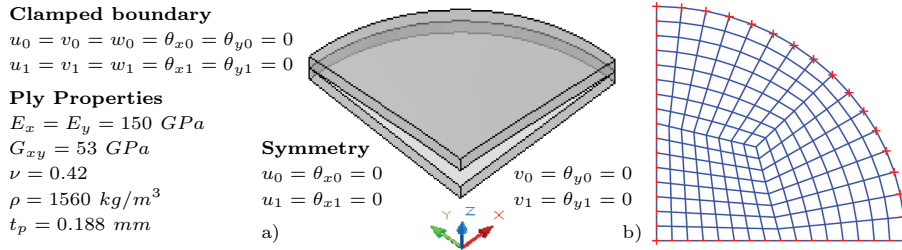


Figure 3.4: a) Delaminated circular clamped plate (quarter represented). b) FEM model.

A uniform load was applied to the upper part of the plate, ensuring, as in the previous case, the opening of the delamination. Figure 4.3a shows the relative error in L_2 -Norm of the delaminated element, and the one obtained from the upper part constituted by a 7 layer $[0, 90, 0, 90, 0, 90, 0]$. The separate part can be directly computed by means of the DKQ formulation. As in the previous case, both formulations have practically the same relative error of the L_2 -Norm for every mesh.

Analogously, Fig. 4.3b shows the relative error in the first three axisymmetrical eigenfrequencies for both formulations. It can be seen that the results are practically equivalent for every mesh and that the error grows along with the frequency, since the mesh loses accuracy when the modes increase.

From these results, it can be concluded that the accuracy of this methodology is the same as when separate elements are considered. This finding serves to confirm that the method is a very sound option. It is important to remark that the accuracy of the solution depends only on the selected

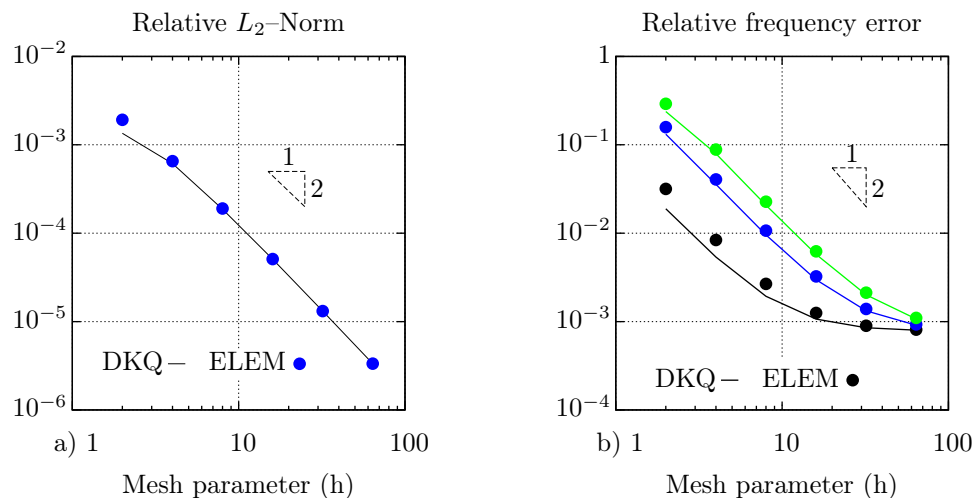


Figure 3.5: a) Relative error in L_2 -Norm for separate elements (DKQ) and delaminated element. b) Relative error in eigenfreq. (1-3). Lines (DKQ), dots (delaminated element).

membrane and bending formulations. In this case, DKQ and QMITC elements are used, respectively. If the formulations of the single elements are more accurate, the delaminated element will have the same accuracy. It is moreover important to mention that this element is conceived for plate vibrations, meaning that the study of accuracy was applied to bending problems.

3.4 Numerical examples for damage detection

Delamination detection is one of the main interests in the application of advanced composite materials in the aeronautical industry. Controlling the size of existing delaminations in order to decide when a structure must be repaired is a very important issue. The purpose of this section is to verify the developed delamination FEM model for future applications in damage detection. As mentioned in the Introduction, model based methods have been successfully applied in some previous works [44, 45, 46, 47, 48, 49, 50, 51, 52, 53, 54, 55, 56]. Two numerical examples are then studied with two different composite stacking sequences, in order to appreciate how the characteristic parameters of delamination (location, extension and position in the thickness) affect the response of the specimen in terms of the usually applied damage indicators: frequency shifts, damage indexes, mode shape changes and FRF variations.

3.4.1 Cantilever beam

First, a cantilever plate with beam behaviour is studied, analyzing two different stacking sequences to understand the effect of delamination. In this case, only one delamination in the thickness is considered ($n_d=1$). The beam has the same dimensions and ply properties as in Section 5.3. Table 3.1 shows different delamination extensions, placed always at the coordinate $x = 0.45 L$ (center of delamination). The stacking sequences used are $[0\ 90]_{3S}$ and $[0\ 90\ 45\ -45\ 0\ 90]_S$. Figure 3.6 shows the cantilever beam modeled with the new element proposed in this paper.

Frequency shifts and mode shapes are obtained to quantify the effect of the delamination on its dynamic response. From the damaged and undamaged response, a typical index of damage based on the response of the entire beam is defined as:

$$DI = \frac{|\Phi_0 - \Phi_1|}{|\Phi_0|} \quad (3.10)$$

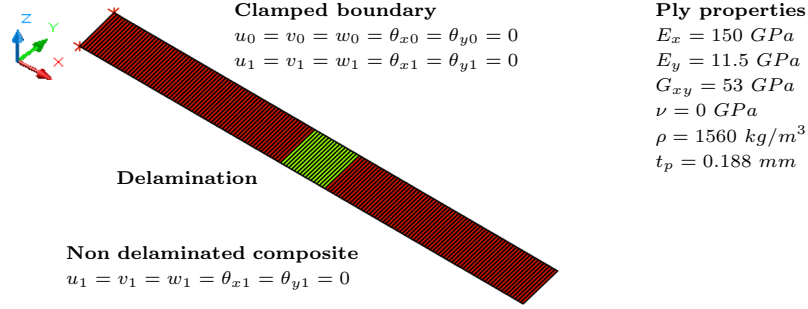


Figure 3.6: Delaminated FEM Model of a cantilever beam. Green elements represent the delamination.

where subindex 0 represents the undamaged beam and subindex 1 the delaminated one; Φ is considered to be a particular mode shape.

Extension	Length (cm)		Position in thickness
I	2.0	10%	between plies 3-4
II	2.0	10%	centered
III	1.0	5%	centered
IV	0.4	2%	centered

Table 3.1: Different delamination extensions and position in the thickness for the composite beam

Tables 3.2 and 3.3 respectively represent the frequency shifts and damage indexes (DI) for displacements and curvatures in both stacking sequences. Some already known results can be underlined here. They grow with the frequency, although not monotonically in the case of frequency shifts, requiring the use of higher modes for the detection of minor damage. From both tables, it follows that mode shapes/damage indexes have greater capability in damage detection than frequency shifts, damage indexes of curvatures being a better damage indicator (see e.g. [34, 35, 36]), as is well known.

Mode		Frequency shift (%)						
		I	II	III	I	II	III	
[0 90] _{3S}	5	1.78	3.31	0.49	[0 90 45 - 45 0 90] _S	1.49	2.93	0.38
	6	2.52	5.78	0.73		2.41	4.11	0.59
	7	2.14	2.83	0.50		5.64	3.11	0.38

Table 3.2: Frequency shifts of a cantilever beam of [0 90]_{3S} and [0 90 45 - 45 0 90]_S composites

In Figs. 3.7 and 3.8, the 6-th eigenvector of displacements and curvatures is plotted for both stacking sequences and for the extensions I, II and III. The undamaged one is represented by 0. The influence of the stacking sequence and position of the delamination in the thickness is clearly noted in the delaminated area, since the eigenvector is quite different in this area for non-centered delaminations (extension II) and for the [0 90 45 - 45 0 90]_S composite. Centered delaminations always give (for

	Mode	Displacement w				Curvature κ			
		I	II	III	IV	I	II	III	IV
$[0\ 90]_{3S}$	5	6.57	13.64	2.11	0.14	29.52	51.51	15.24	4.95
	6	10.49	20.19	3.44	0.23	43.60	59.85	18.90	6.04
	7	16.60	26.11	4.52	0.29	67.59	54.47	15.63	4.91
$[0\ 90\ 45\ -45\ 0\ 90]_S$	5	7.44	10.71	1.61	0.10	65.78	39.46	11.65	3.54
	6	18.97	16.16	2.66	0.18	136.99	48.70	14.28	4.43
	7	92.12	20.56	3.42	0.22	555.13	42.41	12.89	3.55

Table 3.3: Damage indexes DI (%) for displacements w and curvatures κ of a cantilever beam of $[0\ 90]_{3S}$ and $[0\ 90\ 45\ -45\ 0\ 90]_S$ composites

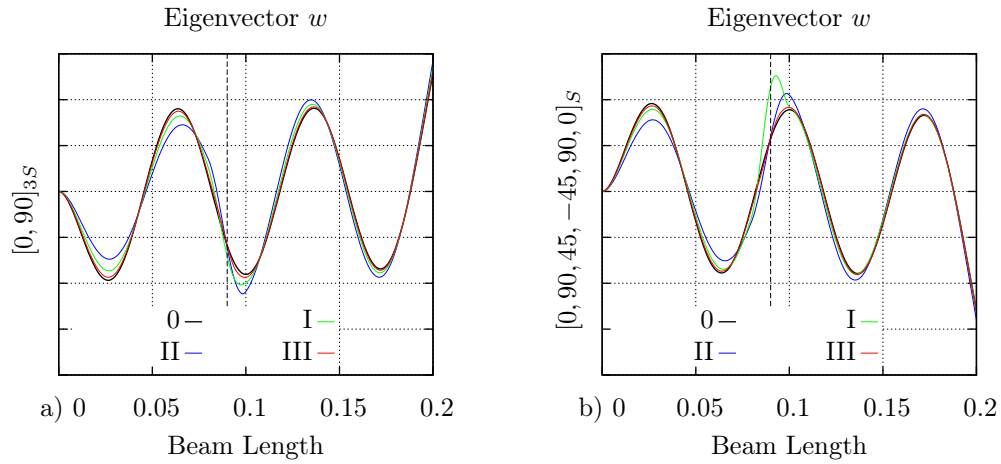


Figure 3.7: Eigenvector 6 of displacements for extensions I, II and III. a) Composite $[0\ 90]_{3S}$. b) Composite $[0\ 90\ 45\ -45\ 0\ 90]_S$. The undamaged one is represented by 0. The vertical dashed line represents the center of the delamination.

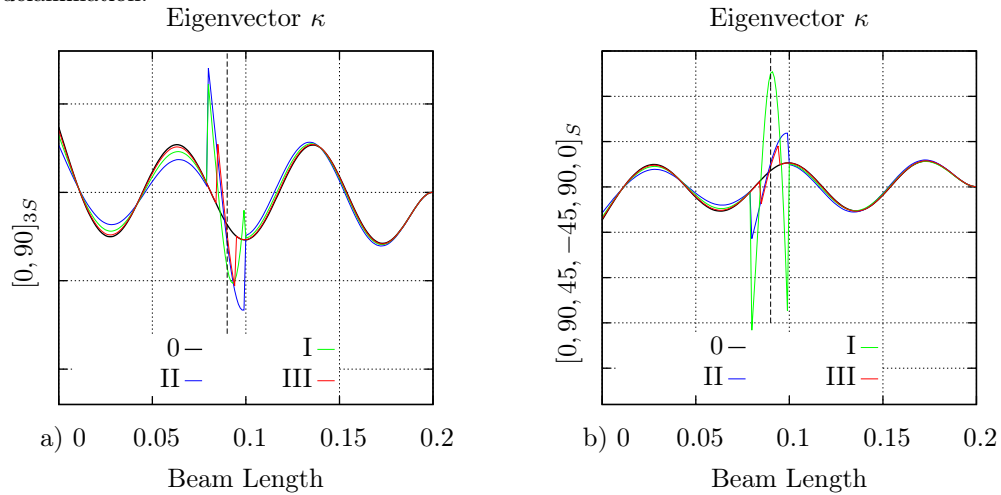


Figure 3.8: Eigenvector 6 of curvatures for extensions I, II and III. a) Composite $[0\ 90]_{3S}$. b) Composite $[0\ 90\ 45\ -45\ 0\ 90]_S$. The undamaged one is represented by 0. The vertical dashed line represents the center of the delamination.

every composite and position in the thickness) greater differences between the mode shapes outside the delaminated area. This result is very important in the case of plates, since the information would

be taken at sections not necessarily across the delamination (See F1 and F2 in the plate of the next subsection).

Finally, location and extension delamination parameters are studied for the composite $[0\ 90]_{3S}$. Figure 3.9 shows the relationship between frequency shifts and the location and size of delamination for modes 5, 6 and 7. When the location changes, the delamination length is assumed to be 10%; and when extension changes, position is assumed at $x = 0.45 L$. Figure 3.10 shows the 6-th eigenvector of displacements for different delamination locations. In all cases, delamination is supposed to be between 6-th and 7-th plies. Having more information at different points of the beam, mode shapes prove more relevant for damage detection than frequency shifts.

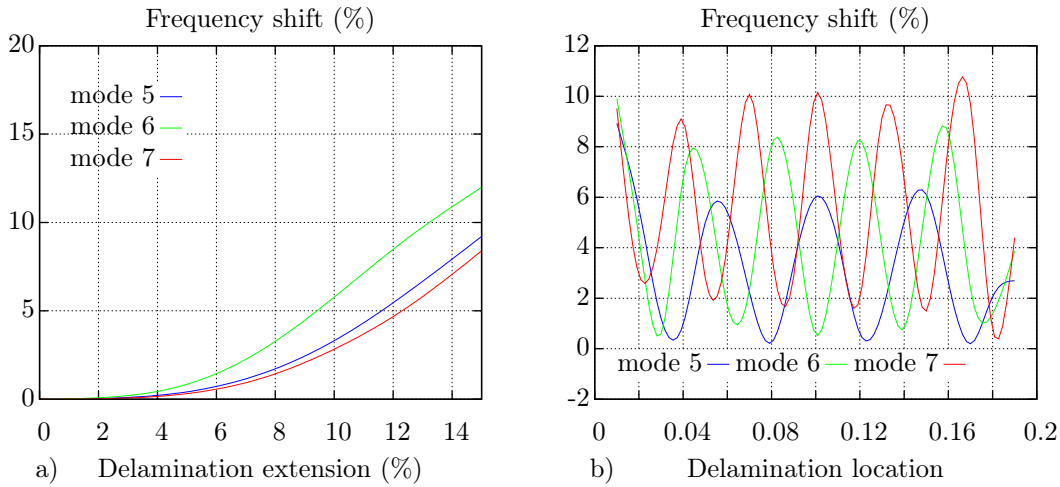


Figure 3.9: Frequency shifts (%) for composite $[0\ 90]_{3S}$ for modes 5, 6 and 7. a) Influence of the delamination extension. Delamination center at $x = 0.45 L$. b) Influence of delamination location, with extension 10%.

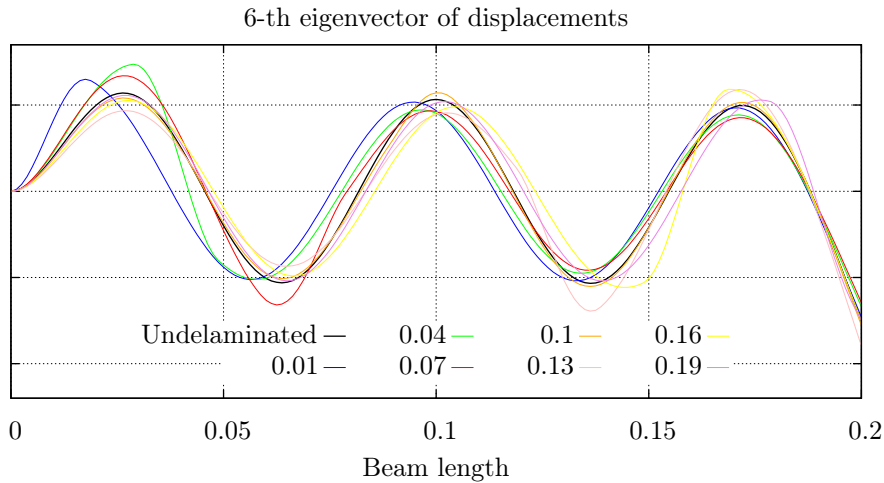


Figure 3.10: Eigenvector 6 of displacements for different delamination locations. Extension is 10%.

3.4.2 Plates

A composite clamped plate of dimensions 1.1×1.0 m is also studied. The mechanical properties of the ply have been considered to be $E_x = 150$, $E_y = 11.5$, $G_{xy} = 5$ GPa, $\nu = 0.42$, $\rho = 1560$ kg/m³ and constant ply thickness $t_p = 0.188$ mm. The composite is a 14 layer $[0, 90, 0, 90, 0, 90, 0]_S$. In this case only one delamination in the thickness is considered ($n_d=1$), whose sizes are described in Table 3.4. The stacking sequence of the laminate is $[0\ 90]_{3S}$.

Extension	Dim.(x) (cm)	Dim.(y) (cm)	Delam. area (%)	Position in thickness
I	18.8	18.0	3.0%	centered
II	14.4	14.0	2.0%	centered
III	11.0	10.0	1.0%	centered
IV	8.80	8.0	0.7%	centered
V	6.60	6.0	0.4%	centered
VI	4.40	4.0	0.2%	centered
VII	18.8	18.0	3.0%	between plies 3-4
VIII	14.4	14.0	2.0%	between plies 3-4
IX	11.0	10.0	1.0%	between plies 3-4
X	8.80	8.0	0.7%	between plies 3-4
XI	6.60	6.0	0.4%	between plies 3-4
XII	4.40	4.0	0.2%	between plies 3-4

Table 3.4: Delamination sizes and position in the thickness for the $[0\ 90]_{3S}$ composite plate

Clamped plate

$$\begin{aligned} u_0 = v_0 = w_0 &= 0 \\ \theta_{x0} = \theta_{y0} &= 0 \\ u_1 = v_1 = w_1 &= 0 \\ \theta_{x1} = \theta_{y1} &= 0 \end{aligned}$$

Ply Properties

$$\begin{aligned} E_x &= 150\text{ GPa} \\ E_y &= 11.5\text{ GPa} \\ G_{xy} &= 5\text{ GPa} \\ \nu &= 0.42 \\ \rho &= 1560\text{ kg/m}^3 \\ t_p &= 0.188\text{ mm} \end{aligned}$$

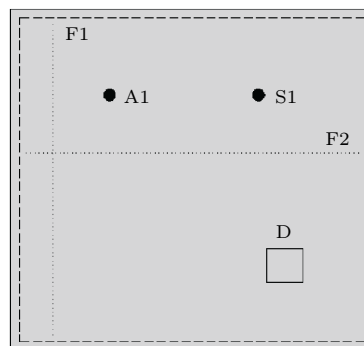


Figure 3.11: Composite clamped plate. Sections where eigenvectors are obtained (F1 and F2). Actuator (A1). Sensor (S1). Delamination (D).

Thus, 6 delamination sizes and two different positions in the thickness are considered. Their location in the top-view of the plate can be seen in Fig. 3.11. The delamination is also expressed in terms of the area of the delamination with respect to the total area of the plate. This percentage is used to establish two kinds of delaminations: “type 1” and “type 2”. The limit is established in 1% of the area of the plate. The largest delamination of Table 3.4 occupies a 3% of the area of the plate, which is not a considerable damaged area. The center of the delamination (D) is always at coordinates $x = 0.83$ m and $y = 0.25$ m. Two selected sections (F1 and F2) are defined for plotting the results. They could represent two optical fibers embedded in the plate, where the mode shapes are obtained.

Damage indexes

Tables 3.5 and 3.6 show some damage indexes (DI) for all the extensions and the two selected sections of the plate (F1 and F2). The undamaged one is represented by 0. For plates, because of their 2D behaviour, damage indexes tend to increase but not monotonically. Accordingly, depending on the mode and selected section, the damage index for displacements could be greater than for curvatures. As expected, for delamination areas smaller than 1% of the area of the plate (extensions IV, V, VI, X, XI and XII), higher modes are required to detect the damage. Concerning the position of the delamination in the thickness, the damage index tends to decrease when the delamination is away from the center.

Mode	Displacement w			Curvature κ_x		
	I	II	III	I	II	III
1	0.65	0.24	0.06	0.69	0.26	0.09
2	28.82	11.05	2.90	11.14	4.13	1.07
3	6.80	2.55	0.67	18.29	6.98	1.82
	VI	V	VI	VI	V	VI
16	12.17	3.91	0.75	9.10	2.91	0.56
17	4.61	1.39	0.26	2.19	0.69	0.13
18	7.05	2.17	0.41	34.19	10.52	1.99
	VII	VIII	IX	VII	VIII	IX
1	0.46	0.23	0.13	0.43	0.19	0.09
2	17.86	6.42	1.62	6.75	2.37	0.59
3	4.22	1.49	0.39	11.45	4.06	1.02
	X	XI	XII	X	XI	XII
16	5.57	1.89	0.49	3.91	1.18	0.32
17	2.76	0.87	0.22	1.01	0.40	0.26
18	4.20	1.32	0.26	20.89	6.71	1.31

Table 3.5: Damage indexes DI (%) for displacements w and curvatures κ_x for section $x=0.13$ m (F1) of the composite plate

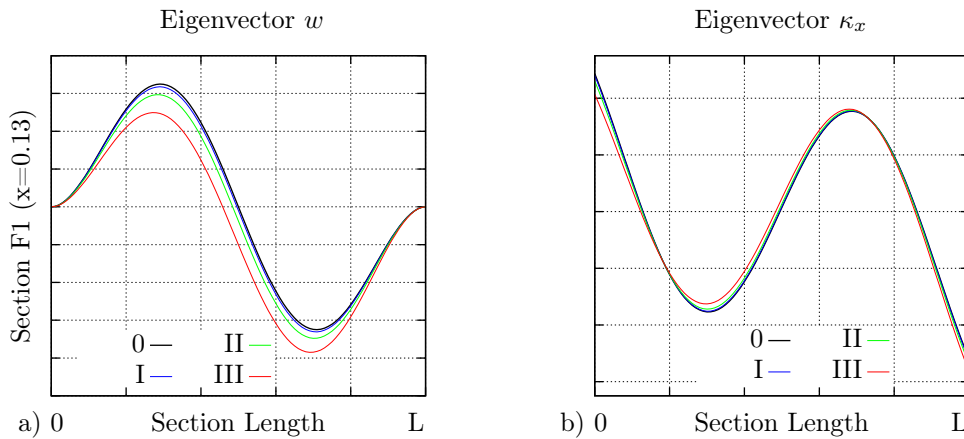


Figure 3.12: Eigenvectors of 2-nd mode at section $x=0.13$ m (F1). Extensions I, II and III. a) Displacements w . b) Curvatures κ_x .

Mode	Displacement w			Curvature κ_y		
	I	II	III	I	II	III
1	0.29	0.11	0.03	0.47	0.18	0.07
2	21.68	8.18	2.13	55.35	22.05	5.84
3	7.38	2.72	0.70	3.08	1.06	0.27
	VI	V	VI	VI	V	VI
16	11.43	3.74	0.73	82.85	30.39	6.08
17	3.80	1.15	0.22	5.55	1.67	0.32
18	5.49	1.63	0.31	4.84	1.43	0.27
	VII	VIII	IX	VII	VIII	IX
1	0.16	0.06	0.02	0.24	0.11	0.10
2	13.34	4.71	1.18	35.40	12.85	3.25
3	4.51	1.56	0.39	1.73	0.57	0.22
	X	XI	XII	X	XI	XII
16	5.25	1.80	0.45	42.09	14.75	3.57
17	1.76	0.59	0.21	2.66	1.06	0.66
18	2.96	0.93	0.28	2.06	0.65	0.40

Table 3.6: Damage indexes DI (%) for displacements w and curvatures κ_y for section $y=0.58$ m (F2) of the composite plate

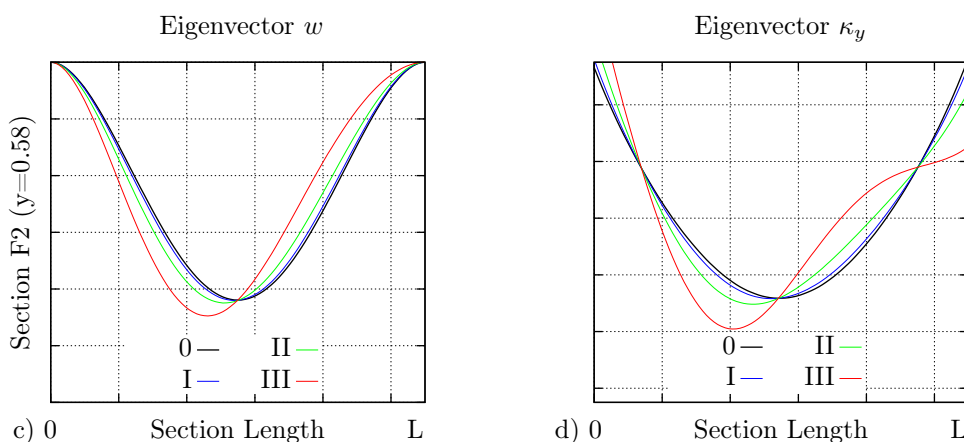


Figure 3.13: Eigenvectors of 2-nd mode at section $y=0.58$ m (F2). Extensions I, II and III. a) Displacements w . b) Curvatures κ_y .

Figures 3.12 and 3.13 represent the 2-nd eigenvector for both selected sections (F1 and F2) and for extensions I, II and III. For the rest of the cases no further plots have been included, since the results are similar. For non-centered delaminations, the eigenvectors are proportional to the one corresponding to a centered one.

From the experimental point of view, while the very promising optical fibers are still in a developing process. Fiber Bragg Grating (FBG) sensors are the ones applied most extensively at present. However they only provide local information. Alternatively, PZT sensors have well known properties and are mostly used for monitoring structures. From the measured signals, the time-domain or frequency-domain can be used for damage detection applications. In the next subsection, the damage is characterized in the frequency-domain through the use of the well known FRF.

FRF Analysis

FRF is a very effective signal processing technique for detecting damage from vibration signals, requiring only the information from some points where signals are measured, and therefore minimizing the amount of data to work with. This type of analysis is quite powerful and can detect very small damage if the selected bandwidth is large enough. It is often used to extract frequencies and mode shapes. Experimentally, this can be done using PZT elements, which can be used either as actuators or as sensors. In Fig. 3.11, A1 represents the actuator and S1 the sensor.

Considering the same plate as before, an FRF analysis can be carried out. FRF is defined as:

$$FRF_{A1/S1}(\omega) = H(\omega) = \frac{\mathcal{F}(w)}{\mathcal{F}(p)} \quad (3.11)$$

where A1 is the actuator; S1 the sensor; $H(\omega)$ is the Transfer Function of the FEM plate; ω is the frequency; \mathcal{F} denotes the Fourier Transform; $w = w(t)$ are the vertical displacements at the sensor position and $p = p(t)$ the excitation load.

Since PZT sensors give signals proportional to accelerations, the FRF used for this example will be computed from the accelerations and not from the displacements. This results in a better function, since the displacements tend to decrease with frequency. In an experiment the FRF would be obtained as the division defined in (3.11). For a numerical model, the corresponding FRF can be computed directly from the model.

In the considered plate, the excitation is at coordinates $x = 0.30$ m and $y = 0.70$ m (A1). The corresponding measured vertical accelerations are at the node of coordinates $x = 0.75$ m and $y = 0.70$ m (S1). A damping ratio of $\xi=0.003$ is assumed for all damping modes.

Figure 5.7 shows the FRF for the undamaged case 0 and all the centered delaminations of Table 3.4 with a selected bandwidth [0, 1500] Hz. Obviously, the differences between curves grow with the frequency, allowing for the detection of damage. As to be expected, very small delaminations can be detected in the high part of the bandwidth, where changes in the amplitudes (peaks) with respect to the undamaged plate clearly occur. Several criteria can be used to classify the damage, such as frequency shifts, mode shape changes, damage-induced energy, etc. In this case, the frequency and respective amplitude shifts, extracted from the FRF, are used, here defined as damage indexes. In the case of the amplitudes, they could be positive or negative, depending on the considered amplitude; some increase and others diminish. These damage indexes are defined as follows:

$$DI_F = \frac{F_0 - F_1}{F_0}; \quad DI_A = \frac{A_0 - A_1}{A_0} \quad (3.12)$$

where F and A denote eigenfrequency or amplitude; 0 represents the undamaged plate and 1 the delaminated one.

For "type 1" delaminations, a close-up of bandwidth is selected, [120-320] Hz, where 5 damage indexes for eigenfrequencies and their respective amplitudes are computed. For "type 2" ones, the close-up of the bandwidth selected is [1025-1225] Hz. Analogously, 5 damage indexes for eigenfrequencies and amplitudes are computed. Table 3.7 shows these damage indexes. As expected, higher frequencies are required to detect very small delamination sizes.

Figure 3.15 shows the close-up of the bandwidth where the damage indexes are computed. As is well known, eigenfrequencies tend to decrease with the presence of damage. Exceptionally, and for higher modes, some of them can increase, resulting in a negative damage index (see eigenfrequency: 1139

Hz in Fig. 3.15b The results show that frequency changes are not very significant, while amplitude changes are more sensitive to the presence of damage.

From these results it can be concluded that damage may be detected with a relatively small bandwidth. Damage indexes of amplitudes are more sensitive, as is the case of modal shapes. For very small delaminations, higher frequencies are required. While the damage indexes of amplitudes are appreciable in the high part of the bandwidth, the damage indexes of eigenfrequencies tend to decrease along with delamination size (see Table 3.7).

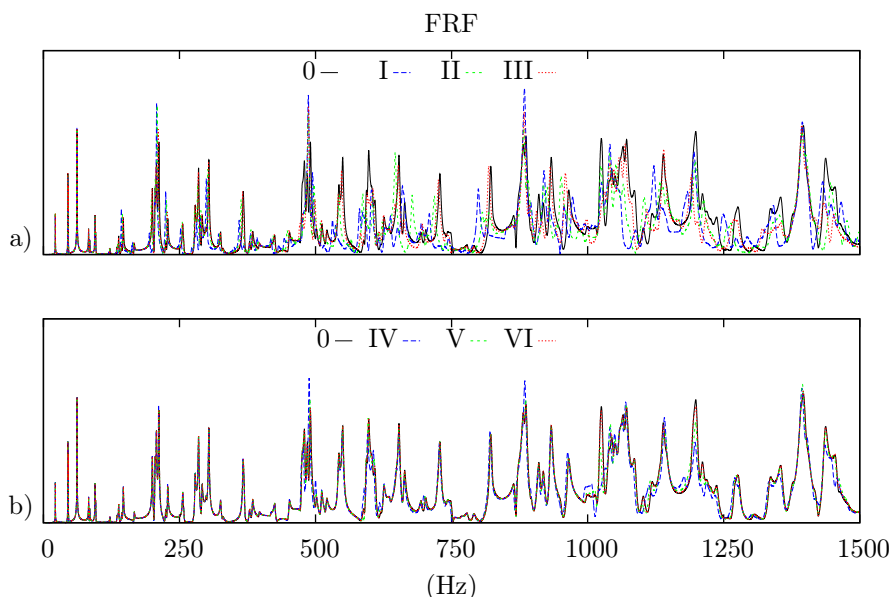


Figure 3.14: FRF at location $x = 0.75$ m and $y = 0.30$ m. a) Extensions 0, I, II, III. b) Extensions 0, IV, V and VI.

Extension	Eigenfrequency (DI_F)					(Hz)	Amplitude (DI_A)				
	200.2	207.6	212.2	228.6	256.0		200.2	207.6	212.2	228.6	256.0
I	2.80	3.32	1.98	1.75	1.45		67.92	94.14	-34.66	-78.00	11.28
II	0.90	0.96	1.46	1.09	0.43		17.87	17.23	-32.43	-51.54	8.48
III	0.20	0.34	0.57	0.44	0.12		0.36	4.88	-11.11	-18.59	-3.25
Extension	1051	1072	1086	1119	1199	(Hz)	1051	1072	1086	1119	1199
IV	0.00	0.19	0.28	0.63	0.17		-13.51	-4.69	10.26	8.95	34.57
V	0.05	0.09	0.09	0.36	0.08		-6.87	-3.03	3.19	-1.33	18.58
VI	0.10	0.09	0.00	0.09	0.00		-0.15	-0.78	0.38	-0.22	5.36

Table 3.7: Damage indexes DI_F and DI_A (%) for selected Eigenfrequencies: 200.2, 207.6, 212.2, 228.6 and 256.0 (Hz) for extensions I, II and III; 1051, 1072, 1086, 1119 and 1199 (Hz) for extensions IV, V and VI

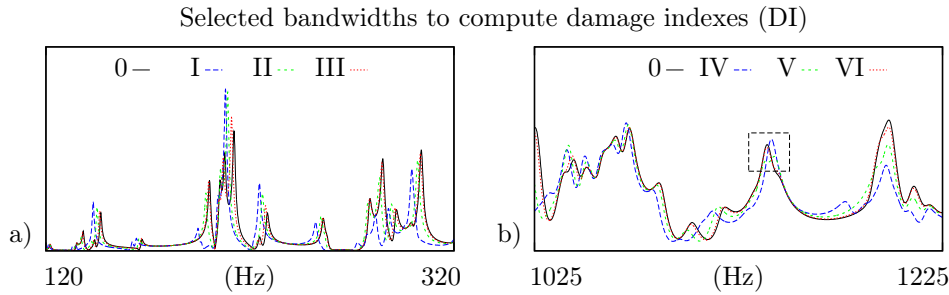


Figure 3.15: Selected bandwidths of FRF (to compute damage indexes). a) Extensions 0, I, II, III. b) Extensions 0, IV, V and VI. Marked eigenfrequency: 1139 Hz.

3.5 Conclusions and further work

In this paper a methodology for defining delaminations is used to develop a 4-node delaminated composite Finite Element. Based on similar approaches to FEM, the accuracy of this methodology was tested. Relative errors of the L_2 -Norm for the developed element were studied for 2 *Benchmark* problems and compared with the case of considering the fracture with separate elements ("4 Region Approach"). Similarly, relative errors in the first eigenfrequencies were compared for both formulations. The conclusion is that the two formulations provide the same results regardless of the selected mesh, confirming this formulation as a better means of model delamination.

It has also been proven that this methodology leads to elements that always pass the "Patch Test" if the selected FEM elements used to build the delaminated one (DKQ and QMITC in this case) also pass the "Patch Test" for the uncoupled single problems. In future work, the authors plan to extend this methodology to HOT elements for composite shells with other uncoupled FEM formulations, as a generalization of the fracture model.

Finally, some results in the field of SHM have been presented for beams and composite plates, studying the effect of delamination on some of the dynamic damage indicators used in the damage detection techniques, reconfirming some known relationships between them, and presenting the developed element as a tool for model based strategies.

Chapter 4

Experimental analysis of orthotropic composite plates. Comparison with numerical results

This chapter describes experiments performed in three composite orthotropic plates of stacking sequence $[0\ 90]_{3S}$. Two of these plates present an internal delamination in the mid-surface of two different sizes. FRF analysis were carried out and compared for the three plates. Results show how the FRF analysis can be a powerful tool to detect the delamination. However, the experiment showed some limitations due to the variability associated with the experiment itself. Additionally, the same plates were studied with the numerical method developed in Chapter 3, obtaining similar results from a qualitative point of view.

4.1 Introduction

The use of advanced composite materials has grown in recent decades. From the structural point of view, their stiffness, weight, fatigue-life and strength limit make this kind of material very attractive.

It is well known that the delamination or debonding of adjoining plies is one of the most frequent types of damage in composite structures. This modifies the carrying capacity of the structure and can lead to catastrophic consequences if they are large enough. Therefore, delamination detection is an important issue in the maintenance tasks.

In the context of SHM, several damage identification methods based on the change of eigenfrequencies, mode shapes, damping ratios, FRF, etc., have been used to identify and evaluate damage. This challenge is usually subdivided into four levels of damage [32] (I: detection, II: localization, III: severity and IV: remaining life). Improvements in terms of location (levels II and III) can be performed by the use of modal shapes, the curvature shapes being more powerful than displacement ones. All the identification techniques involve a compromise between the severity of damage and the number of modes required to be able to detect damage. Interested readers can find detailed information in [33, 34, 35, 36, 37, 68].

Zak et al. [44, 45] studied the vibration of delaminated composite beams and plates. Changes in eigenfrequencies were validated in a finite element model and experimental data. Hanagud and Luo [46] studied a composite plate based on measured structural dynamic response. Analytical models were constructed to predict the dynamic response of the damaged structure, based on the computation of appropriate damage indexes, obtained from the mode shapes. The influence in frequency shifts and

FRF due to debonding on sandwich panels was studied by Kim and Hwang in [47] with good agreement with numerical results. Krawczuk et al. [48] identified and locate damage in a laminated composite beam using frequency shifts as inputs. The model was validated with numerical tests. Ling et al. in [49] used fiber-optic sensors to measure FRF, which is used to detect and identify the size and location of delaminations in composite beams. Results were also validated with a numerical model. Sanders et al. in [51, 52] discussed the subject of detecting delamination within composites with neural networks. Fiber-optic sensors were used to measure the first five modal frequencies of several glass/epoxy composite beams. Harrison and Butler used a genetic algorithm to locate delamination on beams in [53] using frequency shifts and mode shapes. Zwink have located damage in composite specimens due to impact loads with vibration-based techniques considering the non-linear response in [55]. Finally, Saravanos and Hopkins studied in [56] the change of damping ratios in cantilever composite beams and compared the results with numerical simulations.

In this work, damage (delamination) is identified for two composite plates through the use of FRF analysis. Experimental results are also compared with numerical simulations based on the delaminated element developed in [68].

4.2 Description of the composite SEDA plates and the experiment

As part of the Project "Application of advanced signal processing techniques to damage detection and characterization (SEDA)", three composite plates were fabricated by INTA (Instituto Nacional de Técnicas Aeroespaciales) in Madrid. All of them were orthotropic plates of stacking sequence [0 90]_{3,5}, called SEDA plates. The experimentation and numerical analysis was funded by the Project P08-TEP-03641, "Detección de defectos en materiales compuestos avanzados de uso aeronáutico mediante técnicas vibro-acústicas y modelos de optimización (DEMAC)". The mentioned plates have the following ply properties:



- Thickness 0.188 mm;
- $E_x=150$ GPa;
- $E_y=11.5$ GPa;
- $G_{xy}=5.0$ GPa;
- $\nu_{xy}=0.42$ GPa;

being the total thickness of the plate 2.256 mm.

Two of these plates presented an internal delamination between layers 6 and 7 (mid-surface). In the first case (plate 5S2/2) the delamination size was 80x80 mm, whereas in the second case (plate 5S2/3) the size was 180x180 mm. In order to ensure the debonding between the plies a thin teflon was placed between both plies. The plate (5S2/1) represents the undelaminated plate. Figure 4.1 presents the geometry of the plates and the delamination sizes.

The performed experiment consisted on the vibration of these plates in a fully clamped configuration. For that a special steel frame was designed and built to be able to fix the plate through a system of screws. A pair force of 55 N·m was applied to ensure that the plate was clamped along the 4 edges. Once the plate was inside the frame, the clamped dimensions of the plate were 850x650 mm. Additionally, an anti-vibration table was used to avoid ground vibrations. In Figure 4.2 both frame and table can be seen.

A electric signal generator of the PULSE-System from Brüel and Kjaer was used to excite the plates through a piezoelectric element (PZT) used as actuator (A1). Additionally, two PZT sensors (S1, S2)

 MINISTERIO DE DEFENSA	SECRETARIA DE ESTADO DE DEFENSA	Doc. N°.: XF/RPT/4320/024/INTA/08	
	 INSTITUTO NACIONAL DE TÉCNICA AEROSPACIAL	Página: 9 de 20	Edición: 02

ANEXO I. PANELES FABRICADOS

Las tablas A1.1 y A1.2 proporcionan información acerca de los paneles fabricados.

Tabla A1.1. Descripción de los paneles fabricados para ensayos de vibraciones

Ref.	Secuencia laminación	Dimensiones (mmxmm)	Ciclo de Curado ¹	Observaciones
5S2/1	[90/0] _{3S}	900 x 700	H0820	Pisa: no Retenedores: no Tejido pelable: no Delaminación: si ²
5S2/2	[90/0] _{3S}	900 x 700	H0820	
5S2/3	[90/0] _{4S}	900 x 700	H0820	

¹ Detalles del ciclo de curado en Anexo II

² Delaminación en el plano medio del laminado. Su tamaño y situación están esquematizadas en la Figura 3.

Tabla A1.2. Descripción de los paneles fabricados para probetas de ensayo para determinar módulo transversal, relación de poisson y contenido volumétrico en fibra.

Ref.	Secuencia laminación	Dimensiones (mmxmm)	Ciclo de Curado ¹	Corte ²	Observaciones
5S2/4	[0] _e	300 x 100	H0820	1	Pisa: si Retenedores: no Tejido pelable: no
5S2/5	[90] ₁₁	150 x 300	H0820	2	

¹ Detalles del ciclo de curado en Anexo II

² Esquemas de corte en Anexo III

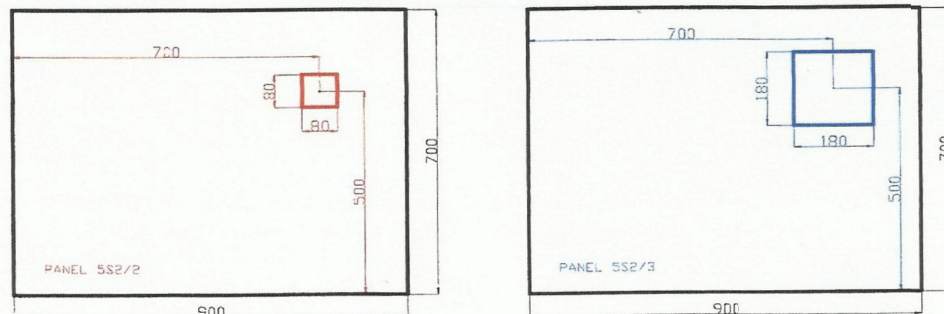


Figure 4.1: SEDA [0 90]_{3S} composite plates.

registered the electric signals due to the vibration of the plate, which were finally recorded and digitalized by the PULSE-System. Figure 4.2 shows the complete experiment setup. Detailed information of the PULSE-System, the instrumentation methodology and PZT characteristics can be found in [69] and [70].

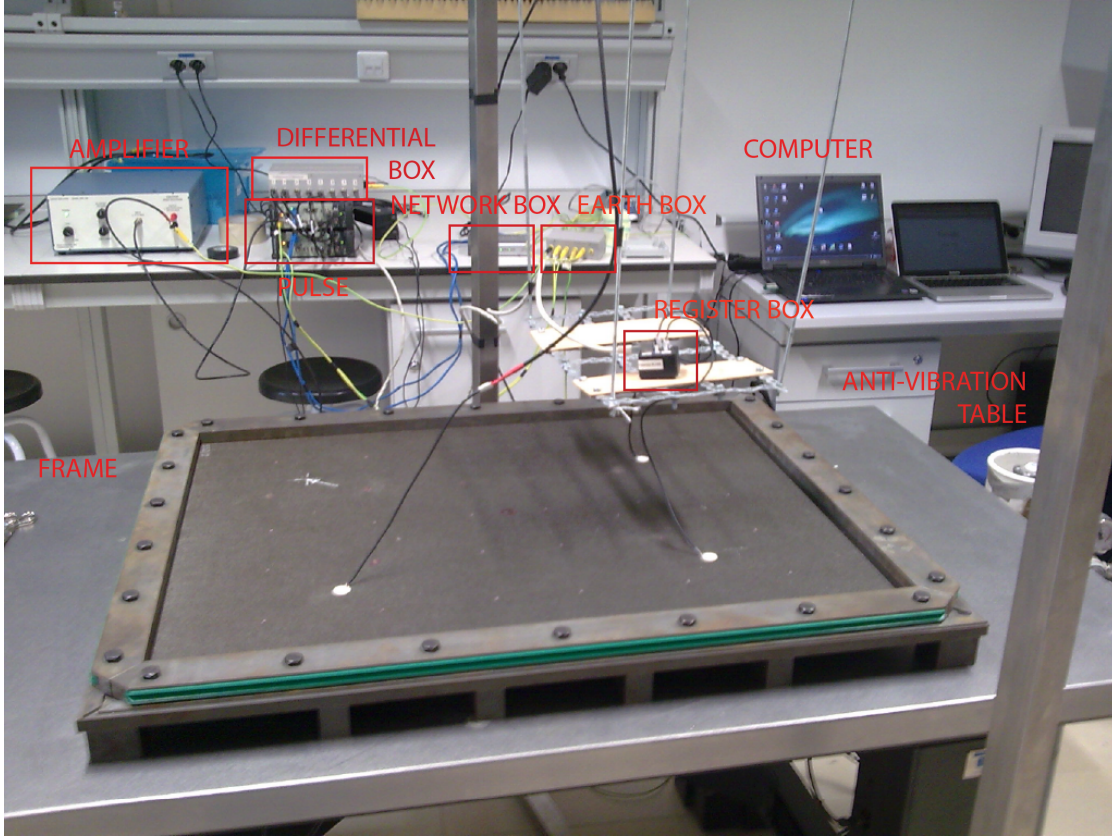


Figure 4.2: PULSE-System and SEDA plate on the steel frame instrumented with one actuator and two sensors.

Concerning the composite plate, it was instrumented with an actuator (A1) and two sensors (S1, S2), which were connected to the PULSE-System through convenient connections boxes manufactured by the personal of the SNADS group. Figure 4.3 shows the PZT used as actuator and sensors, which were the same type, both in size and properties. Table 4.1 describes the properties of this PZT element.

Model	Ceramic	Electrodes	Geometry	Diameter	Thickness
PRYY+0796	PIC255	Ag	Circular	20 mm	0.5 mm

Table 4.1: PZT used as Actuator and Sensor.

The positions of the actuator (A1) and sensors (S1, S2) are described in Figure 4.4. All of them were placed away from the delamination to present a more general case of study. For the sake of brevity, in this chapter only the response of sensor 2 is presented, since results using sensor 1 were quite similar.



Figure 4.3: PZT used as Actuator and Sensor.

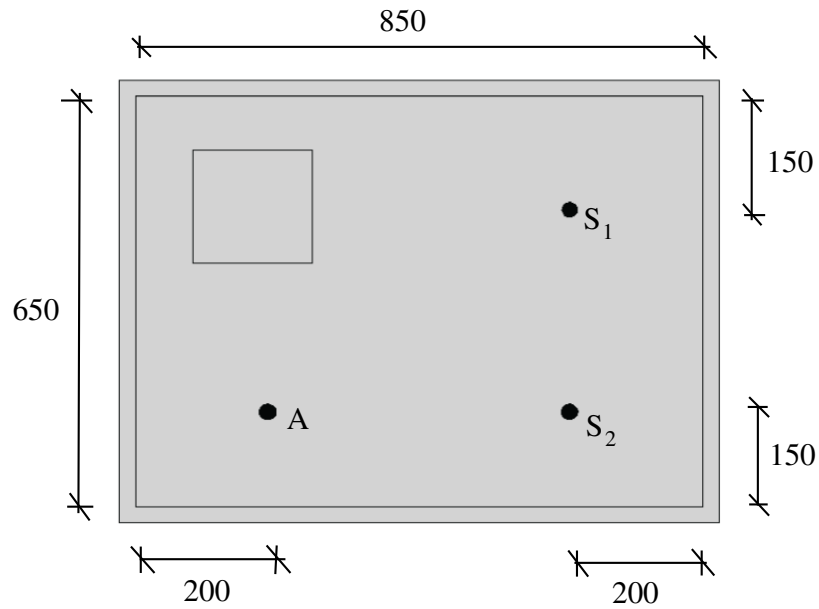


Figure 4.4: Actuator and sensor positions. Clamped dimensions. All data in mm.

4.3 Experiment

For all the experiments performed the following characteristics were used:

- A random white-noise as excitation signal;
- Sampling frequency [0 8192] Hz;
- Frequency excitation range of [0 6400] Hz;
- Measurement length 32 s;
- Analyzed bandwidth [0 3500] Hz.

These properties were set in the software of the PULSE-System and finally the actuator and sensors signals were recorded in the computer. It is important to keep in mind that once signals are registered,

they must be normalized, due to different issues concerning the instrumentation, such the use of different PZT elements and the effect of the used glue to fix the PZT. In particular, signals were normalized by equation (4.1), resulting in a signal of mean zero and standard deviation one, i. e.

$$x_N = \frac{x - \bar{x}}{\sigma} \quad (4.1)$$

where x_N is the normalized signal, \bar{x} represents the mean of the signal, x is the recorded signal and σ the standard deviation of the recorded signal.

4.4 Experiment variability

As it was already pointed out, the experiments were performed on three different plates, therefore some variability and limitations had to be expected. In order to proof that the instrumentation of each single plate and that the PULSE-System did not present any variability, all the plates were tested over a foam several times at different days, obtaining a variability of results close to zero. Figure 4.5 shows one of SEDA the plates over the foam.

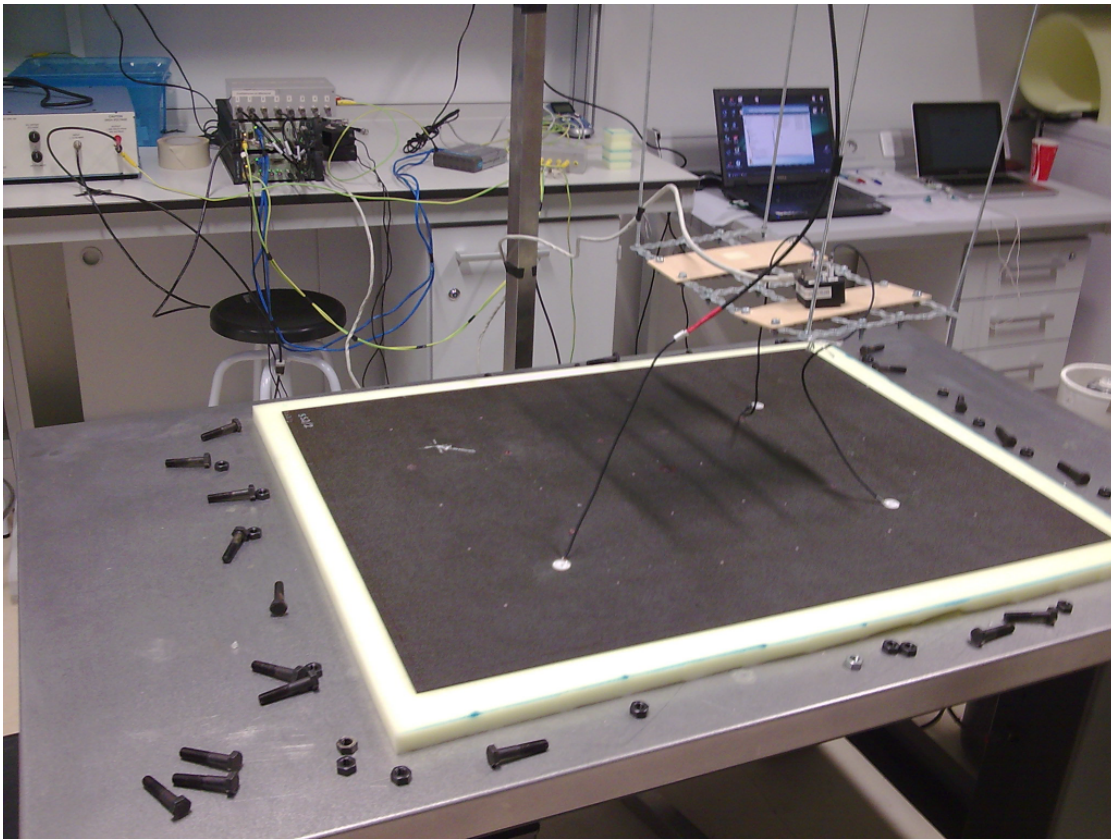


Figure 4.5: SEDA plate over foam.

Figure 4.6 shows the FRF's of three different experiments performed at several days. The three different FRF of this correspond to the undelaminated plate over the foam (see Figure 4.5) and have practically the same response. Therefore no variability of the instrumentation system was observed. Similar results were obtained in the other plates, but for the sake of simplicity, only results for the undelaminated plate are presented here.

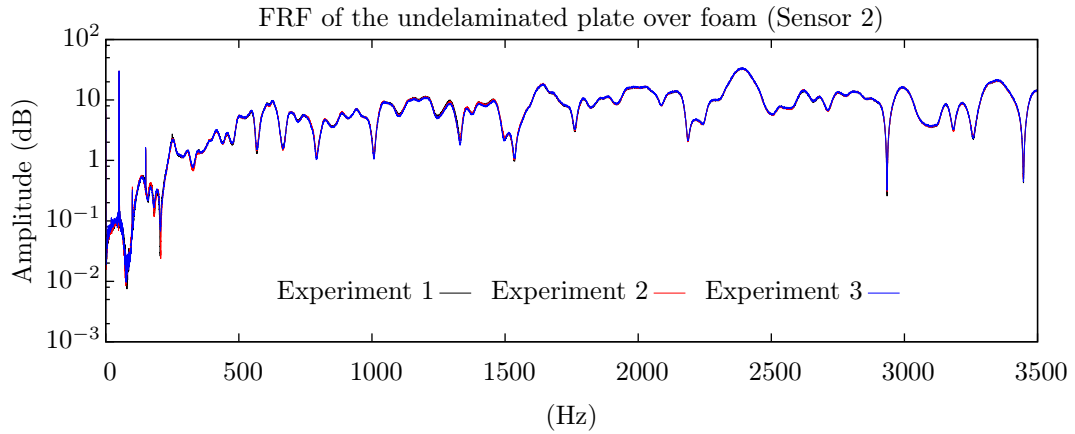


Figure 4.6: Variability of instrumentation system for undelaminated plate.

In order to test the variability of the fixation system and the fact that the instrumentation of the three plates and the plates themselves were different (different PZT, the exact position of the PZT in three different plates, etc.), the plates were disposed several times and the screws were adjusted several times on the frame. As a result of these experiments a variance for the frequency response of about 1-3 Hz for the lower frequencies and about 5 Hz for the highest ones were founded. Figure 4.7 presents the six different experiments, where a small variation of the FRF can be appreciated. For clarity, the bandwidth has been divided in two plots, one from [0 1500] Hz and the other from [1500 3500] Hz.

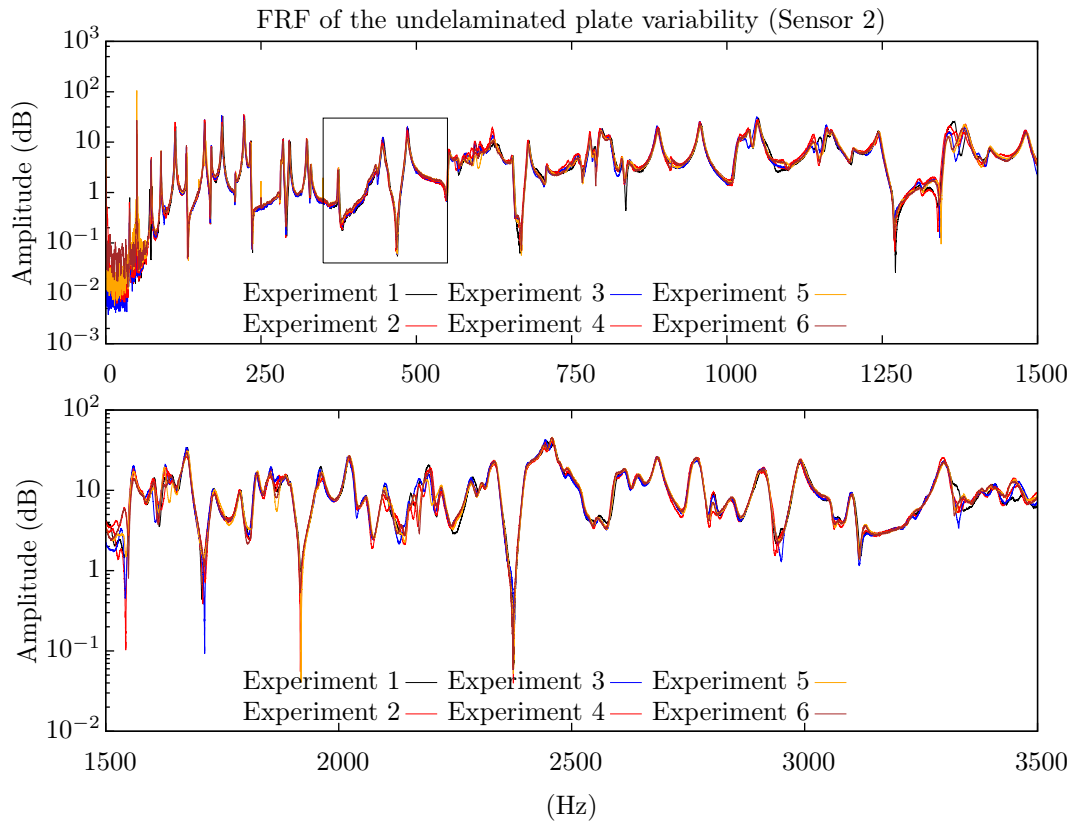


Figure 4.7: Variability of the FRF for the undelaminated clamped plate.

So for this experiment, an error depending on the frequency between 1-5 Hz was assumed. In this case, a total number of six experiments were performed, three performed in one day and three in other

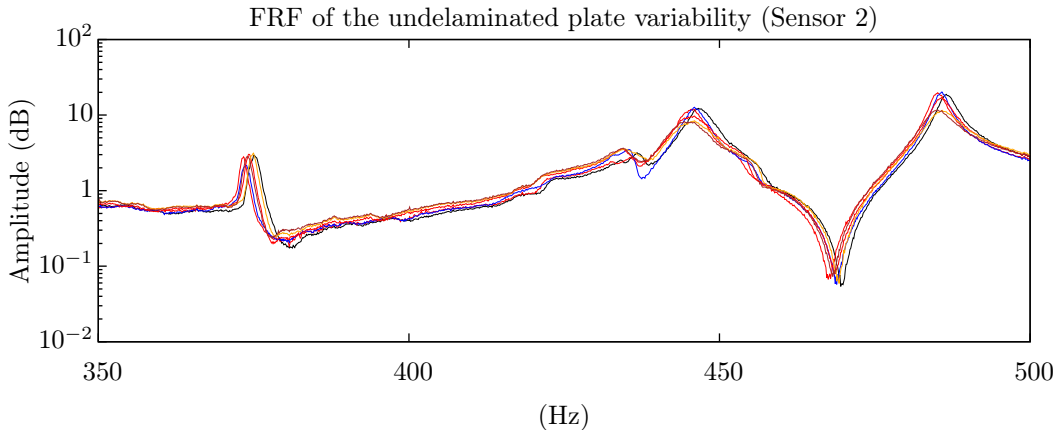


Figure 4.8: Variability of the FRF for the undelaminated clamped plate. Frequency band [350 500] Hz.

day. At each of these three experiments, the screws were adjusted again to the pair force of 55 N·m in order to introduce the variability associated with the boundary conditions. It is important to keep in mind that before every experiment was performed, plates were free of in-plane stresses associated of temperature changes, since the pair force was set to zero and adjusted to the maximum pair force.

Despite the fact that the signals were normalized, amplitudes of the FRF can not be strictly compared since the instrumentation was not exactly the same for the three plates and the fact that the colocation of the PZT can present some differences (in position and amount of glue). In Figure 4.8 a closer look to the different FRF was made. Variabilities of about 50% in the linear scale or more were founded. It was then really difficult to set a clear variance for the amplitudes and therefore they should be only taken into account if the differences are quite considerable.

4.5 Experimental results

Once a magnitude of the frequency variability was fixed, the experiments of the three different plates were performed, in order to study the possibility of damage identification with the use of FRF. The same excitation characteristics described before (section 4.3) were used for all the experiments.

In the following figures, FRF of the undelaminated plate is compared with the FRF of both delaminated ones. For clarity, it has been separated the 80x80 mm delamination of the 180x180 mm delamination. Also for clarity, the studied bandwidth has been divided in two bands; [0 1500] Hz and [1500 3500] Hz.

Firstly, Figure 4.9 shows the effect of the delamination of 80x80 mm in the SEDA composite plate. It can be seen how higher frequencies are required in order to clearly distinguish the effect of delamination, for amplitudes and frequencies. For frequencies greater than 1500 Hz the effects of the delamination were quite considerable. For frequencies lower than this value, not every frequency shift between delaminated and undelaminated plates was clearly identifiable since it was in the range of the variability of the experiment. However some of them were noticeable. In the next section of this chapter a closer look to the first bandwidth is performed.

Secondly the results for the plate with a delamination of 180x180 mm are presented in Figure 4.10. Here for all the frequencies the differences were quite considerable, pointing out this delamination as easily identifiable. However, this is a large delamination for the purpose of aeronautical applications and therefore the results can be taken into account in order to proof the damage detection technique, but maybe not for practical issues.

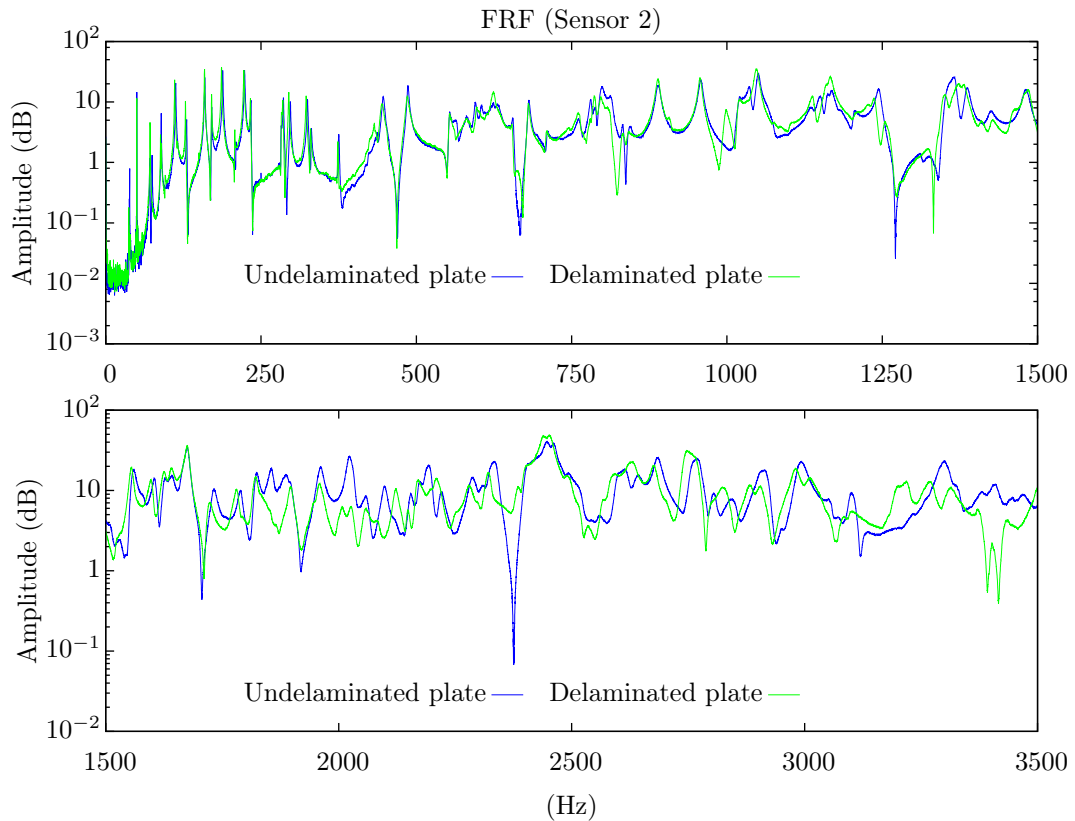


Figure 4.9: FRF of the undelaminated and 80x80 mm delamination plates.

Results point out the following conclusions:

- In order to detect the small delamination (80x80 mm), higher frequencies are required (>1500 Hz in the used plate).
- The delamination of 180x180 mm is easily detectable in all the bandwidth.
- A generalized tendency of diminishing natural frequencies of the plate due to damage (but not everyone) is appreciated.

As expected, higher frequencies were required in order to detect small delaminations. This is however a well known result in the field of SHM. If no scale influence is assumed, the small delamination would be about 40-50 mm in an aeronautical panel, since the considered clamped plate was of 850x650 mm.

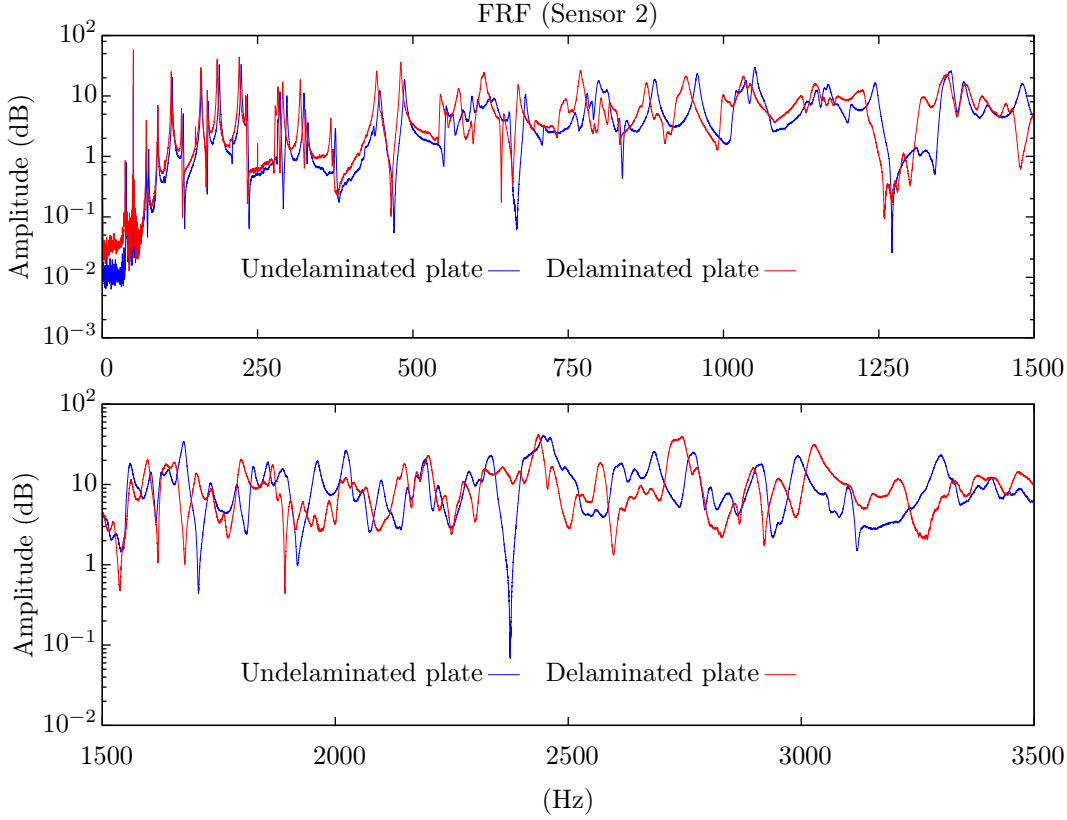


Figure 4.10: FRF of undelaminated and 180x180 mm delamination plates.

4.6 Comparison with numerical results

The performed experiments were also studied from a numerical point of view with a numerical model, developed in [68]. This model is based on a CLT theory which introduces the delamination in the kinematic equations through the following expression:

$$\begin{aligned}
 u(x, y, z) &= u_0(x, y) + \theta_{y0}(x, y)z + \sum_{r=1}^{n_d} \left[u_r(x, y) + \theta_{y_r}(x, y)z \right] H(z - z_r) \\
 v(x, y, z) &= v_0(x, y) + \theta_{x0}(x, y)z + \sum_{r=1}^{n_d} \left[v_r(x, y) + \theta_{x_r}(x, y)z \right] H(z - z_r) \\
 w(x, y, z) &= w_0(x, y) + \sum_{r=1}^{n_d} \left[w_r(x, y) H(z - z_r) \right]
 \end{aligned} \tag{4.2}$$

where u , v , and w are displacements; θ_x and θ_y are rotations; H is the Heaviside step function; the subscript 0 indicates mid-plane quantities and n_d is the number of delaminations considered. Variables with subscript r are the new degrees of freedom describing the kinematic discontinuities across the r -th delamination. These new variables represent relative displacements and rotations between plies. Further details on the element formulation can be found in [68].

Figure 4.11 shows the finite element model of the plate for the 80x80 mm delamination. The mesh is of 170x130 elements.

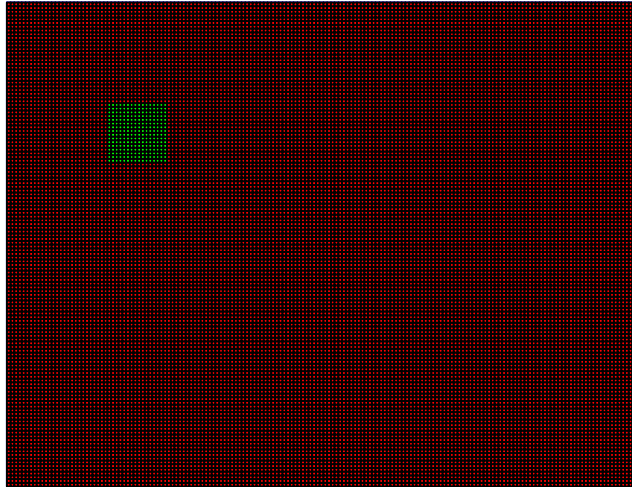


Figure 4.11: Finite element model of the delaminated plate. Delamination 80x80 mm.

In general the influence of the delamination was quite similar for both cases, although theoretical and experimental results does not fit, for multiple reasons (used composite theory, variability of geometric parameters and elastic parameters, contact and friction effects, etc.).

However, the experiments validate what the theory predicted and show also the limitations of the Finite Element Method in order to perform damage detection strategies based on models. They should only be used from a comprehensive point of view in this field.

The numerical study was performed twice. Firstly, with the composite values given in 4.3; secondly, with an inverse optimization of the parameters in order to have a better approach of the numerical solution.

4.6.1 Comparison with the given parameters

As in the previous section, the effect of the two delamination sizes was studied separately. Figures 4.12-4.14 shows the effect of the delamination of 80x80 mm in the SEDA composite plate. In this case however results are presented in three separated bandwidths: [0 500] Hz, [500 1500] Hz and [1500 3500] Hz. The first bandwidth, is from a comprehensive point of view the most interesting one, since a really high similarity between experimental and numerical FRF's can be found. However several assumptions make that the results can not fit as it was already mentioned (used composite theory, variability of geometric parameters and elastic parameters, contact and friction effects, etc.).

It was found that for frequencies lower than 1500 Hz, only some of the frequency shifts due to delamination in the numerical result were quite noticeable and greater than the variability of the experiment. Something similar happened with the amplitudes of the FRF, but at some of the resonant peaks, both frequency shifts and amplitudes changes between delaminated an undelaminated plates were big enough to identify the delamination. From a practical point of view, as was pointed out before, it would be better to work up to 1500 Hz in order to detect damage, but model and experiment unfortunately lose similarity as the frequency increases.

Regarding the damping, a viscoelastic linear damping ratio of value $\xi=0.005$ for the first eigenfrequency to $\xi=0.01$ for the highest one was assumed. Values under $\xi=0.01$ practically do not modify the natural frequencies and only modify amplitudes. In this chapter, the main interest is focused on the comparison of the eigenfrequencies. Considering the adopted model, no influence at this level should be expected.

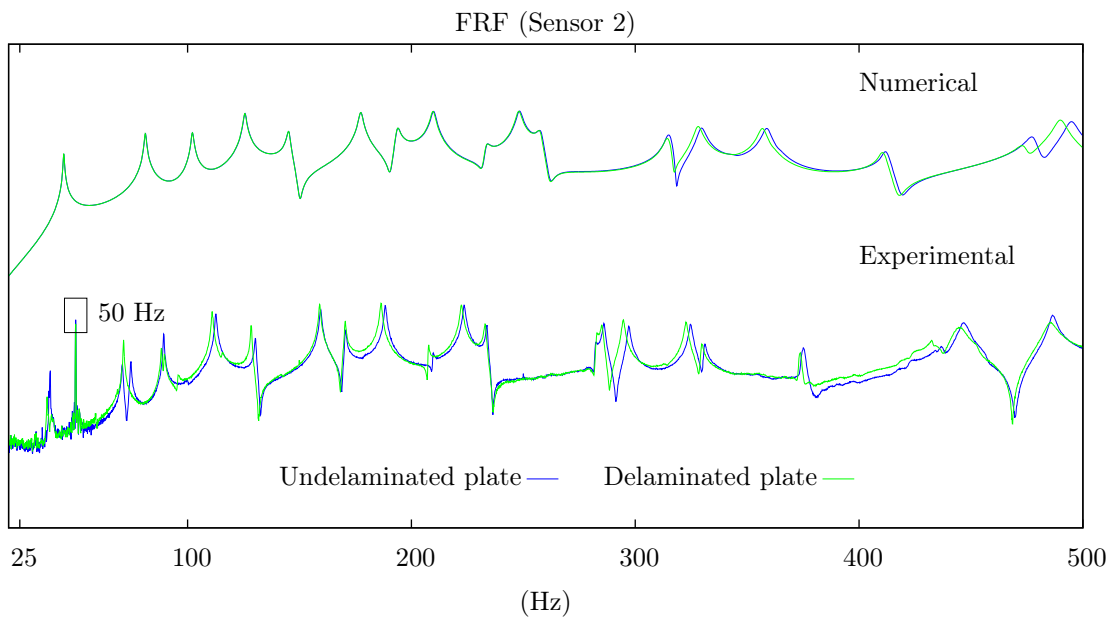


Figure 4.12: Numerical and experimental comparison for undelaminated and 80x80 mm delamination plates over the bandwidth [0 500] Hz.

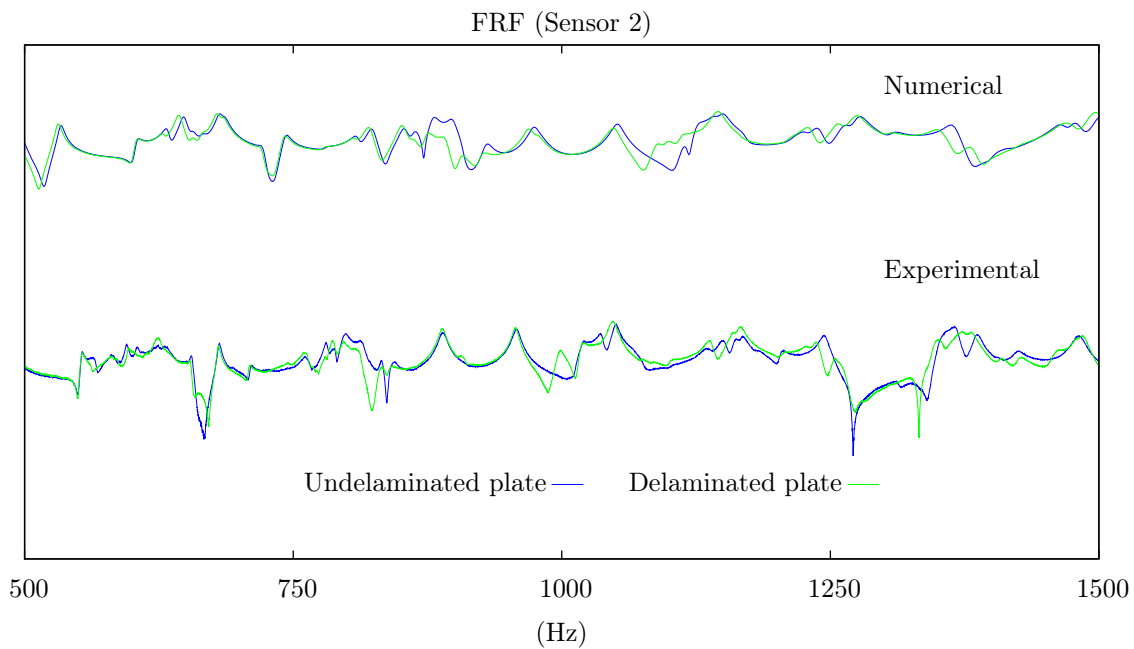


Figure 4.13: Numerical and experimental comparison for undelaminated and 80x80 mm delamination plates over the bandwidth [500 1500] Hz.

A peak in the frequency 50 Hz (and multiples for low frequencies) can be appreciated in the experimental results. This is due to the electric signal and therefore must not be taken into account, since it is not corresponding to any eigenfrequency of the plate.

Secondly the effects delamination of 180x180 mm are compared in Figures 4.15-4.17. For this case the delamination is easily identifiable from frequency shifts and amplitude changes. Similar results for numerical and experimental results were found, although not for all the natural frequencies happens the same. Higher differences were founded, specially in the first bandwidth [0 500] Hz for the numerical

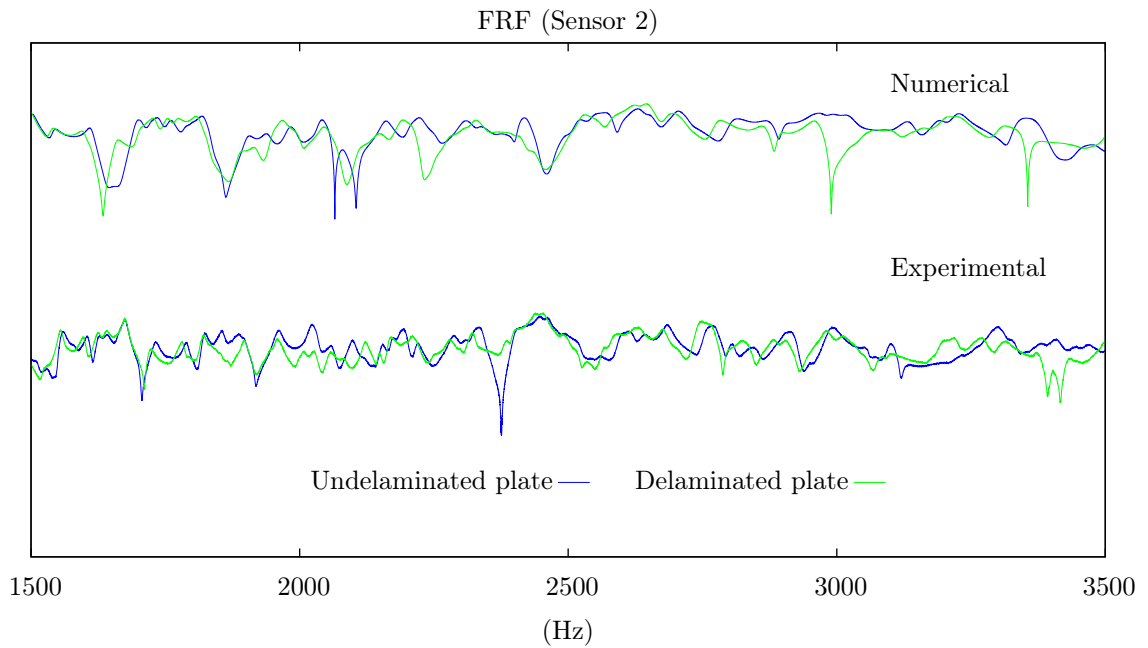


Figure 4.14: Numerical and experimental comparison for undelaminated and 80x80 mm delamination plates over the bandwidth [1500 3500] Hz.

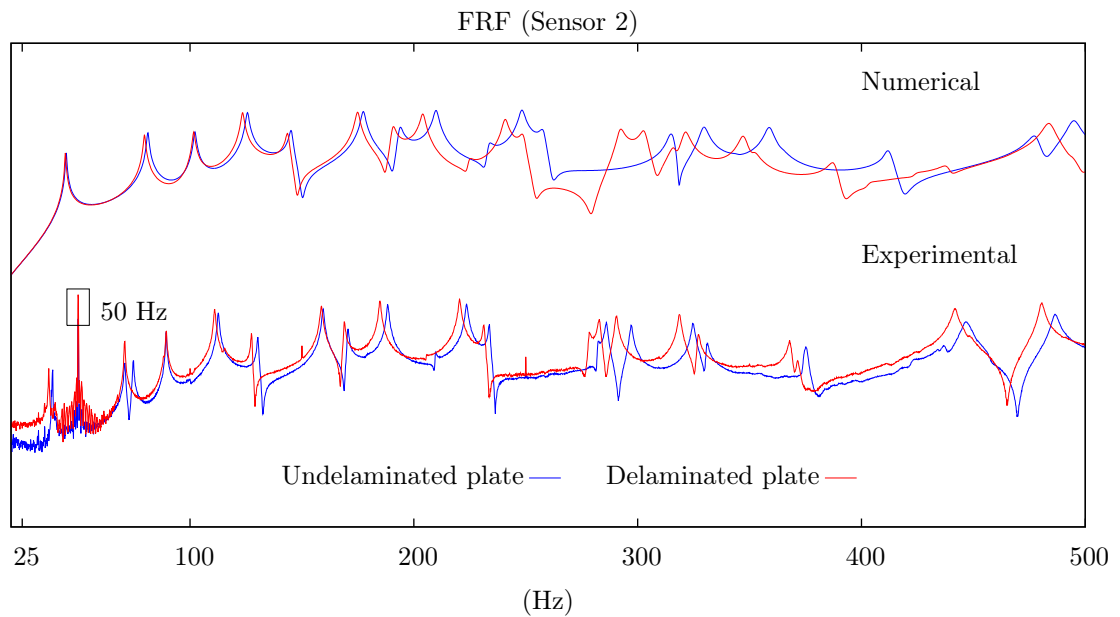


Figure 4.15: Numerical and experimental comparison for undelaminated and 180x180 mm delamination plates over the bandwidth [0 500] Hz.

one (most likely due to the delamination model does not consider any possibility of contact or friction between the debonded surfaces). However, in general the relative changes between numerical and experimental FRF's are similar from a qualitative point of view.

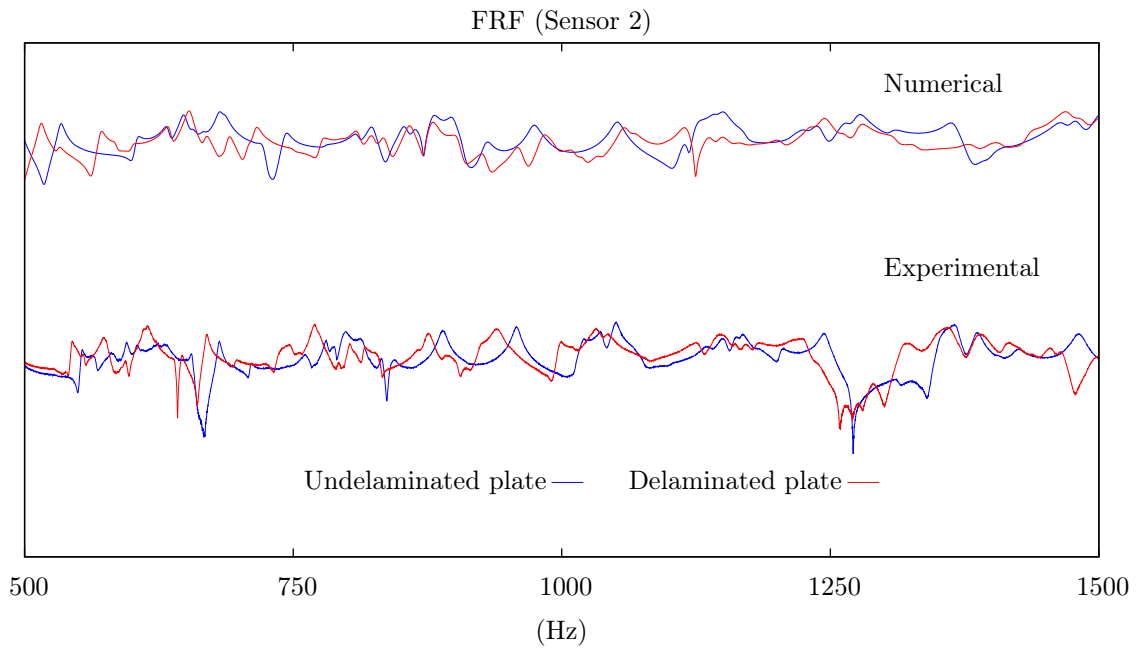


Figure 4.16: Numerical and experimental comparison for undelaminated and 180x180 mm delamination plates over the bandwidth [500 1500] Hz.

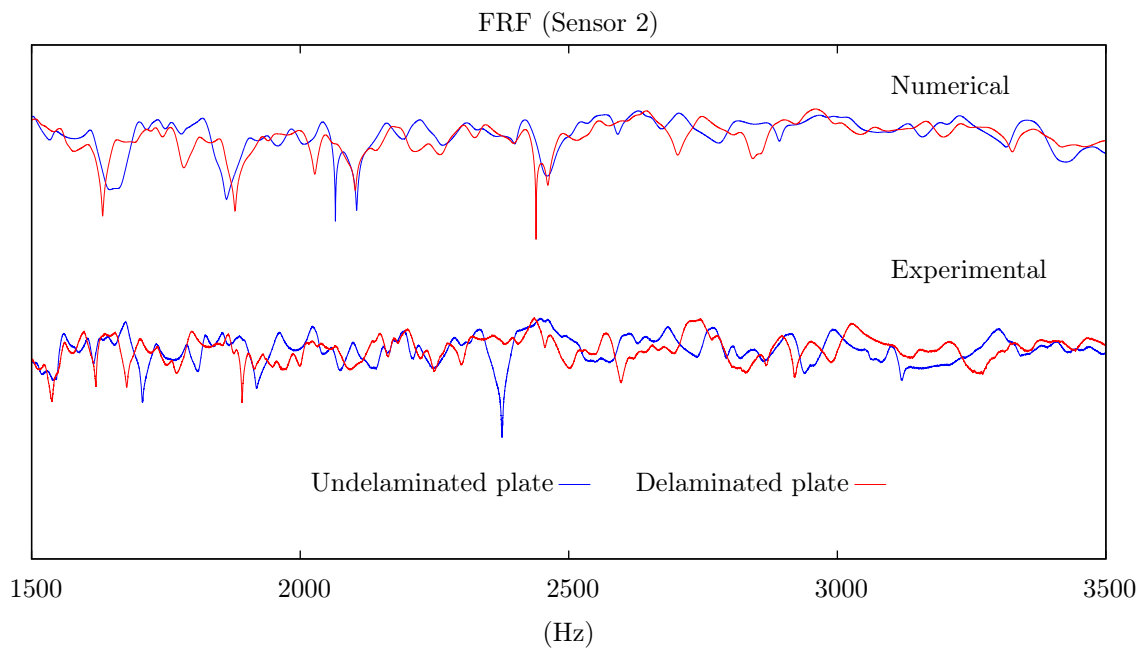


Figure 4.17: Numerical and experimental comparison for undelaminated and 180x180 mm delamination plates over the bandwidth [1500 3500] Hz.

4.6.2 Comparison with the inverse optimized parameters

It was also found that if some elastic and geometric parameters are modified, a better approach between theoretical and experimental results could be obtained. Since the ply thickness and E_x moduli are the most sensitive parameters [3], an inverse optimization procedure was performed in order to have a better approach between simulation and experimental results. It has to be kept in mind that this problem has multiple solutions and that the solution may give some unrealistic solutions from a physical point of view. However, for the purposes of this work an approach was performed taken into account the bandwidth [0 500] Hz. In this case a ply thickness of 0.2 mm and an elastic moduli $E_x=100$ GPa were used. Figure 4.18 shows the numerical eigenfrequencies in the bandwidth [0 500] Hz after being fitted. Figure 4.19 shows both FRF's. The correlation between them is 0.9998. Table 4.2 presents both natural frequencies and their respective differences.

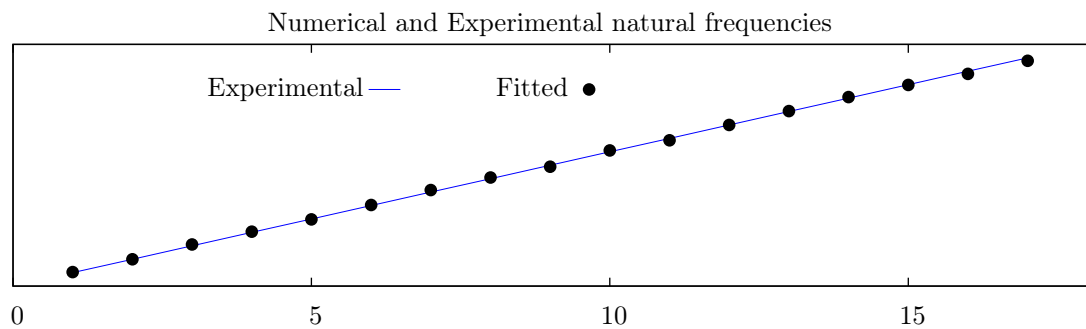


Figure 4.18: Numerical fitted frequencies at the frequency band [0 500] Hz. First 17 eigenfrequencies.

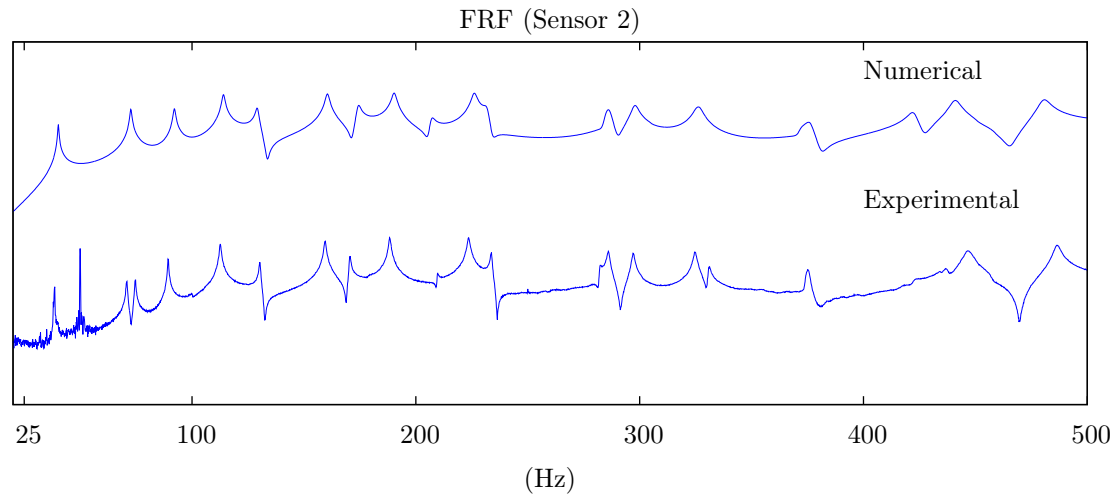


Figure 4.19: Experimental and numerical FRF over the bandwidth [0 500] Hz.

After optimization, numerical and experimental FRF's are presented again in Figures 4.20-4.24 having them a more similar behaviour. Another result to be aware of is that numerical solutions tend also to be more inaccurate as the frequency increases, since the FEM model requires a more refined mesh in order to study very high frequencies. In this study about 300 modes were computed. For this reason bandwidths [0 500], [500 1000] and [1000 1500] are analyzed.

In order to obtain a magnitude order of the predicted frequency shifts from both analysis, theory and experiment, the most significant frequencies were compared from both FRF's, obtaining similar results. It has to be pointed out that not all the frequency the shifts were so similar, although an

Mode	Exp. Natural Freq. (Hz)	Num. Natural Freq. (Hz)	Difference (Hz)
1	38.5	40.25	1.75
2	72.6	72.6	0
3	89.2	92.2	3
4	112.5	113.9	1.4
5	130.2	129.2	-1
6	159.6	160.7	1.1
7	170.5	174.3	3.8
8	188.4	190.4	2
9	209.8	207.2	-2.6
10	223.5	225.8	2.3
11	233.8	230.8	-3
12	285.9	285.8	-0.1
13	297.1	297.9	0.8
14	324.8	326.6	1.8
15	375.4	375	-0.4
16	446.6	441.2	-5.4
17	486.5	480.2	-6.3

Table 4.2: Experimental and numerical natural frequencies with the optimized parameters.

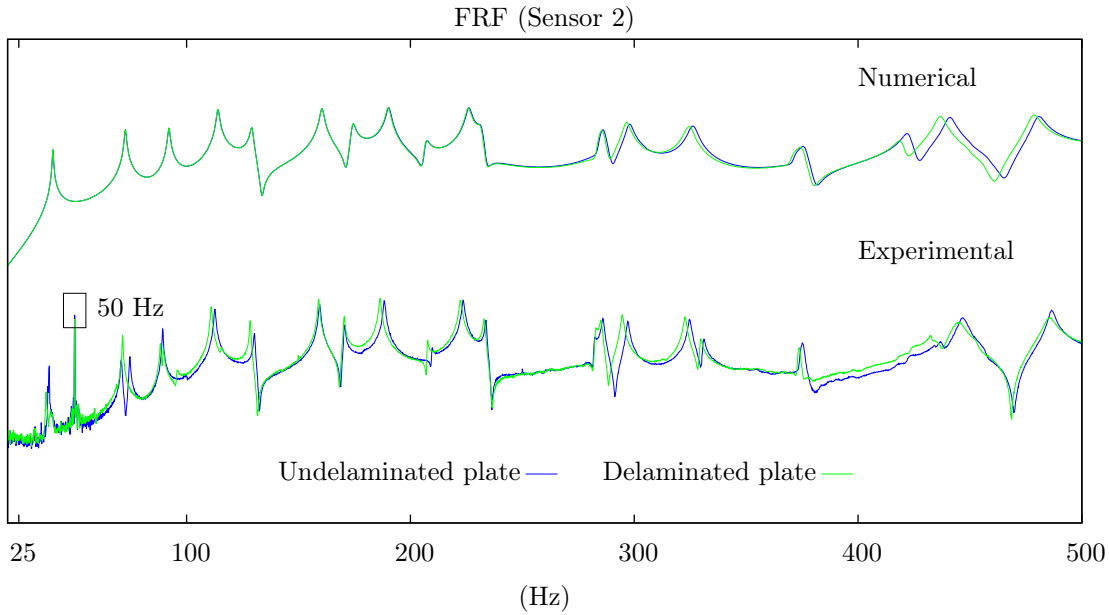


Figure 4.20: Numerical and experimental comparison for undelaminated and 80x80 mm delamination plates over the bandwidth [0 500] Hz.

acceptable general similar behaviour was observed. It also has to be kept in mind that the experimental error was fixed in a range of 1-5 Hz, increasing with the frequency.

As it was suggested in the previous subsection, contact and friction effects were not considered in the FEM models. This would explain why the numerical solution is more flexible than the experimental one, specially for the 180x180mm delamination. Although contact and friction effects should increase with the frequency, the fact that real amplitudes are almost neglectable from above the first modes (almost the total amount of energy is absorbed by the first modes) it makes that this effect tend to diminish as the frequency does. This is in agreement with the numerical and experimental results.

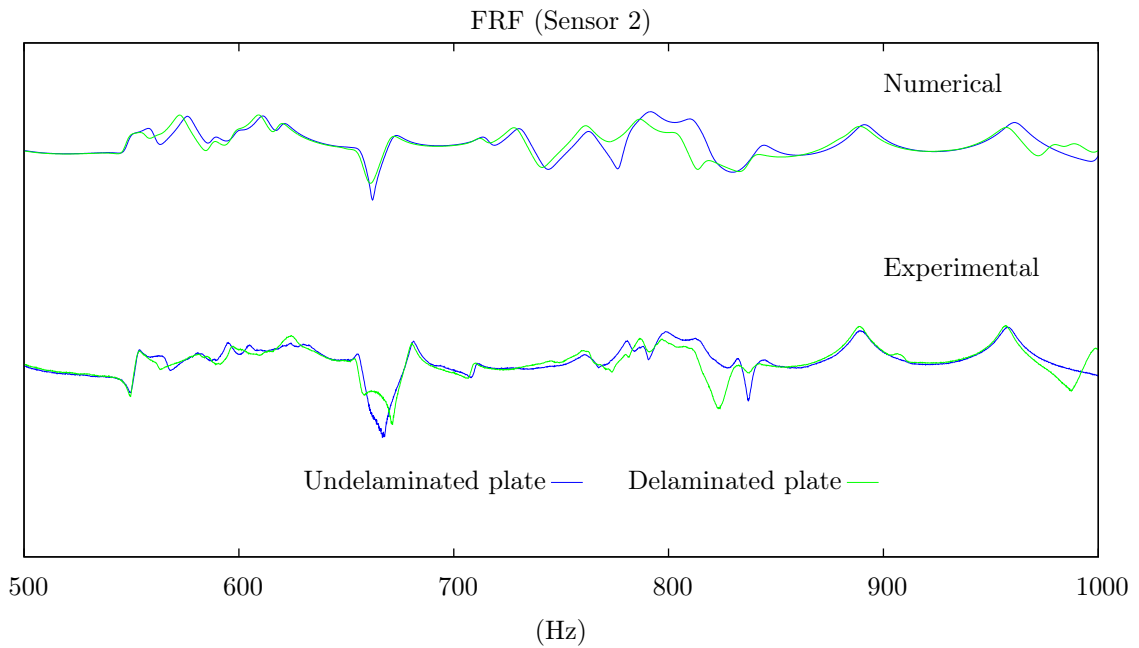


Figure 4.21: Numerical and experimental comparison for undelaminated and 80x80 mm delamination plates over the bandwidth [500 1000] Hz.

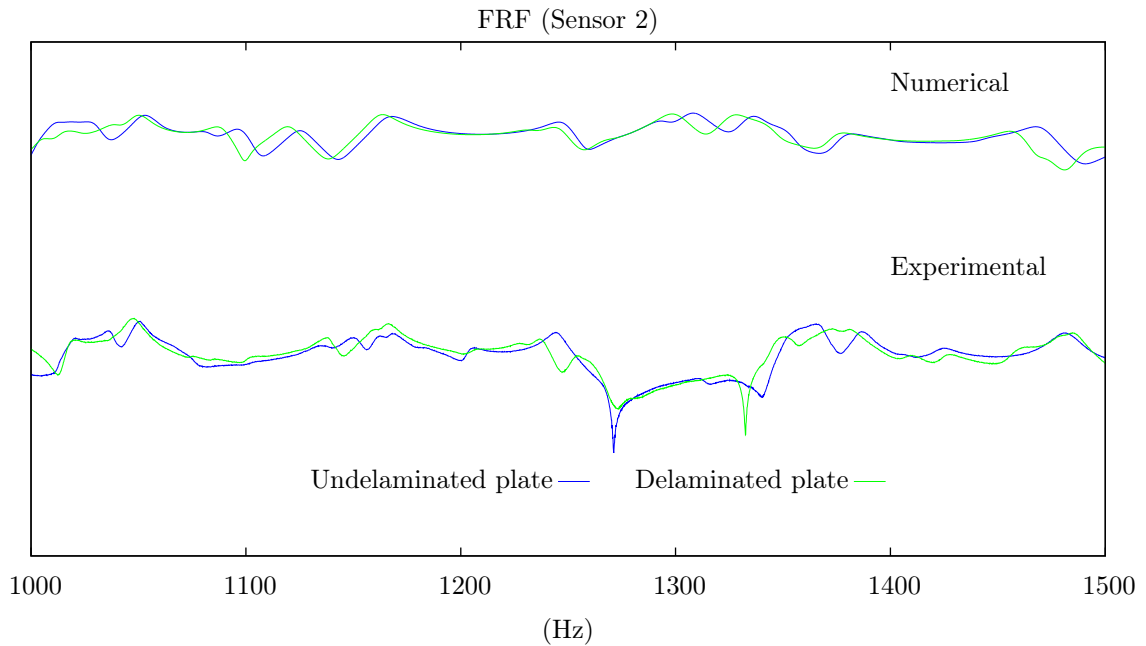


Figure 4.22: Numerical and experimental comparison for undelaminated and 80x80 mm delamination plates over the bandwidth [1000 1500] Hz.

Finally, for both numerical analysis, that is, with the given parameters of the plates and fitted ones (E_x and ply thickness) frequency shifts were compared, giving them both similar results.

Table 4.3 summarizes the frequency shifts due to the delamination obtained from the experiments and the ones obtained from the numerical analysis:

As it can be seen, they are in good agreement, despite the limitations previously mentioned.

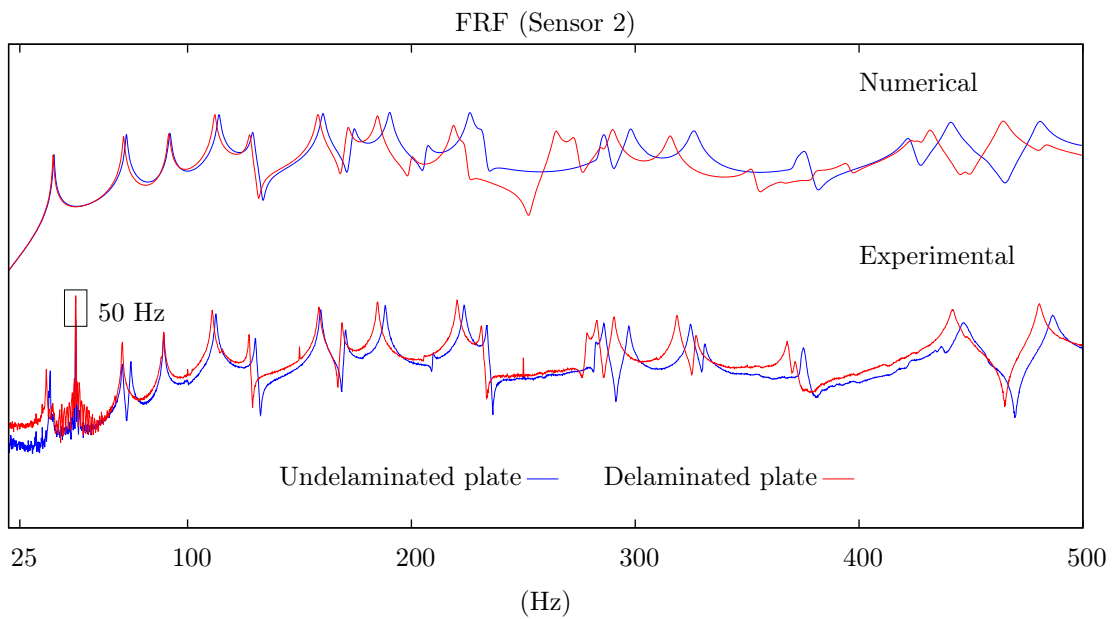


Figure 4.23: Numerical and experimental comparison for undelaminated and 180x180 mm delamination plates over the bandwidth [0 500] Hz.

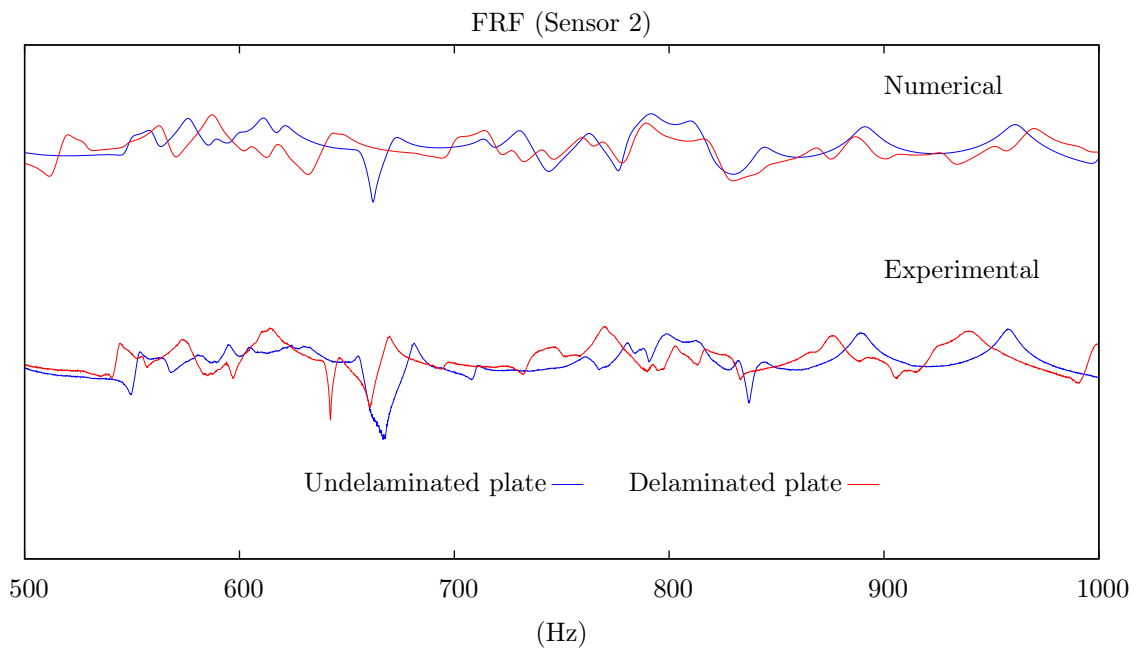


Figure 4.24: Numerical and experimental comparison for undelaminated and 180x180 mm delamination plates over the bandwidth [500 1000] Hz.

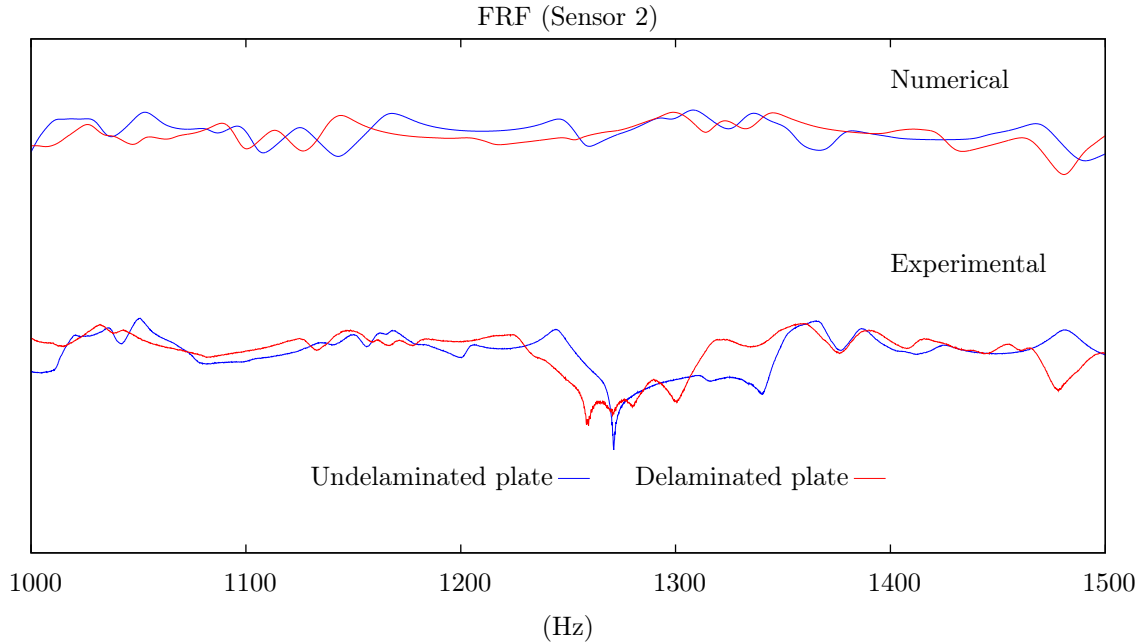


Figure 4.25: Numerical and experimental comparison for undelaminated and 180x180 mm delamination plates over the bandwidth [1000 1500] Hz.

	Experimental Shifts		Numerical Shifts	
	80x80 mm	180x180 mm	80x80 mm	180x180 mm
[0 500] Hz	1-3 Hz	<10 Hz	1-3 Hz	<20 Hz
[500 1000] Hz	<10 Hz	<20 Hz	<10 Hz	<25 Hz
[1000 1500] Hz	<10 Hz	<20 Hz	<10 Hz	<25 Hz
[1500 3500] Hz	<25 Hz	<40 Hz	-	-

Table 4.3: Most significant frequency shifts due to delamination for experimental and numerical (optimized) analysis.

4.7 General conclusions

In this chapter experiments on three composites plates, two of them with an internal delamination of different size were studied. Effectiveness of FRF analysis in order to identify the presence of delamination was performed. Results were also studied and compared with a numerical model.

The following conclusions can be pointed out, some of them well known in the SHM field:

- The experimental setup does not introduce variability (it is close to zero).
- The use of three different plates, and the use different PZT sensors with different amount of glue on each plate and the support system result in a variability of 1-5 Hz for the frequencies.
- It was difficult to set a regular variance for amplitudes in the FRF's. However noticeable changes in them can also identify damage.
- Delamination is identifiable through FRF analysis, and it is a matter of increasing the bandwidth to work with, to be able to detect small delaminations.
- No contact and friction effects have been considered in the numerical solution, obtaining greater frequency shifts due to delamination specially for the 180x180 mm delamination, and in the first analyzed bandwidth [0 500] Hz.

- Numerical results point out similar frequency shifts due to delamination.
- Model based methods should be used in a comprehensive way for damage detection techniques.
- FRF analysis and the very promising optical fibers sensors could be an effective way to identify delaminations in SHM context of real structures.

Chapter 5

Modal Analysis of Delaminated Composite Plates using the Finite Element Method and Damage Detection via combined Ritz/2d-Wavelet Analysis

In this chapter the following paper is presented: “Modal Analysis of Delaminated Composite Plates using the Finite Element Method and Damage Detection via combined Ritz/2d-Wavelet Analysis” published in the Journal of Sound and Vibration. in 2013, with doi: <http://dx.doi.org//10.1098/rsta.2000.0717>. The contribution of the author was providing some FRF analysis of the delaminated element developed in chapter 3. Some eigenvalues results for delaminated plates were also provided in order to test a damage detection technique, from a theoretical point of view.

Abstract

Structural studies to find defects (in particular delaminations) in composite plates have been very prevalent in the Structural Health Monitoring field. The present work develops a new method to detect delaminations in CFRP (Carbon Fiber Reinforced Polymer) plates. In this paper the method is validated with numerical simulations, which come to support its adequacy for use with real acquisition data. This is done firstly through the implementation of a delaminated plate finite element. Using the classical lamination plate theory, delamination is considered in the kinematic equations through jump functions and additional degrees of freedom. The element allows the introduction of n_d delaminations through its thickness. Classical QMITC (Quadrilateral Mixed Interpolation Tensorial Components) and DKQ (Discrete Kirchhoff Quadrilateral) elements are used for the membrane and bending FEM (Finite Element Method) formulation. Second, using the vibration modes obtained with the FEM, a damage location technique based on the variational Ritz method and Wavelet Analysis is proposed. The approach has the advantage of requiring only damaged modes and not the healthy ones. Both FEM simulations and Ritz/Wavelet damage detection schemes are applied in an orthotropic CFRP plate with the stacking sequence $[0/90]_{3S}$. In addition, the influence of delamination thickness position, boundary conditions and added noise (in order to simulate experimental measures) was studied.

Keywords : Delamination; FEM; Structural Health Monitoring; Damage detection; Ritz method; Wavelet Analysis

5.1 Introduction

The use of CFRP (Carbon Fiber Reinforced Polymer) has grown in recent decades by virtue of its properties. Having started within the aerospace industry, it is now widely used in other engineering applications. From the structural point of view, its stiffness, weight, fatigue-life and strength limit make this material very attractive.

Delamination or debonding of adjoining plies is one of the most frequent types of damage in composite structures. It must be taken into account, because its presence modifies the carrying capacity of the structure. It may originate in manufacturing itself, or during service-life due to fatigue or impact. Because delamination is difficult to detect, in recent years several research lines have aimed to develop efficient methods for its detection. Model based methods [33] have been developed to avoid, when possible, the in-situ inspection of a structure, since they can provide information about the presence of damage based on the combination of a measured response and a numerical model.

A review of the models developed to investigate delamination can be found in Ref. [33] and more recently in Ref. [57]. The present paper classifies the delamination models in view of the laminate composite theory used and the damage model.

The main laminate composite theories, derived from the general elasticity theory, are:

- Equivalent Single Layer models;
- Layerwise models;
- 3D models.

The first of these were based on the so-called Equivalent Single Layer theory (ESL), resulting in the Classical Laminate Theory (CLT) for thin plates, First-Order Shear Deformation Theory (FSDT) for thick plates and Higher Order Theories (HOT) as a generalised ESL theory. The need to focus interest on the layer level, in order to study interply stresses, led to Layerwise theories (see Ref. [3]). Full Layerwise theories have a layer-by-layer piecewise approximation, whereas the partial Layerwise theories (zig-zag) are a particular case of an ESL with continuity in the interply stresses, offering a good balance between accuracy and time-consumption. Finally, for some applications the problem can be solved using the standard 3D theory of elasticity, but it is very time-consuming and normally used for certain local problems.

It is important to stress that only static conditions of delamination (a constant size over time) are considered in this paper, since the purpose is to detect an existing delamination through an FEM model, which is supposed to be of certain dimensions. However, other models based on 3D elasticity [71, 72] and Interface Elements [73] have been applied to study the progression of delamination.

From the perspective of damage, two possibilities can be applied:

- “4 Region Approach”;
- Considering the delamination in the equations of the problem.

In most models, delamination is taken into account using the so-called “4 Region Approach” (see Refs. [33, 57]). This assumption physically separates the model into four different elements that are connected properly at the nodes. The other way to consider delamination is in the equations of the problem; then, properly defining new kinematic equations, the delamination can be modeled.

Different authors have approached this technique through the use of jump functions with a Heaviside function. New degrees of freedom appear as a result of this assumption.

In recent years similar delamination models have been described. Reference [59] studies the buckling in composite cylindrical shells under axial compression through the “4 Region Approach”. Reference [74]

studies the buckling of composite shells with multiple delaminations based on a higher order zig-zag theory that includes the delamination in the kinematic equations. Reference [75] studies the vibration of shells using the “4 Region Approach”.

Concerning the interaction between the two delaminated surfaces, contact forces were not taken into account since they would be negligible for the lower modes and delamination sizes considered in this paper (the opening is around 10^{-13} times the maximum displacement of the considered mode). Some previous research [56, 44] addresses this issue in the case of composite beams. These studies concluded that contact forces modify the response only for delamination sizes larger than 10%-30% of the beam. In the case of plates, owing to the 2D behaviour, the influence of contact would be even smaller than in beams. We should stress that only lower modes were considered in this paper, for which reason such influence is virtually negligible.

As is well known, delamination produces changes in the structural properties, and in particular the dynamic ones. Because stiffness and damping are modified (decrease and increase, respectively), several dynamic parameters such as frequency, mode shape, damping ratio, etc. can be studied in order to detect the delamination location and extent. Many of the damage detection methods involve vibration test techniques that are based on the assumption that damage modifies the physical characteristics of the material. Because the natural frequencies and vibration modes change substantially with respect to the undamaged material, they can be used to develop approaches for damage detection and evaluation. The reader can find most of the damage detection techniques in [34, 35, 76].

On the other hand, Wavelet Analysis has been widely used to detect damage both in beams and plates (see e.g. Refs. [77, 78, 79, 80, 81, 82]). It generally calls for modal information regarding the healthy structure, which may not be available in some practical situations. In contrast, some papers (see Refs. [78, 79]) have proven the effectiveness of the use of new wavelet approaches to develop damage indexes in which the modal information of the undamaged structure is not needed. Such approaches, applied to beams, are based on the use of the Wavelet Transform to approximation functions of the damaged modes as well as the undamaged ones.

In this context, we propose a new damage location index based on the combined use of the 2D Continuous Wavelet Transform (CWT) and the variational Ritz method on the damaged modes (the application of the Ritz method to damaged plates is developed in works such as Refs. [83, 84, 85, 86]). The transversal displacement modes of the damaged plate are approximated by a product series of functions compatible with the boundary conditions as under the classical Ritz method work [87], generating new modes to be used as undamaged modes. The damage index is thus defined as the difference between the CWT of the damaged modes and the new ones.

The damage detection approach put forth here has been tested with an orthotropic CFRP plate with stacking sequence $[0/90]_{3S}$ in which six extensions of delamination –at the same position but with different extension– were generated via the FEM simulation proposed. The six extensions were thickness-localised in the midplane, and for one case the influence of the thickness position was studied. The approach makes it possible to reach Level 2 of SHM, i.e. as far as the location of damage.

5.2 Delamination model

5.2.1 Kinematic delamination equations

One relevant aspect of this paper is the effect of the delamination size on mode shapes, with detectability achieved through the Wavelet Transform. For this purpose, an ESL finite element based

on CLT was developed. Delamination was considered through kinematic equations which, according to Ref. [56], can be written as:

$$\begin{aligned}
 u(x, y, z) &= u_0(x, y) + \theta_{y0}(x, y)z + \sum_{r=1}^{n_d} \left[u_r(x, y) + \theta_{yr}(x, y)z \right] H(z - z_r) \\
 v(x, y, z) &= v_0(x, y) + \theta_{x0}(x, y)z + \sum_{r=1}^{n_d} \left[v_r(x, y) + \theta_{xr}(x, y)z \right] H(z - z_r) \\
 w(x, y, z) &= w_0(x, y) + \sum_{r=1}^{n_d} \left[w_r(x, y) H(z - z_r) \right]
 \end{aligned} \tag{5.1}$$

where u , v , and w are displacements; θ_x and θ_y are rotations; H is the Heaviside step function; the subscript 0 indicates midplane quantities of the lower delaminated subsection. Variables with subscript r are the new degrees of freedom describing the kinematic discontinuities across the r -th delamination. These new variables represent relative displacements and rotations between plies; n_d is the number of delaminations considered.

Figure 5.1 shows the kinematics of the r -th delamination at the ply level.

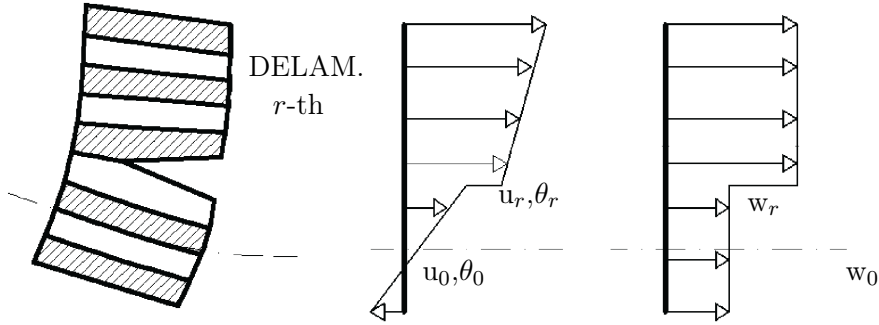


Figure 5.1: Kinematics of delamination [56]

The CLT of an undelaminated plate relates internal forces/moments \mathbf{N}_0 and \mathbf{M}_0 with in-plane strains, $\boldsymbol{\epsilon}_0$ and $\boldsymbol{\kappa}_0$:

$$\begin{Bmatrix} \mathbf{N}_0 \\ \mathbf{M}_0 \end{Bmatrix} = \begin{bmatrix} \mathbf{A} & \mathbf{B} \\ \mathbf{B} & \mathbf{D} \end{bmatrix} \begin{Bmatrix} \boldsymbol{\epsilon}_0 \\ \boldsymbol{\kappa}_0 \end{Bmatrix} \tag{5.2}$$

where:

$$\mathbf{N}_0 = \begin{Bmatrix} N_x \\ N_y \\ N_{xy} \end{Bmatrix}, \quad \mathbf{M}_0 = \begin{Bmatrix} M_x \\ M_y \\ M_{xy} \end{Bmatrix}, \quad \boldsymbol{\epsilon}_0 = \begin{Bmatrix} \epsilon_{x0} \\ \epsilon_{y0} \\ \epsilon_{xy0} \end{Bmatrix}, \quad \boldsymbol{\kappa}_0 = \begin{Bmatrix} \kappa_{x0} \\ \kappa_{y0} \\ \kappa_{xy0} \end{Bmatrix} \tag{5.3}$$

\mathbf{A} is the membrane stiffness matrix, \mathbf{D} the bending stiffness matrix and \mathbf{B} the coupling matrix, all of them with reference to the laminate midplane.

Using the kinematic equations (5.1), an analogue to Eq. (5.2) can be obtained for a laminate with n_d delaminations:

$$\begin{pmatrix} \mathbf{N}_0 \\ \mathbf{N}_1 \\ \vdots \\ \mathbf{N}_{n_d} \\ \mathbf{M}_0 \\ \mathbf{M}_1 \\ \vdots \\ \mathbf{M}_{n_d} \end{pmatrix} = \begin{bmatrix} \mathbf{A} & \mathbf{A}_1 & \dots & \mathbf{A}_{n_d} & \mathbf{B} & \mathbf{B}_1 & \dots & \mathbf{B}_{n_d} \\ \mathbf{A}_1 & \mathbf{A}_{11} & \dots & \mathbf{A}_{1n_d} & \mathbf{B}_1 & \mathbf{B}_{11} & \dots & \mathbf{B}_{1n_d} \\ \vdots & \vdots & \dots & \vdots & \vdots & \vdots & \dots & \vdots \\ \mathbf{A}_{n_d} & \mathbf{A}_{1n_d} & \dots & \mathbf{A}_{n_d} & \mathbf{B}_{n_d} & \mathbf{B}_{1n_d} & \dots & \mathbf{B}_{n_d} \\ \mathbf{B} & \mathbf{B}_1 & \dots & \mathbf{B}_{n_d} & \mathbf{D} & \mathbf{D}_1 & \dots & \mathbf{D}_{n_d} \\ \mathbf{B}_1 & \mathbf{B}_{11} & \dots & \mathbf{B}_{1n_d} & \mathbf{D}_1 & \mathbf{D}_{11} & \dots & \mathbf{D}_{1n_d} \\ \vdots & \vdots & \dots & \vdots & \vdots & \vdots & \dots & \vdots \\ \mathbf{B}_{n_d} & \mathbf{B}_{1n_d} & \dots & \mathbf{B}_{n_d} & \mathbf{D}_{n_d} & \mathbf{D}_{1n_d} & \dots & \mathbf{D}_{n_d} \end{bmatrix} \begin{pmatrix} \boldsymbol{\epsilon}_0 \\ \boldsymbol{\epsilon}_1 \\ \vdots \\ \boldsymbol{\epsilon}_{n_d} \\ \boldsymbol{\kappa}_0 \\ \boldsymbol{\kappa}_1 \\ \vdots \\ \boldsymbol{\kappa}_{n_d} \end{pmatrix} \quad (5.4)$$

where $\mathbf{A}_{rr} = \mathbf{A}_r$, $\mathbf{B}_{rr} = \mathbf{B}_r$ for $r = 1, 2, \dots, n_d$; \mathbf{N}_0 and \mathbf{M}_0 are the resultant internal forces and moments of the laminate section, and \mathbf{N}_r and \mathbf{M}_r the internal forces and moments of the partial section (above the r -th ply). New degrees of freedom entail new internal forces/moments and strains, i.e.

$$\mathbf{N}_0 = \int_{-h/2}^{h/2} \begin{Bmatrix} \sigma_x \\ \sigma_y \\ \tau_{xy} \end{Bmatrix} dz, \quad \mathbf{M}_0 = \int_{-h/2}^{h/2} \begin{Bmatrix} \sigma_x \\ \sigma_y \\ \tau_{xy} \end{Bmatrix} z dz \quad (5.5)$$

$$\mathbf{N}_r = \int_{-h/2}^{h/2} \begin{Bmatrix} \sigma_x \\ \sigma_y \\ \tau_{xy} \end{Bmatrix} H(z - z_r) dz, \quad \mathbf{M}_r = \int_{-h/2}^{h/2} \begin{Bmatrix} \sigma_x \\ \sigma_y \\ \tau_{xy} \end{Bmatrix} z H(z - z_r) dz \quad (5.6)$$

$$\mathbf{A}_r = \sum_{p=1}^n \int_{-z_p}^{z_p} \bar{\mathbf{Q}}_p H(z - z_r) dz, \quad \mathbf{B}_r = \sum_{p=1}^n \int_{-z_p}^{z_p} \bar{\mathbf{Q}}_p z H(z - z_r) dz \quad (5.7)$$

$$\mathbf{D}_r = \sum_{p=1}^n \int_{-z_p}^{z_p} \bar{\mathbf{Q}}_p z^2 H(z - z_r) dz, \quad \mathbf{A}_{rs} = \sum_{p=1}^n \int_{-z_p}^{z_p} \bar{\mathbf{Q}}_p H(z - z_r) H(z - z_s) dz \quad (5.8)$$

$$\mathbf{B}_{rs} = \sum_{p=1}^n \int_{-z_p}^{z_p} \bar{\mathbf{Q}}_p z H(z - z_r) H(z - z_s) dz \quad (5.9)$$

$$\mathbf{D}_{rs} = \sum_{p=1}^n \int_{-z_p}^{z_p} \bar{\mathbf{Q}}_p z^2 H(z - z_r) H(z - z_s) dz \quad (5.10)$$

where n is the number of plies and $\bar{\mathbf{Q}}_p$ is the reduced stiffness of the p -th ply.

5.2.2 FEM Formulation

The formulation presented in Section 5.2.1 was used to develop a delaminated Finite Element. These new degrees of freedom represent the relative displacements in the delamination. The element allows n_d delamination in its thickness. For the purpose of this paper only one delamination was considered, resulting in a 4-node quadrilateral element, with 10 d.o.f. per node, five of them being the new degrees of freedom associated with the delamination.

The element requires $2 \cdot n_d$ deformation matrices in order to interpolate ϵ_r and κ_r . Since these strains have the same structure as ϵ_0 and κ_0 , the element can be built using only two single finite element formulations, each one applied to the extensional (sliding) and bending (opening and relative rotation) d.o.f. of the r delamination. One is the membrane formulation, modeled using the QMITC (Quadrilateral Mixed Interpolation Tensorial Components) element [65], and the other is the bending formulation, modeled with the DKQ (Discrete Kirchhoff Quadrilateral) element [66].

5.3 Semianalytical solution for the plate modes

The Ritz method [87] is a semianalytical method used to calculate frequencies and modes of vibration of a plate. It is based on the calculation of the potential energy U and the kinetic energy T . The method supposes that the transversal displacement w can be expressed as a function product series with the corresponding function weights, i.e.

$$w(x, y) = \sum_{m=1}^M \sum_{n=1}^N A_{mn} X_m(x) Y_n(y) \quad (5.11)$$

where A_{mn} are the function weights, M and N are the summation number of terms (usually $M = N$) and $X_m(x)$, $Y_n(y)$ are functions that satisfy the boundary conditions at $x = (0, a)$ and $y = (0, b)$. In this work, the boundary condition compatible functions described in Ref. [88] are used.

To obtain the vibration modes of the plate, $U - T$ must be minimised, i.e.

$$\frac{\partial(U - T)}{\partial A_{mn}} = 0 \quad (5.12)$$

Using Eq. (5.12) with all A_{mn} parameters, a set of $M \cdot N$ equations is obtained, expressed in matrix form as

$$\{\mathbf{F} - \mathbf{G}\omega^2\} \mathbf{A}_{mn} = 0 \quad (5.13)$$

where \mathbf{F} and \mathbf{G} are $M \cdot N$ side square matrices, ω the angular frequency and \mathbf{A}_{mn} is the vector of the variables. Multiplying the left side by \mathbf{G}^{-1} and denoting $\mathbf{H} = \mathbf{G}^{-1}\mathbf{F}$ and $\lambda = \omega^2$, Eq. (5.13) becomes

$$\{\mathbf{H} - \mathbf{I}\lambda\} \mathbf{A}_{mn} = 0 \quad (5.14)$$

where \mathbf{I} is the $M \cdot N$ side square identity matrix. Since Eq. (5.14) is a set of homogeneous equations, nontrivial solutions can be obtained only if the determinant of the coefficient matrix is zero, i.e.

$$|\mathbf{H} - \mathbf{I}\lambda| = 0 \quad (5.15)$$

Hence, an eigenvalue problem must be solved. Because matrix dimensions are usually large, the computation of the matrix terms and the solution of the eigenvalue problem are usually obtained using a computer program. In other words, this is a semianalytical method.

This method allows one to obtain the frequencies (from the eigenvalues, which are the square of the angular frequencies) and the modes (from the eigenvectors, which are the weights A_{mn} for each mode in Eq. (5.11)).

5.4 Damage detection

The technique proposed in this work allows for damage detection to be performed at Level 1 (detection) and Level 2 (location) of Rytter's damage identification hierarchy [89]. It is remarkable that no information about the undamaged plate is necessary, meaning great applicability. The technique is based on Wavelet Transform combined with the Ritz method. Figure 5.2 shows a block diagram of the complete damage detection technique. The main advantage of the current method is that it does not require information on the undamaged plate or higher modes to detect damage.

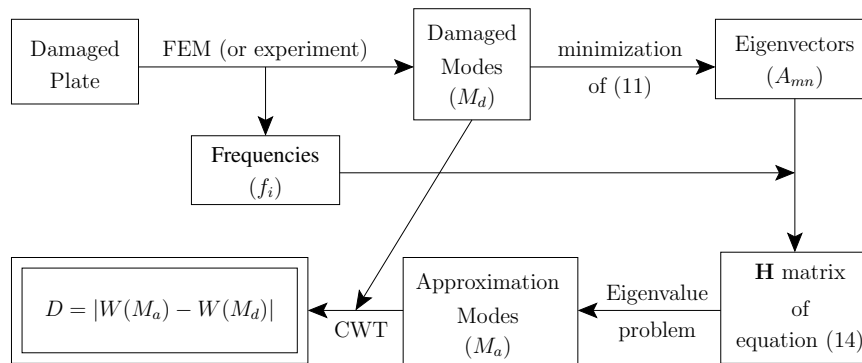


Figure 5.2: Block diagram for damage detection based on Ritz method and Wavelet Transform.

Firstly, the first four (main) frequencies (f_i) and vibration modes of the damaged plate (M_d) are obtained using the FEM research code FEAP with the element and mesh described in Section 5.2 (85×65 elements, 86×66 nodes).

Second, using the summation in Eq. (5.11) and assuming a set of functions compatible with the boundary conditions as in Ref. [88], the values A_{mn} that fit the numerical modes are computed using the Fletcher-Reeves conjugate gradient minimization algorithm [90].

From the eigenvectors A_{mn} and the frequencies (f_i), an approximation of the matrix \mathbf{H} of Eq. (5.14) is obtained.

This matrix is an approximation of the \mathbf{H} matrix that can be obtained using the Ritz method with $M = N = 2$ in Eq. (5.11). Thus, a standard extraction algorithm is used to obtain the frequencies and vibration modes (M_a). These new vibration modes are an approximation of the original ones, since only four terms in Eq. (5.11) were used, implying that some information is lost during the process. The technique presented here assumes that this lost information is mainly related to damage, so these new modes can therefore be used as the undamaged modes to define a damage index similar to Ref. [77]. Note that different values for M and N can be used by changing the number of frequencies and modes established initially.

Finally, to detect the presence of damage, the following positional damage index is defined at all the points of the mesh (86×66 nodes):

$$D(x, y) = |W(M_a(x, y)) - W(M_d(x, y))| \quad (5.16)$$

where $W(X)$ represents the 2D Continuous Wavelet Transform. In order to perform a good comparison, the modes have to be normalised in the same way. In this case a normalization to the maximum absolute value is applied.

The chosen wavelet function was the Halo Wavelet, also known as isotropic Morlet Wavelet, described in Ref. [91]. In the frequency domain, this wavelet can be expressed as:

$$\hat{g}(k) = \exp\left(-\frac{(|k| - k_0)^2}{2}\right) \quad (5.17)$$

where k is the frequency vector and k_0 is a parameter.

Figure 5.3 shows the Halo Wavelet in both the spatial and frequency domains. We should underline that the Halo Wavelet is always real. To satisfy the wavelet admissibility condition ($k_0 > 5.5$, see Ref. [92]), the parameter k_0 was chosen as equal to 6. Regarding the scale, it is necessary to consider that the width of the wavelet function depends on the minimum number of divisions in the axis (in our case 65, corresponding to the y axis). The optimum scales for damage detection were found to be the ones allowing placement inside the first and second peaks of a number of elements between 4 (about scale 7) and 6 (about scale 10). The scale we used was equal to 8.5. Wavelet computations were performed using Matlab® and the YAWTb toolbox [93]. We should stress that these optimum scales were independent of the size of the damage.

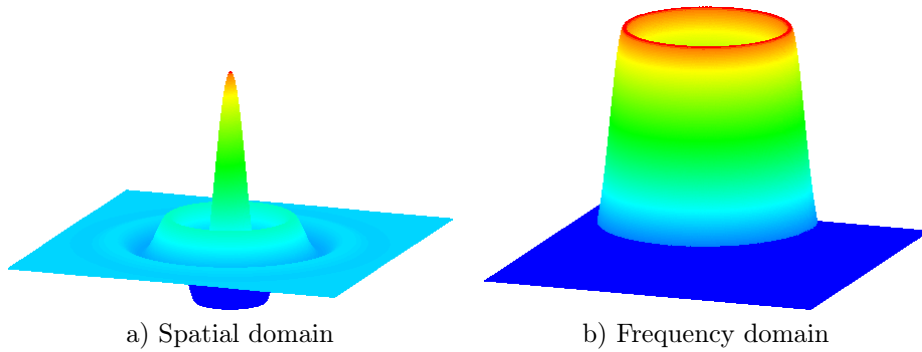


Figure 5.3: Halo Wavelet in Spatial domain (a) and Frequency domain (b).

5.5 Results

5.5.1 Cases analysed

The element explained in Section 5.2 was implemented in the Finite Element Analysis Program FEAP [67]-[28]. A composite $[0/90]_{3S}$ rectangular plate with dimensions 0.85×0.65 m, was studied and numerically simulated. Two different boundary conditions were implemented: fully clamped and fully simply supported, the plate being fully clamped if is not specified otherwise. Eight different cases of a single delamination were considered (see Table 5.1). For six of the cases, the position with respect to thickness was considered to be between the 6-th and 7-th plies (midplane delamination), and the remaining two were considered outside of the midplane (one between the 3-rd and 4-th plies, the other

between 9-th and 10-th). Its position on the plate (top view) was always centered at the coordinates $x = 57$ cm and $y = 42$ cm. Figure 5.4 shows the Finite Element Model and the location of the delamination for damage case IV. The mesh used for all the computations was 1.00 cm \times 1.00 cm. Modes 1 and 3 were used in all the cases.

For the sake of simplicity, only one delamination was considered in all the analysed cases. It is reasonable to assume that if multiple delaminations exist, damage would be greater and thus more detectable using the procedure proposed in this paper.

The mechanic properties of the ply were considered to be $E_x = 150$, $E_y = 11.5$, $G_{xy} = 5$ GPa, $\nu = 0.42$ and $\rho = 1560$ kg/m³. The ply thickness was taken to be $t_p = 0.2$ mm. They correspond to a typical CFRP plate.

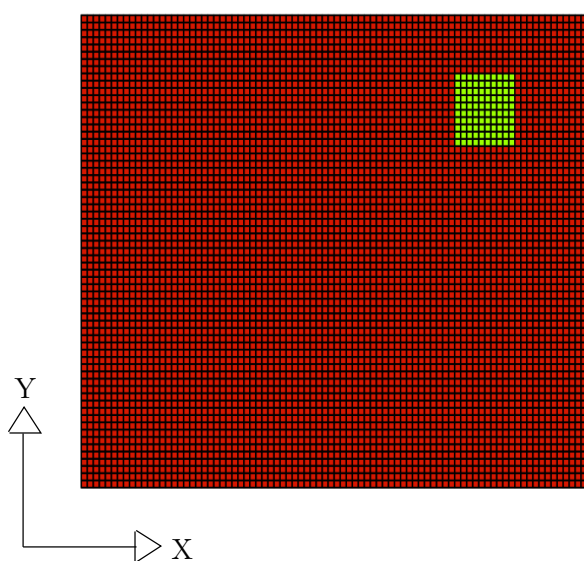


Figure 5.4: FEM Model. Case IV of damage

Before looking at the results of the new damage detection method proposed in this paper, some classical mode shapes and FRF are plotted below. The purpose is to show how this new method can detect damage, even for lower modes, using only the damaged response.

Case	Delamination size (m x m)	Plies between delamination is located
0	Undamaged	
I	0.04 x 0.04	6-th/7-th
II	0.06 x 0.06	6-th/7-th
III	0.08 x 0.08	6-th/7-th
IV	0.10 x 0.10	6-th/7-th
V	0.14 x 0.14	6-th/7-th
VI	0.18 x 0.18	6-th/7-th
VII	0.10 x 0.10	3-rd/4-th
VIII	0.10 x 0.10	9-th/10-th

Table 5.1: Cases of damage analyzed

5.5.2 Mode shapes

Mode shapes are frequently used to detect damage, which modifies their configuration, the curvatures of these mode shapes being commonly used. Figures 5.5 and 5.6 show mode shapes of x-Curvature for modes 1, 2, 4 and 6. The first Figure is for case I of damage and the second one is for case IV. As shown, curvatures are indeed able to detect damage. For small cases of damage, more modes are required, because delamination is not detectable in all of them. On the other hand, Wavelet Analysis performed on the vertical displacements is capable of detecting the presence of delamination in every mode. Vertical displacements could be easily taken as measured data from a real structure. Curvatures are computed directly as the second derivative of the measured displacements, giving, for thin plate formulations, the exact value. For Higher Order formulations a pseudo-curvature would be obtained, whose effect in damage detection techniques would be similar to that of thin formulations.

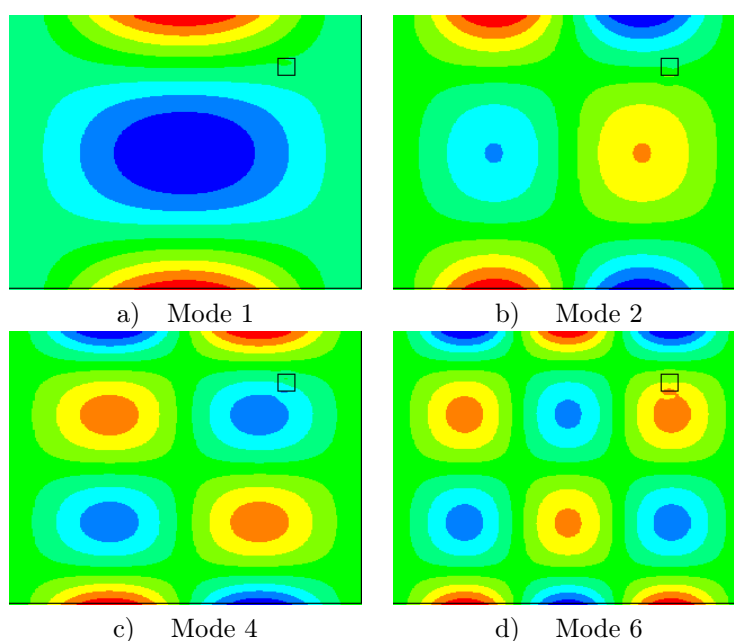


Figure 5.5: Mode shapes 1(a), 2 (b), 4 (c) and 6 (d) for x-Curvatures for a plate with case I delamination

5.5.3 FRF Analysis

Another powerful tool is Frequency Response Function (FRF) Analysis. In this case, the information is normally taken at some points of the structure. With an excitation at coordinates $x = 20$ cm and $y = 14$ cm, FRF from the different simulations at coordinates $x = 25$ cm and $y = 22$ cm (S1) and $x = 60$ cm and $y = 22$ cm (S2) were obtained. Here, the vertical displacement was the degree of freedom used.

Figure 5.7 shows the FRF at positions S1 and S2. Figures a) and c) show the undamaged case and the damaged cases I, II and III. Figures b) and d) show the undamaged case and the damaged cases IV, V and VI. Figures a) and b) are for S1, and c) and d) for S2.

From the plots, it can be seen that FRF is a very effective method for detecting delamination, requiring only the information from some points, minimizing the amount of data to be measured. However, it requires the use of higher modes and the undamaged response. Even for large delamination sizes, higher modes are required. This result confirms that delamination is a difficult kind of damage to detect, using the vibration bending modes, if the information is taken locally.

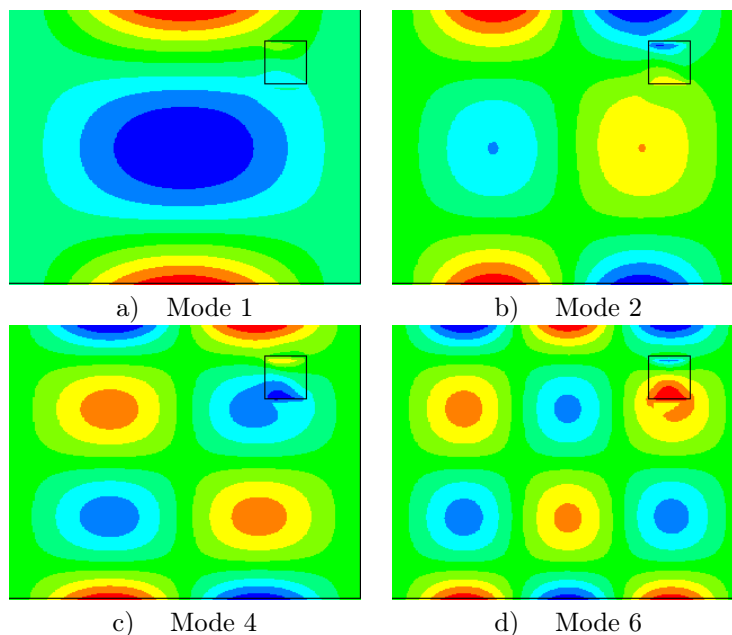


Figure 5.6: Mode shapes 1 (a), 2 (b), 4 (c) and 6 (d) for x-Curvatures for a plate with case IV delamination

5.5.4 Wavelet Analysis

Figures 5.8 and 5.9 show the positional damage index $D(x, y)$ defined in this paper, calculated for the plates with damage cases I, II, IV and VI using, respectively, mode 1 and mode 3 for computations. A square black line delimits the extension of the delamination. It is clear that the damage index D is larger near the delaminated zone, allowing for its detection. Thus D is a good indicator for damage location. Results for the two modes are very similar except for damage case VI, where mode 1 provides a better performance. Other modes were used with similar results, and other scales were used with poorer results.

It is seen that even for small delamination extensions, the delaminated zone and proximities are clearly different from the rest of the plate, using only lower modes. This is an advantage with respect to classical methods such as mode shapes or FRF Analysis. Another important advantage is the fact that this method does not call for any information about the undamaged plate, and results can be easily computed from the measured displacements.

5.5.5 Influence of the delamination thickness position

In this Section the results for damage detection in cases VII and VIII are compared with case IV. In the three cases the delamination has the same extension and it is placed between different plies, as is described in Table 5.1. Figure 5.10 shows the results of the damage index $D(x, y)$ calculated for these three cases, using modes 1 and 3. It can be seen that the method provides very similar results for delaminations with the same extension, no matter where the delamination is placed in the midplane (case IV) or away from the midplane (cases VII and VIII).

5.5.6 Influence of boundary conditions

In this Section the influence of the boundary conditions for damage detection is studied. To this end, the results for a fully clamped plate are compared with the results for a fully simply supported plate, both for the damage case IV.

Figure 5.11 shows the results of the damage index $D(x, y)$ calculated for both boundary conditions, using case IV and modes 1 and 3. It can be seen that for mode 1 the method provides very similar results. On the other hand, for mode 3 some noise appears in the corners when the plate is simply supported, but the delamination is well located despite this.

5.5.7 Effect of added noise

To study the applicability of the damage index $D(x, y)$ on experimental measures, the numerical modes M_d were modified by the addition of random noise, with the aim of simulating experimental conditions of modes. That is, the new modes, called noisy modes, were generated by the following expression for every point in the mesh:

$$\tilde{w}(x, y) = w(x, y) + R \times 10^Z \quad (5.18)$$

where $R \in [-1, 1]$ is a random number and Z a natural number, $w(x, y)$ being the unnoisy modes.

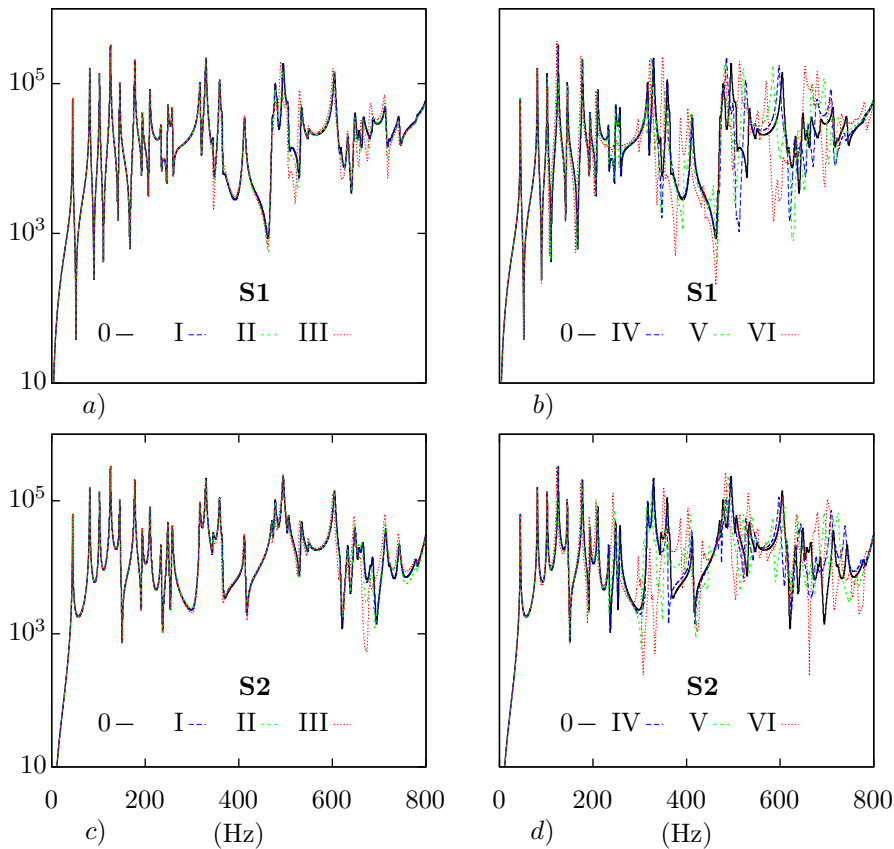


Figure 5.7: FRF at locations S1 (a, b) and S2 (c, d) and cases 0, I, II, III (a, c) and 0, IV, V, VI (b, d)

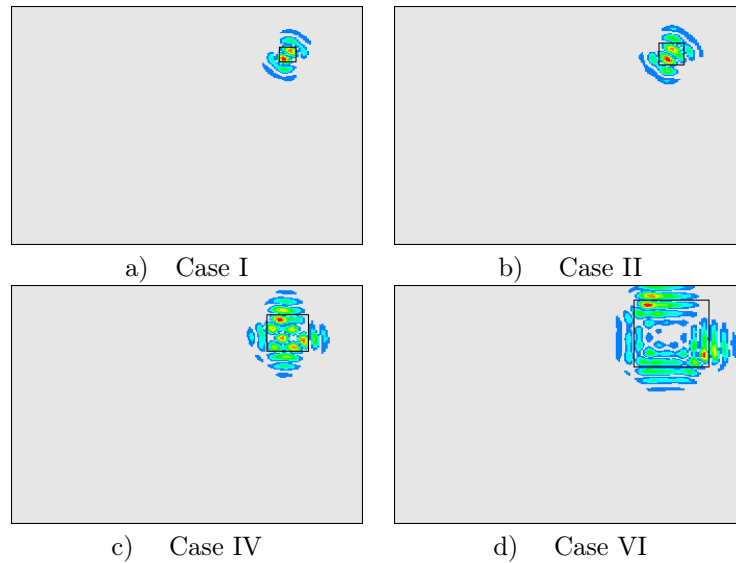


Figure 5.8: Damage index $D(x, y)$ for damage cases I (a), II (b), IV (c) and VI (d) using mode 1. Horizontal line: coordinate x ; vertical line: coordinate y

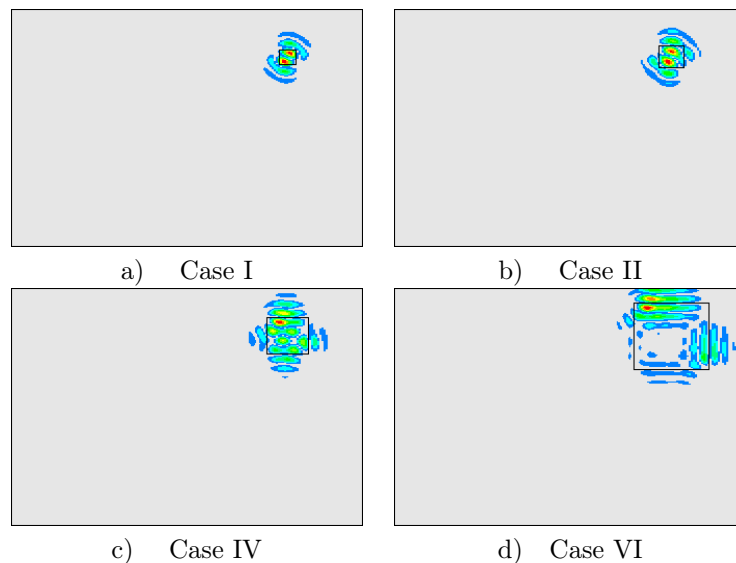


Figure 5.9: Damage index $D(x, y)$ for damage cases I (a), II (b), IV (c) and VI (d) using mode 3. Horizontal line: coordinate x ; vertical line: coordinate y

Different tests were made in order to find the maximum natural number Z allowing us to detect and locate damage. Figures 5.12 and 5.13 show the damage index $D(x, y)$, calculated for the plates with damage cases I, II, IV and VI using, respectively, noisy modes 1 and 3, with the noise added according to the Equation (5.18) with $Z = -4$, this being the maximum value of Z that permits damage to be detected. It can be seen that, despite the fact that some noise appears in the damage index near the edges, the delaminations were very well located. This noise is intrinsic to the technique and it is associated with the fact that only four modes are used in the Ritz series (see Ref. [69]). Greater values of Z give unsuccessful results for damage location. Thus, to ensure the right damage location,

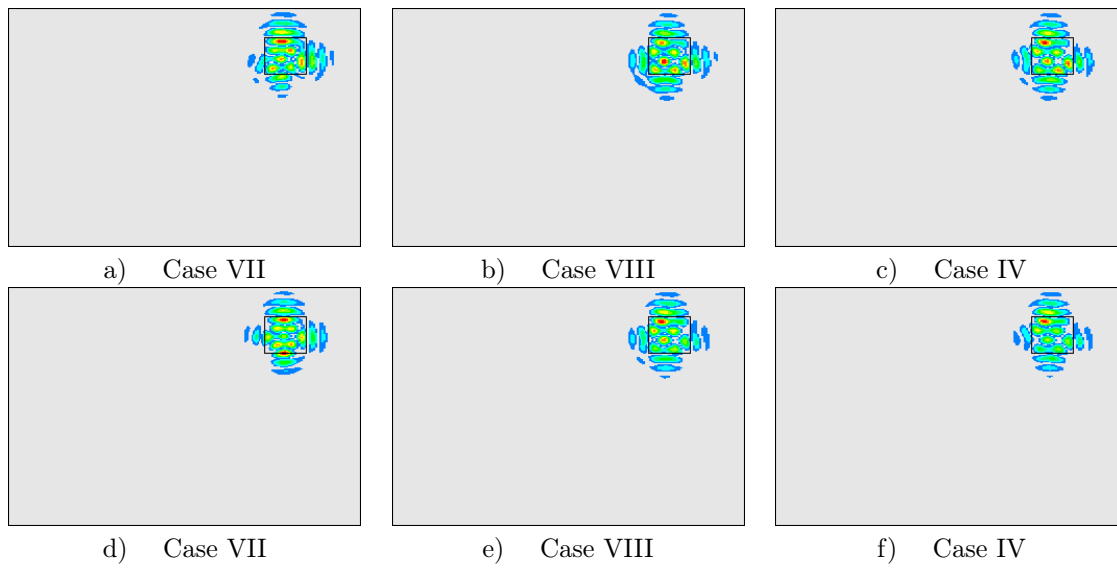


Figure 5.10: Damage index $D(x, y)$ for damage cases VII (a, d), VIII (b, e) and IV (c, f) using mode 1 (a, b, c) and mode 3 (d, e, f). Horizontal line: coordinate x ; vertical line: coordinate y

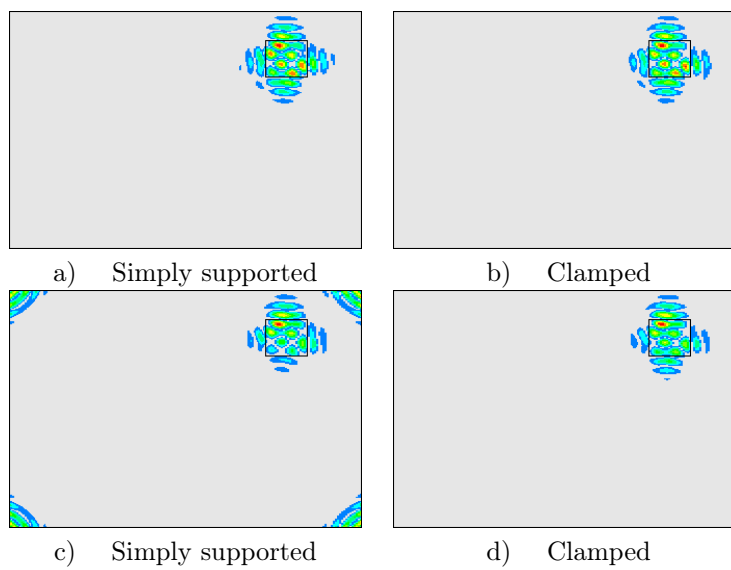


Figure 5.11: Damage index $D(x, y)$ for damage case IV when the plate is fully simply supported (a, c) and fully clamped (b, d) using mode 1 (a, b) and mode 3 (c, d). Horizontal line: coordinate x ; vertical line: coordinate y

sensors and instrumentation system with a sensitivity higher than 10^{-4} with respect to the maximum value of the mode should be used.

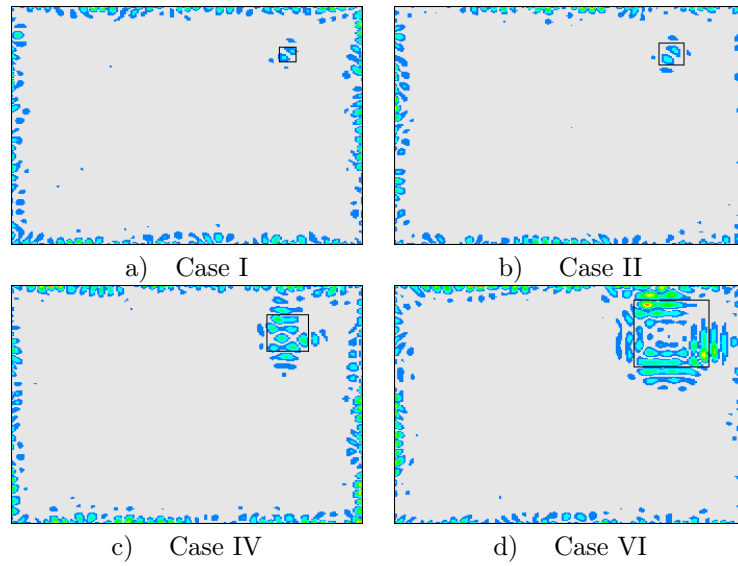


Figure 5.12: Damage index $D(x, y)$ for damage cases I (a), II (b), IV (c) and VI (d) using noisy mode 1. Horizontal line: coordinate x ; vertical line: coordinate y

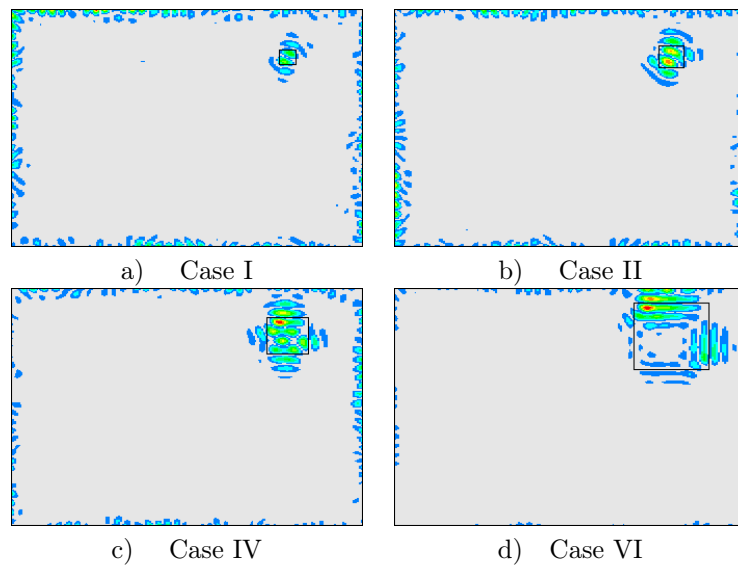


Figure 5.13: Damage index $D(x, y)$ for damage cases I (a), II (b), IV (c) and VI (d) using noisy mode 3. Horizontal line: coordinate x ; vertical line: coordinate y

5.6 Conclusions

This paper presents a new method of delamination detection in CFRP plates. Based on the Ritz method and the Wavelet Transform, the method allows for the detection of delamination using only the damaged response. To test the method, numerical simulations were performed. For this purpose, we developed a novel 4-node quadrilateral ESL finite element, which models a delaminated composite based on CLT. Given a simple kinematic assumption, its formulation is described for a composite with multiple delaminations.

Eight different cases of damage were tested on a $[0/90]_{3S}$ CFRP plate. In order to demonstrate the advantages of this method, results were compared with those of classical methods including mode shapes and FRF analysis. The proposed method makes it possible to detect delamination at Level 2 (location) of Rytter's damage identification hierarchy using the lower modes, thereby making it advantageous with respect to the classical methods.

The influence of the delamination thickness position and the boundary conditions was studied, showing that the thickness position barely influences the damage detection, and that when the boundary conditions are less restrictive (simply supported vs clamped) the proposed technique can present some limitations (occurrence of noise in the corners). Also, a study adding noise to the simulated damaged modes was carried out, finding that to ensure the damage detection with experimental data, sensors and an instrumentation system with sensitivity higher than 10^{-4} with respect to the maximum value of the mode should be used.

Chapter 6

Conclusions and further works

This Doctoral Thesis pursues several objectives to study composite applications in the field of the aerospace industry.

Two main blocks comprise this research:

- Developing a composite shell with a novel IGA formulation.
- Studying the effect of delamination on composite plates.

Isogeometric Analysis is a very promising methodology, unifying geometric definition and Finite Element Analysis in one tool. This methodology allows us to define complex geometries using NURBS.

Firstly, an isoparametric composite shell has been implemented for a higher-order ESL theory, through the use of higher-order NURBS, resulting in a good formulation for static and modal analysis.

Although higher-order NURBS present better accuracy than standard finite element ones, the shell is further improved, in order to avoid locking.

Particularly shear-locking is avoided through the use of a hierarchic discrete difference vector theory, while curvature-locking is avoided by the use of projection techniques.

The following conclusions and observations can thus be extracted from the first part (Chapters 1 and 2):

- IGA admits complex geometries, without requiring mesh refinements.
- The strain and stress are continuous.
- IGA presents the same numerical issues as the standard finite element method does.
- Isoparametric higher-order NURBS work well for most of the standard problems.
- The proposed locking-free shell presents better results for very thin shells and for high-curvature ones.
- The proposed locking-free shell presents better results for higher frequencies.

Several benchmark and numerical problems are compared with the IGA ones in order to test the implemented shell and to proof its efficiency.

In further works, other locking strategies will be performed. The theory will be generalized for a non-linear regime.

For the time being, and within the field of Structural Health Monitoring (SHM), two objectives are achieved.

Firstly, a delaminated composite element was implemented with the standard finite element theory, to study how dynamic properties were affected by the presence of delamination from a comprehensive point of view. Mode shape changes, frequency shifts and FRF changes are analyzed in order to quantify the influence of delamination. In general, changes tend to be greater as the delamination size grows, requiring the use of higher order frequencies to detect small delaminations.

Secondly, the experimental validation of this idea was performed with three composite orthotropic plates $[0\ 90]_{3S}$, two of them having internal delamination. Similar behaviour was observed in the experiments and the simulations, the frequency shifts obtained from the FRF being the variable used to compare both methods.

The following conclusions can therefore be extracted from the second part (Chapters 3 and 4):

- Mode shape changes are more powerful to identify delamination than frequency shifts.
- The PULSE-System does not introduce relevant noise for different experiments.
- A variance for frequencies in the experiment was set for the studied bandwidth, since the experiment was performed on three different plates.
- Amplitude changes in the FRF were only taken into account if the changes were noticeable.
- The plates were free of in-plane stresses.
- FRF analysis was able to identify delamination. In order to clearly detect small delaminations, higher frequencies were required.
- The behaviour resulting from theory and experiments was similar.
- Model based methods should be used from a comprehensive point of view.

Finally, an additional contribution from a paper involving the collaboration of this author is provided, giving the numerical results for some delaminated plates, in order to validate a new damage detection technique developed by a member of the group.

In future work, the study of Lamb waves on delaminated plates will be performed from a numerical point of view.

References

- [1] R.M. Jones, *Mechanics of composite materials*, Taylor and Francis, Philadelphia, USA, 2th edition, 1999.
- [2] A.K. Noor and W.S. Burton and J.M. Peters, “Assessment of computational models for multi-layered composite cylinders”, *International Journal of Solids and Structures*, 27(10): 1269–1286, 1991, ISSN 0020-7683.
- [3] J.N. Reddy, *Mechanics of laminated composite plate and shells. Theory and analysis*, CRC Press, Florida, USA, 2th edition, 1997.
- [4] T.J.R. Hughes and J.A. Cottrell and Y. Bazilevs, “Isogeometric analysis: CAD, finite elements, NURBS, exact geometry and mesh refinement”, *Computer Methods in Applied Mechanics and Engineering*, 194(39-41): 4135–4195, 2005, ISSN 0045-7825.
- [5] T.J.R. Hughes and J.A. Cottrell and Y. Bazilevs, *Isogeometric analysis: CAD, finite elements, NURBS, exact geometry and mesh refinement*, Volume 194, Elsevier Science SA, PO BOX 564, 1001 Lausanne, Switzerland, 2005, ISSN 0045-7825, pages 4135–4195.
- [6] E. Cohen and T. Martin and R.M. Kirby and T. Lyche and R.F. Riesenfeld, “Analysis-aware modeling: Understanding quality considerations in modeling for isogeometric analysis”, *Computer Methods in Applied Mechanics and Engineering*, 199(5-8, SI): 334–356, 2010, ISSN 0045-7825.
- [7] P. Kagan and A. Fischer, “Integrated mechanically based CAE system using B-Spline finite elements”, *Computer-Aided Design*, 32(8-9): 539–552, JUL-AUG 2000, ISSN 0010-4485, 5th ACM Symposium on Solid Modeling and Applications, Ann Arbor, Michigan, Jun 09-11, 1999.
- [8] R. Schmidt and J. Kiendl and K.U. Bletzinger and R. Wuchner, “Realization of an integrated structural design process: analysis- suitable geometric modelling and isogeometric analysis”, *Computing and Visualization in Science*, 13(7): 315–330, 2010.
- [9] L.A. Piegl and W. Tiller, *The NURBS Book (Monographs in Visual Communication)*, Springer, New York, 2th edition, 1997.
- [10] D.F. Rogers, *An Introduction to NURBS with Historical Perspective*, Morgan Kaufmann Publishers, San Francisco, 2001.
- [11] G. Farin, *Curves and surfaces for CAGD*, Morgan Kaufmann Publishers, San Francisco, 2002.
- [12] E. Cohen and R.F. Riesenfeld and G. Elber, *Geometric Modeling with Splines: An Introduction*, Peters A.K. and Natick M.A., San Francisco, 2001.
- [13] J.N. Reddy, “A simple higher-order theory for laminated composite plates”, *Journal of Applied Mechanics-Transactions of the ASME*, 51(4): 745–752, 1984, ISSN 0021-8936.
- [14] J.N. Reddy, “A refined nonlinear-theory of plates with transverse-shear deformation”, *International Journal of Solids and Structures*, 20(9-10): 881–896, 1984, ISSN 0020-7683.

-
- [15] J.N. Reddy, “Exact-solutions of moderately thick laminated shells”, *Journal of Engineering Mechanics-ASCE*, 110(5): 794–809, 1984, ISSN 0733-9399.
- [16] J. Reddy, C. Liu, “A higher-order shear deformation-theory of laminated elastic shells”, *International Journal of Engineering Science*, 23(3): 319–330, 1985, ISSN 0020-7225.
- [17] J. Kiendl, K.U. Bletzinger, J. Linhard, R. Wuechner, “Isogeometric shell analysis with Kirchhoff-Love elements”, *Computer Methods in Applied Mechanics and Engineering*, 198(49-52): 3902–3914, 2009, ISSN 0045-7825.
- [18] S. Shojaee, N. Valizadeh, E. Izadpanah, T. Bui, T.V. Vu, “Free vibration and buckling analysis of laminated composite plates using the NURBS-based isogeometric finite element method”, *Composite Structures*, 94(5): 1677–1693, APR 2012, ISSN 0263-8223.
- [19] N. Pagano, “Exact solutions for rectangular bidirectional composites and sandwich plates”, *Journal of Composite Materials*, 4(Jan): 20–34, 1970, ISSN 0021-9983.
- [20] J. Reddy, “A simple higher-order theory for laminated composite plates”, *Journal of Applied Mechanics-Transactions of the ASME*, 51(4): 745–752, 1984, ISSN 0021-8936.
- [21] G. Akhras, M. Cheung, W. Li, “Static and vibration analysis of anisotropic composite laminates by finite strip method”, *International Journal of Solids and Structures*, 30(22): 3129–3137, 1993, ISSN 0020-7683.
- [22] Computers and Structures, Inc., *SAP2000. Educational version*, University of California, Berkeley, <http://www.sap2000.org>.
- [23] K.P. Rao, “A rectangular laminated anisotropic shallow thin shell finite element”, *Computer Methods in Applied Mechanics and Engineering*, 15: 13–33, 1978.
- [24] C.F. Casanova, A. Gallego, “NURBS-based analysis of higher-order composite shells”, *Composite Structures*, 104(0): 125 – 133, 2013, ISSN 0263-8223.
- [25] Q. Long, P.B. Bornemann, F. Cirak, “Shear-flexible subdivision shells”, *International Journal for Numerical Methods in Engineering*, 90(13): 1549–1577, JUN 29 2012, ISSN 0029-5981.
- [26] R. Echter, B. Oesterle, M. Bischoff, “A hierarchic family of isogeometric shell finite elements”, *Computer Methods in Applied Mechanics and Engineering*, 254: 170–180, FEB 2013, ISSN 0045-7825.
- [27] T.J.R. Hughes, *The Finite Element Method: Linear Static and Dynamic Finite Element Analysis*, Prentice-Hall, New Jersey, 1987.
- [28] O.C. Zienkiewicz and R. L. Taylor and J.Z. Zhu, *The Finite Element Method: Its Basis and Fundamentals*, Volume 1, Elsevier, United Kingdom, 6th edition, 2005.
- [29] S. Timoshenko, S. Woinowsky-Krieger, *Theory of Plates and Shells*, McGraw-Hill Book Company, New York, US, 1959.
- [30] C.M. Wang, J.N. Reddy, K. Lee, *Shear Deformable Beams and Plates*, Elsevier, Oxford, UK, 2000, ISBN 0 08 043784 2.
- [31] L.S.D. Morley, *Bending of clamped rectilinear plates*, Volume 17, Quarterly journal of mechanics and applied mathematics, 1964, ISBN 0033-5614, pages 293–317.
- [32] A. Rytter, *Vibration based inspection of civil engineering structures*, PhD thesis, Department of Building Technology Structural Engineering. University of Aalborg, Denmark., 1993.
- [33] Y. Zou, L. Tong, G.P. Steven, “Vibration-based model-dependent damage (delamination) identification and health monitoring for composite structures - A review”, *Journal of Sound and Vibration*, 230(2): 357–378, 2000, ISSN 0022-460X.
-

- [34] S.W. Doebling, C.R. Farrar, M.B. Prime and D.W. Shevitz, “Damage identification and health monitoring of structural and mechanical systems from changes in their vibration characteristics: A literature review”, Technical Report LA-13070-MS, Los Alamos National Laboratory, Los Alamos, NM. 87545, 1996.
- [35] C.R. Farrar, S.W. Doebling, D.A. Nix, “Vibration-based structural damage identification”, *Philosophical Transactions of the Royal Society of London Series a-Mathematical Physical and Engineering Sciences*, 359(1778): 131–149, JAN 15 2001, ISSN 1364-503X.
- [36] D. Balageas, C. Fritzen, A. Güemes, *Structural Health Monitoring*, ISTE, United Kingdom, 2007.
- [37] A. Alvandi, C. Cremona, “Assessment of vibration-based damage identification techniques”, *Journal of Sound and Vibration*, 292(1-2): 179–202, 2006, ISSN 0022-460X.
- [38] C.P. Fritzen, K. Bohle, “Identification of Damage in Large Scale Structures by Means of Measured FRFs-Procedure and Application to the I40-Highway Bridge”, in *Damage Assessment of Structures, Proceedings of the International Conference on Damage Assessment of Structures (DAMAS 99)*, Dublin, Ireland, pages 310–319, 1999, ISBN 0-87849-839-7, ISSN 1013-9826.
- [39] K. Bohle, C.P. Fritzen, “Results obtained by minimising natural frequency and mac-value errors of a plate model”, *Mechanical Systems and Signal Processing*, 17(1): 55–64, 2003, ISSN 0888-3270.
- [40] L. Yu, T. Yin, “Damage Identification in Frame Structures Based on FE Model Updating”, *Journal of Vibration and Acoustics-Transactions of the ASME*, 132(5), 2010, ISSN 1048-9002.
- [41] W. Liu, W.C. Gao, Y. Sun, “Application of Modal Identification Methods to Spatial Structure Using Field Measurement Data”, *Journal of Vibration and Acoustics-Transactions of the ASME*, 131(3), 2009, ISSN 1048-9002.
- [42] S.T. Jenq, W.D. Lee, “Identification of hole defect for GFRP woven laminates using neural network scheme”, in Chang, F. K. (Editor), *Structural Health Monitoring: Current status and perspectives*, pages 741–751, 1997, ISBN 1-56676-605-2, International Workshop on Structural Health Monitoring, Stanford Univ., Stanford, CA, Sept. 18-20, 1997.
- [43] M.Q. Feng, E.Y. Bahng, “Damage assessment of bridges with jacketed RC columns using vibration test”, in Liu, S. C. (Editor), *Smart Structures and Materials 1999: Smart systems for bridges, Structures and Highways*, Volume 3671 of *Proceedings of the Society of Photo-Optical Instrumentation Engineers (SPIE)*, pages 316–327, 1999, ISBN 0-8194-3145-1, Conference on Smart Systems for Bridges, Structures, and Highways at Smart Structures and Materials 1999, Newport Beach, CA, Mar. 01-02, 1999.
- [44] A. Zak, M. Krawczuk, W. Ostachowicz, “Vibration of a laminated composite plate with closing delamination”, *Journal of Intelligent Material Systems and Structures*, 12(8): 545–551, AUG 2001, ISSN 1045-389X, 3rd International Conference on Damage Assessment of Structures (DAMAS 99), Dublin, Ireland, June 28-30, 1999.
- [45] A. Zak, M. Krawczuk, W. Ostachowicz, “Numerical and experimental investigation of free vibration of multilayer delaminated composite beams and plates”, *Computational Mechanics*, 26(3): 309–315, 2000, ISSN 0178-7675.
- [46] S. Hanagud, H. Luo, “Damage detection and health monitoring based on structural dynamics”, in Chang, F. K. (Editor), *Structural Health Monitoring: Current status and perspectives*, pages 715–726, 1997, ISBN 1-56676-605-2, International Workshop on Structural Health Monitoring, Stanford Univ., Stanford, CA, Sept. 18-20, 1997.
- [47] H.Y. Kim, W. Hwang, “Effect of debonding on natural frequencies and frequency response functions of honeycomb sandwich beams”, *Composite Structures*, 55(1): 51–62, 2002, ISSN 0263-8223.

-
- [48] M. Krawczuk, W. Ostachowicz, “Identification of delamination in composite beams by genetic algorithm”, *Science and Engineering of Composite Materials*, 10(2): 147–155, 2002, ISSN 0334-181X.
- [49] H.Y. Ling, K.T. Lau, L. Cheng, W. Jin, “Fibre optic sensors for delamination identification in composite beams using a genetic algorithm”, *Smart Materials & Structures*, 14(1): 287–295, 2005, ISSN 0964-1726.
- [50] Z. Wei, L.H. Yam, L. Cheng, “Delamination assessment of multilayer composite plates using model-based neural networks”, *Journal of Vibration and Control*, 11(5): 607–625, 2005, ISSN 1077-5463.
- [51] G.W. Sanders, F. Akhavan, S.E. Watkins, K. Chandrashekhara, “Fiber optic vibration sensing and neural networks methods for prediction of composite beam delamination”, in Regelbrugge, M.E. (Editor), *Smart Structures and Integrated Systems - Smart Structures and Materials 1997*, Volume 3041 of *Proceedings of the Society of Photo-Optical Instrumentation Engineers (SPIE)*, pages 858–867, 1997, ISBN 0-8194-2454-4, Conference on Smart Structures and Integrated Systems - Smart Structures and Materials 1997, San Diego, CA, Mar. 03-06, 1997.
- [52] S.E. Watkins, G.W. Sanders, F. Akhavan, K. Chandrashekhara, “Modal analysis using fiber optic sensors and neural networks for prediction of composite beam delamination”, *Smart Materials & Structures*, 11(4): 489–495, 2002, ISSN 0964-1726.
- [53] C. Harrison, R. Butler, “Locating delaminations in composite beams using gradient techniques and a genetic algorithm”, *AIAA JOURNAL*, 39(7): 1383–1389, 2001, ISSN 0001-1452.
- [54] E. Figueiredo, G. Park, K.M. Farinholt, C.R. Farrar, J.R. Lee, “Use of Time-Series Predictive Models for Piezoelectric Active-Sensing in Structural Health Monitoring Applications”, *Journal of Vibration and Acoustics-Transactions of the ASME*, 134(4), AUG 2012, ISSN 1048-9002.
- [55] B.R. Zwink, “Nondestructive Evaluation of Composite Material Damage Using Vibration Reciprocity Measurements”, *Journal of Vibration and Acoustics-Transactions of the ASME*, 134(4), AUG 2012, ISSN 1048-9002.
- [56] D.A. Saravanos, D.A. Hopkins, “Effects of delaminations on the damped dynamic characteristics of composite laminates: Analysis and experiments”, *Journal of Sound and Vibration*, 192(5): 977–993, 1996, ISSN 0022-460X.
- [57] C.N. Delia, D. Shu, “Vibration of delaminated composite laminates: A review”, *Applied Mechanics Reviews*, 60: 1–20, 2007, ISSN 0003-6900.
- [58] M. Damghani, D. Kennedy, C. Featherston, “Critical buckling of delaminated composite plates using exact stiffness analysis”, *Computers & Structures*, 89(13-14): 1286–1294, 2011, ISSN 0045-7949.
- [59] A. Tafreshi, “Efficient modelling of delamination buckling in composite cylindrical shells under axial compression”, *Composite Structures*, 64: 511–520, 2004, ISSN 0263-8223.
- [60] J. Melenk, I. Babuska, “The partition of unity finite element method: Basic theory and applications”, *Computer Methods in Applied Mechanics and Engineering*, 139(1-4): 289–314, DEC 15 1996, ISSN 0045-7825.
- [61] I. Babuska, J. Melenk, “The partition of unity method”, *International Journal for Numerical methods in Engineering*, 40(4): 727–758, FEB 28 1997, ISSN 0029-5981.
- [62] A. Chattopadhyay, D. Dragomir-Daescu, H. Gu, “Dynamic response of smart composites with delaminations”, in Chang, F. K. (Editor), *Structural Health Monitoring: Current status and perspectives*, pages 729–740, 1997, ISBN 1-56676-605-2, International Workshop on Structural Health Monitoring, Stanford Univ., Stanford, CA, Sept. 18-20, 1997.
-

- [63] A. Chattopadhyay, H. Kim, A. Ghoshal, “Non-linear vibration analysis of smart composite structures with discrete delamination using a refined layerwise theory”, *Journal of Sound and Vibration*, 273(1-2): 387–407, MAY 21 2004, ISSN 0022-460X.
- [64] C. Swann, A. Chattopadhyay, A. Ghoshal, “Characterization of delamination by using damage indices”, *Journal of Reinforced Plastics and Composites*, 24(7): 699–711, 2005, ISSN 0731-6844.
- [65] E.N. Dvorkin, S.L. Vassolo, “A quadrilateral 2-D finite element based on mixed interpolation of tensorial components”, *Engineering Computing*, 6: 217–224, 1989.
- [66] J.L. Batoz, M. Bentahar, “Evaluation of a new quadrilateral thin plate bending element”, *International Journal for Numerical Methods in Engineering*, 18(11): 1655–1677, 1982.
- [67] R.L. Taylor, *FEAP. A Finite Element Analysis Program: Programmer Manual*, University of California, Berkeley, 2005, <http://www.ce.berkeley.edu/~rlt>.
- [68] C.F. Casanova, A. Gallego, M. Lázaro, “On the Accuracy of a 4-Node Delaminated Composite Plate Element and its Application to Damage Detection”, *Journal of Vibration and Acoustics. Transactions of ASME.*, 1(1): 1–2, 2013.
- [69] P. Moreno-García, *Simulación y ensayos de vibraciones en placas de material compuesto de fibra de carbono y detección de daño mediante la Respuesta en Frecuencia y la Transformada Wavelet*, PhD thesis, University of Granada, Spain, 2012.
- [70] L. Romo Melo, *Diagnóstico de daño en disipadores de energía histeréticos tipo WPD para el control pasivo en estructuras sismorresistentes mediante análisis de vibraciones en el dominio de la frecuencia*, PhD thesis, University of Granada, Spain, 2012.
- [71] L. Tenek, E. Hennekke, M. Gunzburger, “Vibration of delaminated composite plates and some applications to nondestructive testing”, *Composite Structures*, 23(3): 253–262, 1993, ISSN 0263-8223.
- [72] L. Yam, Z. Wei, L. Cheng, W. Wong, “Numerical analysis of multi-layer composite plates with internal delamination”, *Computers & Structures*, 82(7-8): 627–637, MAR 2004, ISSN 0045-7949.
- [73] J. Chen, M. Crisfield, A. Kinloch, E. Busso, F. Matthews, Y. Qiu, “Predicting progressive delamination of composite material specimens via interface elements”, *Mechanics of Composite Materials and Structures*, 6(4): 301–317, OCT-DEC 1999, ISSN 1075-9417.
- [74] J. Oh, M. Cho, J.S. Kim, “Buckling analysis of a composite shell with multiple delaminations based on a higher order zig-zag theory”, *Finite Elements in Analysis and Design*, 44(11): 675–685, 2008, ISSN 0168-874X.
- [75] S.Y. Lee, D.S. Chung, “Finite element delamination model for vibrating composite spherical shell panels with central cutouts”, *Finite Elements in Analysis and Design*, 46(3): 247–256, 2010, ISSN 0168-874X.
- [76] J.V. Araújo dos Santos, N.M.M. Maia, C.M. Mota Soares, C.A. Mota Soares, *Structural Damage Identification: A Survey*, Chapter 1, pages 1–24, Trends in Computational Structures Technology. Saxe-Coburg Publications, Stirlingshire, UK, 2008.
- [77] E. Castro, M.T. García-Hernández, A. Gallego, “Damage detection in rods by means of the wavelet analysis of vibrations: Influence of the mode order”, *Journal of Sound and Vibration*, 296: 1028–1038, Oct. 2006.
- [78] H. Gökdağ, O. Kopmaz, “A new damage detection approach for beam-type structures based on the combination of continuous and discrete wavelet transforms”, *Journal of Sound and Vibration*, 324: 1158–1180, July 2009.

-
- [79] H. Gökdağ, O. Kopmaz, “A new structural damage detection index based on analyzing vibration modes by the wavelet transform”, *Structural Engineering and Mechanics*, 35(2): 257–260, May 2010.
- [80] E. Douka, S. Loutridis, A. Trochidis, “Crack identification in plates using wavelet analysis”, *Journal of Sound and Vibration*, 270: 279–295, 2004.
- [81] C.C. Chang, L.W. Chen, “Damage detection of a rectangular plate by spatial wavelet based approach”, *Applied Acoustics*, 65(8): 819–832, 2004, ISSN 0003-682X.
- [82] S. Loutridis, E. Douka, L.J. Hadjileontiadis, A. Trochidis, “A two-dimensional wavelet transform for detection of cracks in plates”, *Engineering Structures*, 27(9): 1327–1338, Aug. 2005.
- [83] G.B. Chai, “Frequency analysis of rectangular isotropic plates carrying a concentrated mass”, *Computers & Structures*, 56(1): 39–48, July 1995.
- [84] D.R. Avalos, H.A. Larrondo, P.A.A. Laura, “Analysis of Vibrating Rectangular Anisotropic Plates with Free-Edge Holes”, *Journal of Sound and Vibration*, 222(4): 691–695, May 1999.
- [85] P.M. Ciancio, C.A. Rossit, P.A.A. Laura, “Approximate study of the free vibrations of a cantilever anisotropic plate carrying a concentrated mass”, *Journal of Sound and Vibration*, 302(3): 621–628, May 2007.
- [86] C.A. Rossit, P.M. Ciancio, “Free vibrations of anisotropic rectangular plates with holes and attached masses”, *Structural Engineering and Mechanics*, 28(1): 53–67, Jan. 2008, ISSN 1225-4568.
- [87] D. Young, “Vibration of rectangular plates by the Ritz method”, *Journal of Applied Mechanics*, 17(4): 448–453, Dec. 1950, ISSN 0021-8936.
- [88] J.R. Gartner, N. Olgac, “Improved numerical computation of uniform beam characteristic values and characteristic functions”, *Journal of Sound and Vibration*, 84(2): 481–489, Oct. 1982.
- [89] A. Rytter, *Vibration based inspection of civil engineering structures*, PhD thesis, Department of Building Technology Structural Engineering. University of Aalborg, Denmark., 1993.
- [90] R. Fletcher, C.M. Reeves, “Function minimization by conjugate gradients”, *Computer Journal*, 7(2): 149–154, 1964.
- [91] T. Dallard, G.R. Spedding, “2-D wavelet transforms: Generalization of the Hardy space and application to experimental studies”, *European Journal of Mechanics - B/Fluids*, 12: 107–134, 1993.
- [92] J.P. Antoine, P. Carrette, R. Murenzi, B. Piette, “Image analysis with two-dimensional continuous wavelet transform”, *Signal Processing*, 31(3): 241–272, Apr. 1993.
- [93] L. Jacques, A. Coron, P. Vandergheynst, A. Rivoldini, “The YAWTb toolbox: Yet Another Wavelet Toolbox”, Web page: <http://rhea.tele.ucl.ac.be/yawtb>.